This paper is published as part of a *PCCP* themed issue on
[chemical dynamics of large amplitude motion](#)

Guest editors: David J. Nesbitt and Martin A. Suhm

High resolution electronic spectroscopy of 4-methylanisole in the gas phase. Barrier height determinations for the methyl group torsional motion
Philip J. Morgan, Leonardo Alvarez-Valtierra and David W. Pratt, *Phys. Chem. Chem. Phys.*, 2010
DOI: 10.1039/c000757a

Determination of precise relative energies of conformers of *n*-propanol by rotational spectroscopy
Zbigniew Kisiel, Orest Dorosh, Atsuko Maeda, Ivan R. Medvedev, Frank C. De Lucia, Eric Herbst, Brian J. Drouin, John C. Pearson and Steven T. Shipman, *Phys. Chem. Chem. Phys.*, 2010
DOI: 10.1039/c002156c

Microwave spectroscopy of the Ne–OH($^2\Pi_i$) complex and three-dimensional intermolecular potentials
Yoshihiro Sumiyoshi, Ippei Funahara, Kazuya Sato, Yasuhiro Ohshima and Yasuki Endo, *Phys. Chem. Chem. Phys.*, 2010
DOI: 10.1039/c002193h

Rotational spectra of *o*-, *m*-, and *p*-cyanophenol and internal rotation of *p*-cyanophenol
Andrew R. Conrad, Nathan Z. Barefoot and Michael J. Tubergen, *Phys. Chem. Chem. Phys.*, 2010
DOI: 10.1039/c001705a

Hydrogen exchange in formic acid dimer: tunnelling above the barrier
David Luckhaus, Phys. Chem. Chem. Phys., 2010
DOI: 10.1039/c001253j

Tunneling dynamics and spectroscopic parameters of monodeuterated hydronium, H_2DO^+, from a combined analysis of infrared and sub-millimeter spectra
Holger S. P. Müller, Feng Dong, David J. Nesbitt, Takashi Furuya and Shuji Saito, *Phys. Chem. Chem. Phys.*, 2010
DOI: 10.1039/c002067b

On the efficiency of treating singularities in triatomic variational vibrational computations. The vibrational states of H+3 up to dissociation
Tamás Szidarovszky, Attila G. Császár and Gábor Czakó, *Phys. Chem. Chem. Phys.*, 2010
DOI: 10.1039/c001124j

Theoretical rotation–torsion spectra of HSOH
Andrey Yachmenev, Sergei N. Yurchenko, Per Jensen, Oliver Baum, Thomas F. Giesen and Walter Thiel, *Phys. Chem. Chem. Phys.*, 2010
DOI: 10.1039/c002803g

Chirality of and gear motion in isopropyl methyl sulfide: A Fourier transform microwave study
Eizi Hirota, Keisuke Sakieda and Yoshiyuki Kawashima, *Phys. Chem. Chem. Phys.*, 2010
DOI: 10.1039/c002314k

Torsional energy levels of nitric acid in reduced and full dimensionality with ELVIBROT and TNUM
David Lauvergnat and André Nauts, Phys. Chem. Chem. Phys., 2010
DOI: 10.1039/c001944e

Analysis of the FASSST rotational spectrum of NCNCS in view of quantum monodromy†

Brenda P. Winnewisser,*[a] Manfred Winnewisser,[a] Ivan R. Medvedev,[a]
Frank C. De Lucia,[a] Stephen C. Ross[b] and Jacek Koput[c]

Quantum monodromy has a strong impact on the ro-vibrational energy levels of chain molecules whose bending potential energy function has the form of the bottom of a champagne bottle (*i.e.* with a hump or punt) around the linear configuration. NCNCS, cyanogen iso-thiocyanate, is a particularly good example of such a molecule and clearly exhibits a distinctive monodromy-induced dislocation of the energy level pattern at the bending-rotation energy at the top of the potential energy hump. Indeed, NCNCS [B. P. Winnewisser *et al.*, *Phys. Rev. Lett.* 2005, **95**, 243002] and the water molecule [N. F. Zobov *et al.*, *Chem. Phys. Lett.* 2005, **414**, 193–197] were the first two molecules for which experimental confirmation of quantum monodromy was obtained. We used the fast scan sub-millimetre spectroscopic technique (FASSST) to extend the measurements and spectral analysis to pure rotational transitions (end-over-end) in bending vibrational states lying well above the monodromy point. The analysis of 9204 lines assigned to 7 vibrational states, presented here, shows that the topological properties of the bending potential function are mapped onto every aspect of the ro-vibrational energy levels involving excitation of the quasi-linear bending vibration. In order to model the large amplitude dynamics of such a molecular system, and also to achieve some insight beyond satisfactory parameters for reproducing the spectrum, we used the generalized semi-rigid bender (GSRB) Hamiltonian, which is described in some detail. This Hamiltonian provides a good description of the energy levels over the seven bending states observed, coming close to experimental accuracy. Due to high J values of the measured rotational transitions ($J \leq 116$), the least squares fitting procedure was applied not directly to the measured frequencies, but to effective constants derived from fitting the transition frequencies to a set of polynomials in $J(J + 1)$ yielding effective B_{eff} and D_{eff} constants. The GSRB wave functions are used to show that the expectation values of any quantity which varies with the large amplitude bending coordinate will also have monodromy-induced dislocations. This includes the electric dipole moment components. High level *ab initio* calculations not only provided the molecular equilibrium structure of NCNCS, but also the electric dipole moment components μ_a and μ_b as functions of the large-amplitude bending coordinate. Calculated expectation values of these quantities for individual ro-vibrational levels show the now recognizable monodromy pattern. Finally, a generalization of the quasi-linear parameter γ_0 is suggested.

1. Introduction

In two previous papers,[1,2] we have used pure rotational (end-over-end) transitions to show that NCNCS exhibits a pattern of rotation-bending energy levels characteristic of non-trivial monodromy: an abrupt transition, softened somewhat by quantum mechanics, from the pattern typical of a bent molecule to that expected for a linear molecule as the

vibrational excitation passes above the top of the barrier to linearity. At first glance this appears surprising. However, the determination of the potential energy function and vibrational spacings from purely rotational transitions has already been accomplished for a variety of molecules using the semi-rigid bender approach. In the present paper, we present a comprehensive analysis of the data behind the conclusions discussed in the two previous papers, with an extension of the assigned and fitted data to one higher excited bending state. The highly characteristic effects of monodromy on the end-over-end rotational energy levels are shown in detail.

The present paper is dedicated to Herb Pickett and Ed Cohen, who respectively wrote and cultivated the JPL program package[3] widely used for the analysis of rotational spectra. The analysis of the NCNCS spectrum is appropriate for this purpose, because the main units of SPFIT and SPCAT

[a] *Department of Physics, The Ohio State University, Columbus Ohio, 43210-1106, USA. E-mail: winnebp@mps.ohio-state.edu*
[b] *Department of Physics and Centre for Laser, Atomic, and Molecular Sciences, University of New Brunswick, P.O. Box 4400, Fredericton NB E3B 5A3, Canada*
[c] *Department of Chemistry, Adam Mickiewicz University, 60-780 Poznan, Poland*
† Electronic supplementary information (ESI) available: Supplementary Tables 1–3. See DOI: 10.1039/b922023b
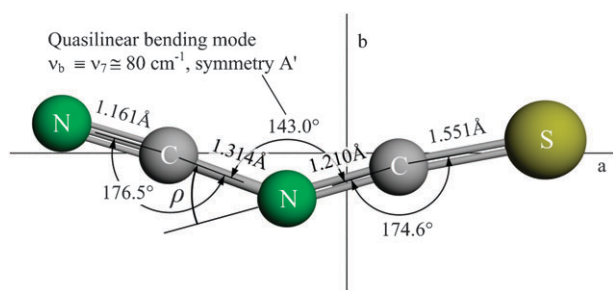
Fig. 1 *Ab initio* predicted equilibrium structure of NCNCS in the principal axis system of the inertia tensor. The large-amplitude coordinate ρ is the complement of the CNC bond angle.

became indispensable integrated units in the program package CAAARS (Computer Aided Assignment of Asymmetric Rotor Spectra)[4] written in this laboratory. The first sight of the dense spectrum of NCNCS was one of the motivations to develop CAAARS. The basic organization of SPFIT and SPCAT—separate files for lines, parameters and log of run in fitting (SPFIT), separate list of predictions and log of run from catalog calculation (SPCAT)—made them ideal for repeated, iterative launching from the assignment procedure. Actually, NCNCS was a challenge for these programs, because neither the linear nor the asymmetric molecule Hamiltonians

can be used to properly label or even to calculate the energy levels with anything close to experimental accuracy.

In 1980 King and Kroto[5] reported the observation of a new microwave spectrum during flow thermolysis experiments involving sulfur dicyanide, $S(CN)_2$. What they had found was the isomerization product cyanogen isothiocyanate, NCNCS. This molecule is a wing-shaped species with two essentially straight entities attached to the central nitrogen atom as shown in Fig. 1.

In the preface to the Dover Edition of his book, Harry Kroto[6] wrote: *The gradual change from asymmetric rotor to pseudo-linear molecule, which takes place as the bending vibrational quantum number increases, is beautifully depicted in the vibrational satellite structure of the J = 12 ← 11 rotational transition.* This statement was even more true than he realized at that time. In Fig. 2 we present the original Figure with some modifications. The assignment comb for $v_b = 0$, the ground vibrational state of NCNCS, exhibits a pattern characteristic of a slightly asymmetric prolate rotor. With increasing excitation of the large amplitude bending motion at the central nitrogen this pattern "metamorphoses to that of a pseudo-linear molecule", using a phrase of Harry Kroto. This observation referred primarily to the relative positions of the $K_a = 0$ line and the $K_a = 1$ doublet lines.
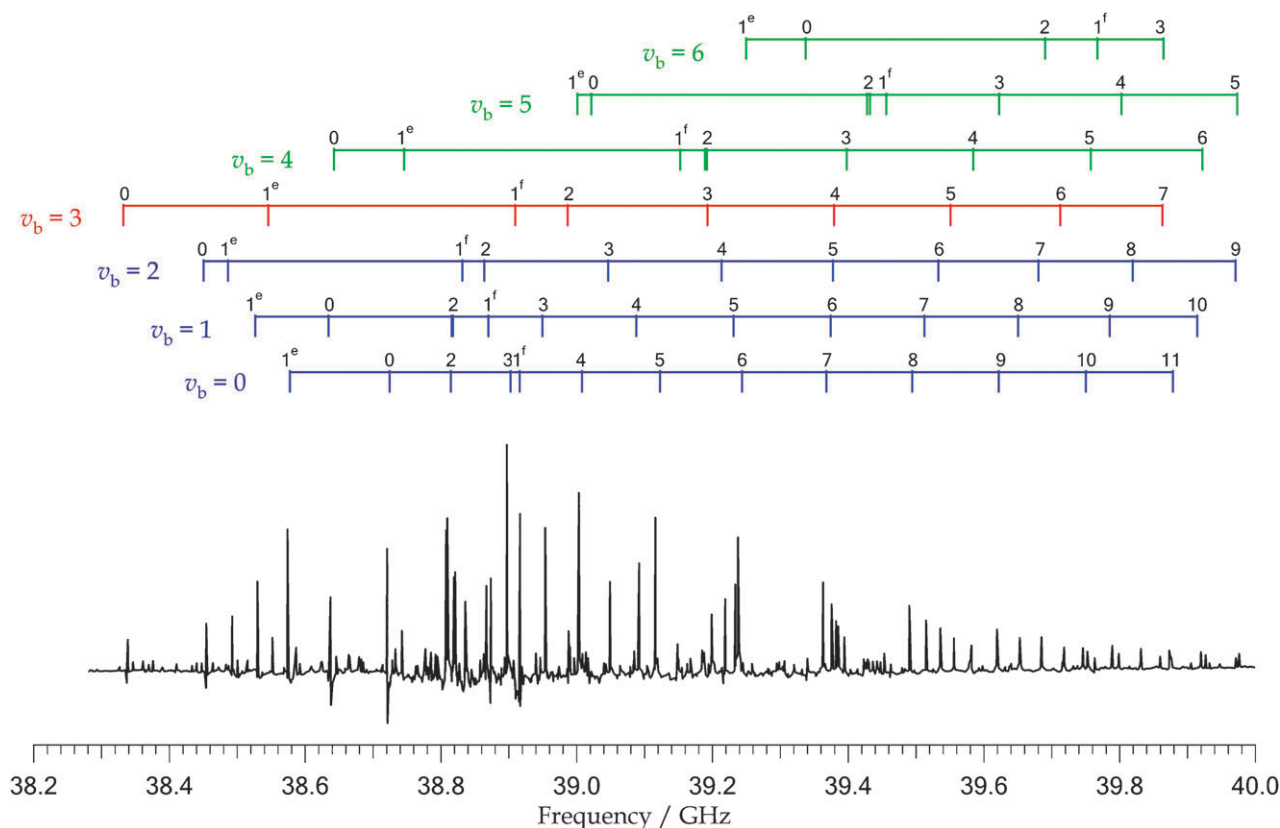
Fig. 2 The $J = 12 \leftarrow 11$ rotational transition of NCNCS, based on the Figure on page 22 in ref. 6 and shown with the assignments extended. The K_a numbers are indicated for every v_b. The microwave survey spectrum was run with 2000 V cm^{-1} electric field strength, accentuating lines with high K_a; lines with $K_a = 1$ and 0 appear weak.[7] The original four sets of transitions for $v_b = 0$ to $v_b = 3$ were assigned by King *et al.*[7] The extension to $v_b = 4$, 5 and 6 is part of this work. The color scheme throughout this paper is: properties arising from bending vibrational states for which $K_a = 0$ lies below the barrier (monodromy point) are drawn in blue. The state closest to the monodromy point is indicated in red, while all states for which the energy of the $K_a = 0$ level is well above the monodromy point are shown in green.

$$V(r) = r^4 - r^2$$
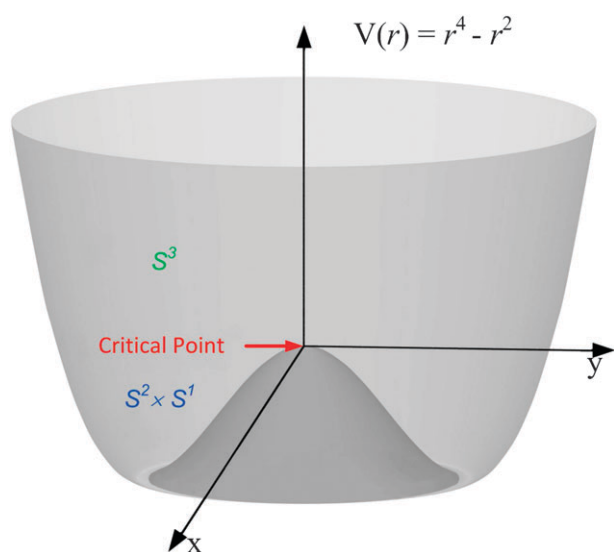
Fig. 3 The volume defined by the champagne bottle potential function for the quasi-linear two-dimensional bending mode of NCNCS bifurcates into two spaces, with the indicated topologies in blue and green, at the critical point or monodromy point marked in red, which is the top of the potential hump and the origin of the coordinate system.

The bending potential function derived from the first analysis of the microwave data by King *et al.*[7] yielded the height of the barrier to linearity as 270 cm^{-1}, which implies that we should be able to probe ro-vibrational energy states both below and above the hump. This type of potential function is shown in Fig. 3.

King, Kroto and Landsberg[7] did not assign lines for any vibrational state above the barrier. They probably could not, because they were not aware of the dramatic changes still to be observed in the spectrum. Most prominent is the abrupt reversal of the sequence of frequency positions of the $K_a = 0$ lines for $v_b = 4$, 5 and 6 as shown now in our Fig. 2. A reversal is indeed predicted for NCNCS in ref. 8, but the patterns in the spectrum were not modeled for higher excitation at that time, and the relevant mathematics had not even been formulated.

Like all of their contemporary spectroscopists they were not aware that a mathematical concept new to spectroscopy was hidden in the vibrational satellite structure of NCNCS. The concept of monodromy (Greek for "once around") in a champagne bottle potential was only introduced in 1991 by the mathematician Larry Bates.[9]

Since the two-dimensional NC–N=CS bending potential function is circularly symmetric, we have two conserved physical quantities, energy and angular momentum.[1] In quantum mechanics these quantities correspond to the commuting operators of energy and angular momentum, with their respective observables. At the energy of the top of the hump, called the monodromy point, the topology of the potential energy surface bifurcates according to Bates[9] into two distinct spaces (see Fig. 3) with surface topology $S^2 \times S^1$ below and S^3 above the monodromy point.[2] This sudden change in topology causes an associated torus bundle in phase space to exhibit nontrivial monodromy, which means there

does not exist a complete set of globally well-defined action variables.[2] This set would consist of total energy, vibrational energy, and rotational (about the Figure axis) energy. In quantum mechanics, classical monodromy translates into a dislocation in the pattern of discrete energy levels around the monodromy point[2] in the energy-momentum map. That this mathematics was relevant to molecular spectroscopy was grasped by Mark Child, who developed its application to triatomic molecules, and especially to the case of H$_2$O.[10–14] The change in topology involves the reclassification of one degree of freedom from rotational (below the barrier) to vibrational (above the barrier),[15–17] a transition which is considerably more abrupt than was thought earlier.

For two chain-type molecules, cyanogen iso-thiocyanate, NCNCS,[1] and water, HOH,[18] the experimental data so far available cover regions both below and above the monodromy point and thus constitute the first experimental evidence of quantum monodromy for molecular systems having a champagne bottle potential function. Similar effects were observed earlier by one of us[19] in the microwave spectra of quasi-symmetric top molecules. In particular, in the spectrum of methyl iso-thiocyanate, CH$_3$NCS,[20] rotational transitions were observed arising from molecules in the vibrational CNC bending states both below and above the monodromy point. The characteristic patterns exhibited in the microwave spectra of quasi-symmetric top molecules were discussed in terms of the potential energy function governing two large-amplitude motions, the skeletal bending and the internal rotation of the CH$_3$-group.[19]

For an overview on the subject of monodromy and molecular spectroscopy the reader is referred to recent publications.[2,14,21]

From an historical point of view it is interesting to note that Riemann formulated the concept of monodromy in his work on functions of complex variables and on complex linear differential equations having given singularities and corresponding monodromy transformations.[22] In his lecture at the 1900 International Congress of Mathematicians in Paris, David Hilbert[23,24] included the monodromy-related Riemann problem as Number 21 in his famous list of unsolved problems for twentieth century mathematics.

In the present work a discussion of our NCNCS measurements and their analysis is presented, highlighting the pervasive patterns imposed on all aspects of the spectrum by quantum monodromy. The data pertains to vibrational states in which only the large amplitude bending motion is excited. It should be noted that if the molecule were bent, with no large amplitude bending, the lowest bending mode "would be ν_9", whereas for a linear molecule, in which the three bending modes are degenerate, it "would be ν_7". We therefore use the notation v_b, indicating the one-dimensional or radial vibrational quantum number which is required by both the bent asymmetric rotor and the Generalized Semi-Rigid Bender (GSRB) models. For simplicity, it will be referred to throughout as v_b:

$$v_b = (v_{linear} - |\ell|)/2 \text{ or } v_{linear} = 2v_b + |K_a|, \quad (1)$$

or, in the theoretical section as $v \equiv v_b$. The vibrational quantum number used in a linear model, v_{linear}, relevant for high v_b, can be inferred from eqn (1). The vibrational angular

momentum quantum number ℓ of a linear molecule is identical to k for a symmetric top, which is used here in section 2, while the same quantity is indicated by K_a in discussing the experimental results and the GSRB calculations, since the asymmetric top perspective is necessary in the analysis for the case of non-zero end-over-end rotation.

The remainder of the paper is organized as follows: In section 2 we discuss theoretical considerations: the *ab initio* calculations (2.1) and a description of the GSRB Hamiltonian along with the incorporation of the centrifugal distortion terms (2.2). Section 3 deals with experimental aspects. Section 4 encompasses the data reduction and assignment procedures. Section 5 continues with the data analysis. Sub-section 5.1 provides the determination of effective spectroscopic constants. The resonance interactions observed in the NCNCS spectrum are briefly discussed in Sub-section 5.2 while the GSRB evaluation of the NCNCS results is discussed in Sub-section 5.3 together with the centrifugal distortion contributions. Sub-section 5.4 discusses the effect of monodromy on expectation values of the electric dipole moments and indeed of any physical quantity which depends on the large amplitude bending coordinate ρ, while Sub-section 5.5 clarifies and extends the definition of the quasi-linear parameter. Section 6 presents the conclusions to be drawn from this work.

2. Theoretical considerations

2.1 *Ab initio* calculations, structure, theoretical potential energy function and dipole moments μ_a and μ_b for NCNCS

The molecular structure of NCNCS was calculated using the coupled-cluster method including single and double excitations and a perturbational correction due to connected triple excitations, CCSD(T)[25,26] The one-particle basis sets employed were the correlation-consistent polarized valence basis sets of quadruple- and quintuple-zeta quality, cc-pVQZ and cc-pV5Z.[27] For sulfur, the extended correlation-consistent cc-pV(n + d)Z basis sets were used.[28] In the valence correlation treatment, the 1s-like core orbitals of the carbon and nitrogen atoms and the 1s2sp-like core orbitals of the sulfur atom were excluded from the active space. The core-electron correlation effects were investigated using the correlation-consistent polarized core-valence basis set of quadruple-zeta quality, cc-pCVQZ.[29] The calculations were performed using the MOLPRO-2006 package of *ab initio* programs.[30]

The molecular structure computed for the electronic ground state of NCNCS is given in Table 1. The equilibrium structure of the NCNCS molecule was found to be planar and bent, with the *trans* conformation of both NCNC and CNCS moieties (a W-shaped overall structure). Values of the structural parameters obtained in the valence correlation treatment with the largest basis set, cc-pV5Z, were corrected for the core-electron correlation effects determined at the CCSD(T)/cc-pCVQZ level. The best estimates of the equilibrium parameters of NCNCS obtained in this way are given in the last column of Table 1. Considering convergence of the calculated values with the basis set size and errors inherent to the CCSD(T) method, the predicted equilibrium internuclear distances and bond angles are believed to be accurate to about

Table 1 Molecular parameters of NCNCS determined at the CCSD(T)/cc-pVnZ level of theory

	cc-pVQZ	cc-pV5Z	CC[a]	Equ.[b]
Equilibrium configuration $\rho \neq 0$				
$r_{N_1C_1}$/Å	1.1643	1.1635	−0.0023	1.161
$r_{C_1N_2}$/Å	1.3181	1.3182	−0.0037	1.314
$r_{N_2C_2}$/Å	1.2128	1.2130	−0.0033	1.210
r_{C_2S}/Å	1.5556	1.5540	−0.0033	1.551
$\angle$(NCN)/°	176.33	176.37	+0.13	176.5
$\angle$(CNC)/°	142.32	141.76	+1.23	143.0
$\angle$(NCS)/°	174.33	174.34	+0.21	174.6
Energy/hartree + 583	−0.166197	−0.187546		
Linear configuration $\rho = 0$				
$r_{N_1C_1}$/Å	1.1665	1.1658	−0.0025	
$r_{C_1N_2}$/Å	1.2965	1.2961	−0.0022	
$r_{N_2C_2}$/Å	1.1945	1.1942	−0.0021	
r_{C_2S}/Å	1.5636	1.5621	−0.0037	
$\Delta E/hc$/cm^{-1} [c]	306	330	−45	285

[a] Corrections for the core-electron correlation effects determined at the CCSD(T)/cc-pCVQZ level. [b] Estimated equilibrium values. [c] Energy difference between the linear and equilibrium configurations.

± 0.001 Å and $\pm 0.1°$, respectively. The large change in the CNC angle from the cc-pCVQZ to the cc-pCV5Z basis set shows the importance of the larger basis set for this quasi-linear bending coordinate. Fig. 1 shows this *ab initio* equilibrium structure, which differs slightly from that given in ref. 1. The CNC bond angle $143°$ already suggests that the molecule is flexible or quasilinear, with a low energy bending vibration.

The CNC bending potential energy function was determined by optimizing the structural parameters for various assumed values of the valence angle CNC. All of the structural parameters were found to vary significantly with the CNC angle. In particular, for the CNC moiety, the CN and NC internuclear distances increase nonlinearly with decreasing CNC angle. The differences in the CN and NC internuclear distances amount to 0.052 and 0.042 Å, respectively, when the CNC angle ranges from $180°$ to $120°$.

The CNC bending potential energy function of NCNCS can be characterized by three parameters, namely the equilibrium angle ρ_e, the height of a barrier to linearity H, and the harmonic force constant f (at $\rho = \rho_e$). The best *ab initio* estimates of these parameters obtained in this work are $\rho_e = 37.0°$, $H = 285$ cm^{-1}, and $f = 0.109$ mdyn Å.

Table 2 gives the *ab initio* bending potential energy and the electric dipole moments along the minimum energy path. These were calculated by the finite-field approach at the CCSD(T)/cc-pVQZ level of theory.

Table 2 The *ab initio* CNC bending potential energy function and electric dipole moment components μ_a and μ_b for NCNCS

ρ/deg	$V(\rho)$/cm^{-1}	μ_a/D	μ_b/D
0.0	0.0	2.714	0.000
10.0	−40.0	2.761	0.058
20.0	−141.5	2.895	0.134
30.0	−251.2	3.094	0.292
37.68	−284.5	3.197	0.414
40.0	−276.2	3.320	0.559
50.0	−83.4	3.507	0.929
60.0	494.3	3.580	1.364
70.0	1644.0	3.478	1.814

This journal is © the Owner Societies 2010

Phys. Chem. Chem. Phys., 2010, **12**, 8158–8189 | 8161

2.2 Description of the generalized Semi-Rigid Bender Hamiltonian

The robust properties of the bifurcation of the champagne bottle potential function into two distinct topological spaces (see Fig. 3) at the monodromy point are mapped onto the energy-momentum maps for ro-vibrational energy, and thus onto the experimental spectrum of any quasi-linear molecule. The spectrum allows us to determine physical quantities such as coordinate expectation values, ro-vibrational wave functions, dipole moments *etc.* which depend on the motion of the NCNCS molecule under the influence of the champagne bottle potential associated with the large amplitude bending mode.

For the present analysis of the NCNCS spectrum the Semi-Rigid-Bender (SRB) concept was used since it can handle five-atom chain molecules with relative ease, in contrast to more advanced methods such as variational calculations. The level of approximation offered by SRB calculations reproduces all of the physically significant features of the NCNCS spectrum, even if experimental accuracy cannot quite be achieved. We therefore believe that a brief but thorough discussion of the Generalized Semi-Rigid Bender (GSRB) Hamiltonian as applied to NCNCS should be presented. This is especially true as the initial derivation[31–34] presents the SRB as a simplification of the very much more complicated non-rigid bender. Here we present a derivation which proceeds directly to the SRB.

The usual starting point for studying vibration and rotation in molecules is to introduce normal coordinates for the vibrations. Typically these are initially treated in the harmonic approximation with a rigid-rotor model used for the rotational motion. This initial description can then be improved by considering higher order terms and interactions. However, in the case of large-amplitude vibrational motion this starting point can be quite inappropriate. This is because large-amplitude vibrations are rarely in the direction of the rectilinear displacements inherent in normal coordinates and because the large-amplitude vibrational motion can also have a rotational nature, especially in the case of bending or torsional motion.

In a 1970 paper on the rotation and large-amplitude bending vibration of a triatomic molecule, Hougen, Bunker, and Johns[31] introduced what has come to be known as the HBJ approach. This approach separates the large-amplitude vibration from the other vibrations, instead uniting it with the rotational motion, while the other vibrations are assumed to be of small amplitude. That is, HBJ separates the Hamiltonian into a small-amplitude vibrational part and a rotation + large-amplitude vibrational part. The seminal contribution of HBJ, and the idea which makes this separation possible and enormously efficacious, is the introduction of a *flexible reference configuration*. The reference configuration is defined so as to follow the large-amplitude motion. For example, in the case of a large-amplitude bending vibration the reference configuration bends with the molecule. In this way the reference configuration carries the large-amplitude bending motion of the molecule in the Hamiltonian. The Greek letter ρ is traditionally used to denote the coordinate describing the large-amplitude motion of the reference configuration.

In the HBJ approach the small-amplitude vibrations are not defined in terms of the instantaneous displacements of nuclei away from the equilibrium configuration (already problematic in the case of a molecule with multiple accessible equilibria). Instead they are defined in terms of the instantaneous displacements of the nuclei from the reference configuration, thereby decreasing the magnitude of these displacements.

Bunker and Stone[33] showed how to fully incorporate rotational motion into the HBJ treatment, thus creating the rotating Rigid Bender model. Subsequent work by Hoy and Bunker[34] incorporated the small-amplitude vibrations by Van Vleck perturbation theory, giving the Non-Rigid Bender model. Bunker and Landsberg,[32] inspired by the suggestion of John Hardwick, took a different approach, and allowed the reference configuration itself to "relax" (see below) during the large amplitude vibration. The resulting model, less complete than the Non-Rigid Bender model, but easier to calculate, is known as the Semi-Rigid Bender (SRB). The SRB does not explicitly account for the small amplitude vibrations or centrifugal distortion involving the small-amplitude vibrations. (Note, however, that the small amplitude vibrations can be included in a rough-and-ready way by having the geometry of the reference configuration and the potential energy function depend on the small amplitude vibrational quantum numbers, thus defining an effective SRB Hamiltonian for each excited small amplitude state.) The hope expressed in ref. 32 in developing the SRB was to produce a model which, although not as accurate as the non-rigid bender, could be more easily generalized to larger molecules. This hope has certainly been realized. Nothing in the SRB model restricts it to a bending motion, and indeed it has been used for a variety of different large-amplitude vibrational motions. It is also straightforward, in principle, to extend the HBJ Hamiltonian to more than one large-amplitude vibration. It is not so straightforward, however, to develop the multidimensional large-amplitude vibrational basis functions for that case.

Unlike the more general non-rigid-bender model, the SRB does not consider any displacements of the nuclei away from the reference configuration. Thus, the SRB model can be considered as a stick-figure quantum model, which describes the rotation and large-amplitude vibration of a molecular framework as shown in Fig. 1. The coordinate ρ describes the single large-amplitude motion of the framework. Other features of the framework such as internuclear distances and angles are allowed to "relax" (*i.e.* vary) as functions of ρ. It is this feature that leads to the moniker *semi-rigid* bender. Since small-amplitude vibrational displacements are neglected in the SRB the reference configuration is identical to the instantaneous configuration and therefore Eckart-type and Sayvetz conditions are not needed since those explicitly involve small-amplitude vibrational displacements.[35]

In the present work we use the SRB model, in a form generalized to larger molecules and for an arbitrary but single large-amplitude motion. This form of the SRB has been called the Generalized SRB (GSRB). The actual computational steps performed to solve the SRB Schrödinger equation are outlined in several places (for example in section IV of ref. 36) and will not be repeated in detail here. The derivation of the SRB Hamiltonian for large-amplitude bending of a triatomic molecule can be seen by following through the derivations in

ref. 31–33. However, a somewhat more direct derivation can be presented by taking advantage of the fact that we neglect the small-amplitude vibrations from the outset. This we do here, for the case of a general single large-amplitude vibration in an arbitrary molecule.

The SRB Hamiltonian is derived from the classical Hamiltonian for a vibrating, rotating point mass stick-figure molecule such as that illustrated in Fig. 1. The potential energy in the SRB Hamiltonian is simply a function of the large-amplitude coordinate, $V(\rho)$. We begin in the space-fixed non-rotating center-of-mass frame X,Y,Z. The location of nucleus α in this frame can be written as the vector $\boldsymbol{r}_\alpha(\rho)$, for NCNCS $\alpha = 1, 2, 3, 4, 5$. To solve the Schrödinger equation we work in the center-of-mass molecule-fixed axes frame, shown for NCNCS in Fig. 4. The positions of the nuclei in the molecule-fixed (i.e. rotating) frame x, y, z, are given by the vectors $\boldsymbol{a}_\alpha(\rho)$, which depend explicitly on ρ. Following Bunker and Jensen[37] [eqn (10.5) to (10.7)] we define the direction-cosine matrix $\mathbf{C}$ as that which rotates space-fixed vector components into molecule-fixed components. The inverse (equal to the transpose, denoted by t) of $\mathbf{C}$ then rotates in the opposite direction. Thus, if $\boldsymbol{r}_\alpha$ and $\boldsymbol{a}_\alpha$ are considered as column vectors, the center-of-mass frame space-fixed location of nucleus α is simply $\boldsymbol{r}_\alpha(\rho) = \mathbf{C}^t \boldsymbol{a}_\alpha(\rho)$. The classical kinetic energy for the SRB model is simply evaluated as,

$$T = \frac{1}{2}\sum_\alpha m_\alpha \boldsymbol{v}_\alpha^2 = \frac{1}{2}\sum_\alpha m_\alpha \dot{\boldsymbol{r}}_\alpha^2 = \frac{1}{2}\sum_\alpha m_\alpha \dot{\boldsymbol{r}}_\alpha^t \dot{\boldsymbol{r}}_\alpha$$

$$= \frac{1}{2}\sum_\alpha m_\alpha \left[\frac{\mathrm{d}}{\mathrm{d}t}(\mathbf{C}^t \boldsymbol{a}_\alpha)\right]^t \left[\frac{\mathrm{d}}{\mathrm{d}t}(\mathbf{C}^t \boldsymbol{a}_\alpha)\right]$$

$$= \frac{1}{2}\sum_\alpha m_\alpha \boldsymbol{a}_\alpha^t \dot{\mathbf{C}}\dot{\mathbf{C}}^t \boldsymbol{a}_\alpha \qquad (2)$$

$$+ \frac{1}{2}\sum_\alpha m_\alpha [\boldsymbol{a}_\alpha^t \dot{\mathbf{C}}\mathbf{C}^t \boldsymbol{a}_\alpha + \dot{\boldsymbol{a}}_\alpha^t \mathbf{C}\dot{\mathbf{C}}^t \boldsymbol{a}_\alpha]$$

$$+ \frac{1}{2}\sum_\alpha m_\alpha \dot{\boldsymbol{a}}_\alpha^t \mathbf{C}\mathbf{C}^t \dot{\boldsymbol{a}}_\alpha,$$

where m_α is the mass of nucleus α and where we remember that in the SRB model the small-amplitude displacements from the reference configuration are neglected (i.e. fixed to 0). Standard
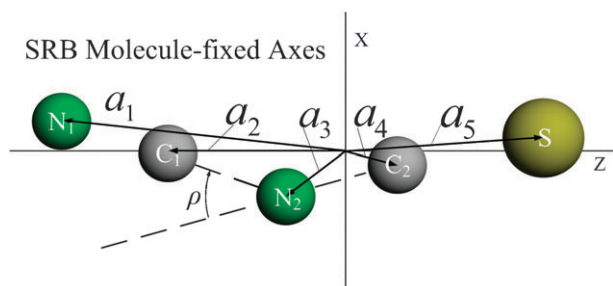
Fig. 4 SRB molecule-fixed-axes x,y,z for NCNCS. The origin of the x, y, z coordinate system is at the center of mass. The y coordinate is perpendicular to the x, z plane and is not drawn. The positions of the nuclei in the molecule-fixed frame are given by the vectors $\boldsymbol{a}_\alpha$, where $\alpha = 1, 2, 3, 4, 5$. These vectors depend on the large amplitude coordinate ρ.

but careful evaluation shows that the elements of the rotation matrix product factors in eqn (2) can be written,

$$[\dot{\mathbf{C}}\dot{\mathbf{C}}^t]_{i,j} = \delta_{i,j}\boldsymbol{\omega}^2 - \omega_i\omega_j,$$

$$[\dot{\mathbf{C}}\mathbf{C}^t]_{i,j} = -[\mathbf{C}\dot{\mathbf{C}}^t]_{i,j} = \sum_k \varepsilon_{i,j,k}\omega_k, \qquad (3)$$

$$[\mathbf{C}\mathbf{C}^t]_{i,j} = \delta_{i,j},$$

where $\delta_{i,j}$ is the Kronecker delta and $\varepsilon_{i,j,k}$ is the Levi–Civita tensor. $\boldsymbol{\omega}$ is the angular velocity vector of the rotating SRB molecular framework relative to the laboratory-fixed axes. The components ω_i of $\boldsymbol{\omega}$ are the projections of the vector $\boldsymbol{\omega}$ onto the SRB molecule-fixed axes x, y, z. We know that the elements of the moment of inertia tensor are

$$I_{i,j}(\rho) = I_{j,i}(\rho) = \sum_\alpha m_\alpha(\delta_{i,j}\boldsymbol{a}_\alpha^2 - \boldsymbol{a}_{\alpha,i}\boldsymbol{a}_{\alpha,j}), \qquad (4)$$

for $i, j = x, y, z$, where $\boldsymbol{a}_{\alpha,i}$ is the ith component of $\boldsymbol{a}_\alpha(\rho)$. Eqn (3) and (4) allow one to re-express each of the three terms in the last line of eqn (2) to give the simple form for the SRB kinetic energy operator,

$$T = \frac{1}{2}\boldsymbol{\omega}^t \boldsymbol{I}\boldsymbol{\omega} + \boldsymbol{\omega} \cdot \sum_\alpha m_\alpha(\boldsymbol{a}_\alpha \times \dot{\boldsymbol{a}}_\alpha) + \frac{1}{2}\sum_\alpha m_\alpha(\dot{\boldsymbol{a}}_\alpha)^2$$

$$= T_{\text{rotation}} + T_{\text{Coriolis}} + T_{\text{LAvib}}. \qquad (5)$$

Here $\boldsymbol{I}$ is the standard moment of inertia tensor for the reference configuration and which therefore depends on ρ, and where we remember from Fig. 4 that the $\boldsymbol{a}_\alpha(\rho)$ are the locations of the atoms in the SRB molecule-fixed axes system. Other than minor differences in notation eqn (5) is equivalent to eqn (7) and (8) of section 11-1 of Wilson, Decius, and Cross[38] for a single vibration, noting that those authors do not include the customary minus sign in their definitions of the off-diagonal elements of the moment of inertia tensor. We can now take account of the fact that the time dependence of the $\boldsymbol{a}_\alpha(\rho)$ is implicit in this notation, being only through their dependence on ρ. Thus,

$$\dot{\boldsymbol{a}}_\alpha = \frac{\mathrm{d}\boldsymbol{a}_\alpha}{\mathrm{d}t} = \frac{\mathrm{d}\boldsymbol{a}_\alpha}{\mathrm{d}\rho}\dot{\rho}, \qquad (6)$$

and we obtain

$$T_{\text{Coriolis}} = (\dot{\rho}\boldsymbol{\omega}) \cdot \left[\sum_\alpha m_\alpha\left(\boldsymbol{a}_\alpha \times \frac{\mathrm{d}\boldsymbol{a}_\alpha}{\mathrm{d}\rho}\right)\right]. \qquad (7)$$

Hougen, Bunker and Johns[31] realized that this term can be incorporated into an extended version of T_{rotation} from eqn (5) by extending the moment of inertia to a fourth dimension relating to the large-amplitude coordinate. First, a fourth *angular velocity* component is introduced,

$$\omega_\rho = \dot{\rho}. \qquad (8)$$

Then by defining the following three pairs of *new* off-diagonal elements of the moment of inertia tensor,

$$I_{i,\rho}(\rho) = I_{\rho,i}(\rho) = \sum_\alpha m_\alpha\left(\boldsymbol{a}_\alpha \times \frac{\mathrm{d}\boldsymbol{a}_\alpha}{\mathrm{d}\rho}\right)_i, \qquad (9)$$

This journal is © the Owner Societies 2010

Phys. Chem. Chem. Phys., 2010, **12**, 8158–8189 | 8163

for $i = x, y, z$, eqn (7) can be written as

$$T_{\text{Coriolis}} = \dot{\rho} \sum_i \omega_i \left[\sum_\alpha m_\alpha \left(\boldsymbol{a}_\alpha \times \frac{\mathrm{d}\boldsymbol{a}_\alpha}{\mathrm{d}\rho} \right)_i \right]$$

$$= \sum_i \omega_i I_{i,\rho} \omega_\rho \qquad (10)$$

$$= \frac{1}{2} \sum_i (\omega_i I_{i,\rho} \omega_\rho + \omega_\rho I_{\rho,i} \omega_i).$$

Similarly, by defining

$$I_{\rho,\rho}(\rho) = \sum_\alpha m_\alpha \left(\frac{\mathrm{d}\boldsymbol{a}_\alpha}{\mathrm{d}\rho} \right)^2, \qquad (11)$$

and again using eqn (6) and (8), we can re-express the kinetic energy of the *large amplitude vibration* T_{LAvib},

$$T_{\text{LAvib}} = \frac{1}{2} \sum_\alpha m_\alpha (\dot{\boldsymbol{a}}_\alpha)^2 = \frac{1}{2} \sum_\alpha m_\alpha \left(\frac{\mathrm{d}\boldsymbol{a}_\alpha}{\mathrm{d}\rho} \dot{\rho} \right)^2$$

$$= \frac{1}{2} \sum_\alpha m_\alpha \left(\frac{\mathrm{d}\boldsymbol{a}_\alpha}{\mathrm{d}\rho} \right)^2 \omega_\rho^2 \qquad (12)$$

$$= \frac{1}{2} \omega_\rho \boldsymbol{I}_{\rho,\rho} \omega_\rho.$$

Still following HBJ the symmetric extended 4×4 matrix $\tilde{\boldsymbol{I}}$ and the 4-vector $\tilde{\boldsymbol{\omega}}$ can be defined as,

$$\tilde{\boldsymbol{I}}(\rho) = \begin{bmatrix} \tilde{I}_{x,x} & \tilde{I}_{x,y} & \tilde{I}_{x,z} & \tilde{I}_{x,\rho} \\ \tilde{I}_{y,x} & \tilde{I}_{y,y} & \tilde{I}_{y,z} & \tilde{I}_{y,\rho} \\ \tilde{I}_{z,x} & \tilde{I}_{z,y} & \tilde{I}_{z,z} & \tilde{I}_{z,\rho} \\ \tilde{I}_{\rho,x} & \tilde{I}_{\rho,y} & \tilde{I}_{\rho,z} & \tilde{I}_{\rho,\rho} \end{bmatrix}, \ \tilde{\boldsymbol{\omega}} = \begin{bmatrix} \tilde{\omega}_x \\ \tilde{\omega}_y \\ \tilde{\omega}_z \\ \tilde{\omega}_\rho \end{bmatrix}, \qquad (13)$$

where the elements of $\tilde{\boldsymbol{I}}$ are taken from eqn (4), (9) and (11) and those of $\tilde{\boldsymbol{\omega}}$ are simply ω_x, ω_y, ω_z, and from eqn (8), ω_ρ. Using eqn (10) and (12) in eqn (5) then gives the final and very pleasing form for the classical kinetic energy and thus the Hamiltonian for a rotating nuclear framework undergoing a single large-amplitude vibration,

$$T = \frac{1}{2} \tilde{\boldsymbol{\omega}}^t \tilde{\boldsymbol{I}} \tilde{\boldsymbol{\omega}}, \qquad (14)$$

so,

$$H = T + V(\rho) = \frac{1}{2} \tilde{\boldsymbol{\omega}}^t \tilde{\boldsymbol{I}} \tilde{\boldsymbol{\omega}} + V(\rho). \qquad (15)$$

In this expression the large-amplitude vibration is treated equivalently with the rotational motion.

The next step is to convert the Hamiltonian of eqn (15) to a form involving momenta rather than angular velocities. The classical generalized momenta conjugate to the components of $\tilde{\boldsymbol{\omega}}$ are,

$$p_r = \frac{\partial T}{\partial \omega_r}, \ r = x, y, z, \rho. \qquad (16)$$

The first three of these are easily shown to be the molecule-fixed components of the total angular momentum,

$$p_i = J_i, \ i = x, y, z \qquad (17)$$

(see eqn (1)–(3) of ref. 38). The fourth component J_ρ is simply defined as,

$$J_\rho = p_\rho = \frac{\partial T}{\partial \omega_\rho}$$

$$= \tilde{I}_{x,\rho} \tilde{\omega}_x + \tilde{I}_{y,\rho} \tilde{\omega}_y + \tilde{I}_{z,\rho} \tilde{\omega}_z + \tilde{I}_{\rho,\rho} \tilde{\omega}_\rho. \qquad (18)$$

Defining the four-vector $\tilde{\boldsymbol{J}}$ as the column vector $[\tilde{J}_x, \tilde{J}_y, \tilde{J}_z, \tilde{J}_\rho]^t$ [where these elements of $\tilde{\boldsymbol{J}}$ are simply J_x, J_y, J_z, and J_ρ from eqn (18)] we can write,

$$\tilde{\boldsymbol{J}} = \tilde{\boldsymbol{I}} \tilde{\boldsymbol{\omega}}, \text{ or } \tilde{\boldsymbol{\omega}} = \tilde{\boldsymbol{I}}^{-1} \tilde{\boldsymbol{J}} = \tilde{\boldsymbol{\mu}} \tilde{\boldsymbol{J}}, \text{ where } \tilde{\boldsymbol{\mu}}(\rho) = \tilde{\boldsymbol{I}}^{-1}(\rho), \quad (19)$$

(as long as $\tilde{\boldsymbol{I}}$ is not singular). Eqn (15) can now be written in terms of momenta as,

$$H = T + V(\rho) = \frac{1}{2} \tilde{\boldsymbol{J}}^t \tilde{\boldsymbol{\mu}} \tilde{\boldsymbol{J}} + V(\rho). \qquad (20)$$

Boris Podolsky[39] pointed out that writing the classical Hamiltonian in a particular form allows one to immediately interpret the same form as the quantum mechanical Hamiltonian, provided that each classical momentum p_i is now interpreted as the quantum mechanical operator $-i\hbar(\partial/\partial q_i)$, where p_i is the momentum conjugate to the generalized coordinate q_i. Sometimes known as the *Podolsky Trick*, this process represents the transformation of the Laplacian operator from Cartesian coordinates to the generalized coordinates being used, avoiding the need to explicitly perform the transformation of the differential operators. Taking into account normalisation, the "Podolsky" form of the Hamiltonian becomes (see for example eqn (9.30) of Bunker and Jensen[37]),

$$H = \frac{1}{2} s^{-1/2} g^{1/4} \left[\sum_{i,j} p_i g^{-1/2} g^{i,j} p_j \right] g^{1/4} s^{1/2} + V(\rho). \qquad (21)$$

Here g is the determinant of the matrix $g^{i,j}$ and s is the volume element weight factor to be used in the integration of the wave functions for normalisation or other purposes (for example, in spherical coordinates, the volume element is typically chosen as $r^2 \sin\theta \, \mathrm{d}r\mathrm{d}\theta\mathrm{d}\varphi$ in which case $s = r^2 \sin\theta$). The SRB approach uses the volume element $\mathrm{d}\rho(\sin\theta) \, \mathrm{d}\theta\mathrm{d}\varphi\mathrm{d}\chi$ of HBJ, where θ, φ, χ are the Euler angles for the orientation of the molecule-fixed axes relative to the space-fixed axes, so that $s = \sin\theta$.

The Podolsky form of the classical Hamiltonian in eqn (21) is the one that can immediately be re-interpreted as the quantum Hamiltonian, provided that the classical momenta appearing there are those conjugate to the coordinates (θ, φ, χ, ρ, in our case) and that when eqn (21) is then re-interpreted as the quantum form the momenta are the differential operators related to the coordinates $\left[-i\hbar\left(\frac{\partial}{\partial\theta}\right), -i\hbar\left(\frac{\partial}{\partial\varphi}\right), -i\hbar\left(\frac{\partial}{\partial\chi}\right), -i\hbar\left(\frac{\partial}{\partial\rho}\right), \text{ in our case} \right]$. However, in eqn (20) the classical SRB Hamiltonian is expressed in terms of the classical angular momenta $\tilde{J}_x$, $\tilde{J}_y$, $\tilde{J}_z$, and $\tilde{J}_\rho$ which are related to the angular velocities $\tilde{\omega}_x$, $\tilde{\omega}_y$, $\tilde{\omega}_z$, and $\tilde{\omega}_\rho$, rather than to the coordinates. Except for $\tilde{J}_\rho$, these angular momenta are not conjugate to the coordinates. Therefore, to use eqn (21) as the bridge between classical and quantum mechanics, the classical SRB Hamiltonian of eqn (20) must first be re-expressed in terms of momenta conjugate to the coordinates. Similarly, we would like the quantum

8164 | *Phys. Chem. Chem. Phys.*, 2010, **12**, 8158–8189

This journal is © the Owner Societies 2010

Hamiltonian to be in terms of the quantum angular momentum operators, rather than the operators $-i\hbar\left(\frac{\partial}{\partial\theta}\right)$, *etc.* This means that the resulting quantum SRB Hamiltonian must in turn be re-expressed to obtain the desired form. Doing this while also accounting for the factor $s = \sin\theta$ is a very involved process which, except for the appearance of the ρ-related angular momentum, is part of the standard development of the molecular vibration–rotation Hamiltonian. We skip this part of the derivation as it can be done following the standard treatment which can be found in various places, in particular the nice review by Meyer.[40]

Quite surprisingly, the quantum SRB Hamiltonian obtained by correctly accounting for the $\sin\theta$ factor and doing the conversions back and forth of the momenta is identical to simply cancelling out the s factors in eqn (21) and interpreting the momenta appearing therein as the quantum mechanical angular momenta. That is, it turns out that the desired quantum form of the SRB Hamiltonian in terms of angular momentum operators is the same as eqn (21) with the s factors removed and with the various g factors identified by direct comparison with the SRB classical Hamiltonian of eqn (20). Doing this identification, while requiring $g^{i,j} = g^{j,i}$, immediately gives $g^{i,j}(\rho) = \tilde{\mu}_{i,j}(\rho)$. Similarly, the determinant, g, in eqn (21) becomes simply $g = \tilde{\mu}$, the determinant of the 4×4 $\tilde{\mu}_{i,j}$ matrix. The Podolsky form of the SRB Hamiltonian is now,

$$\hat{H}_{\text{SRB}} = \frac{1}{2}\tilde{\mu}^{1/4}\left[\sum_{r,s}\hat{J}_r\tilde{\mu}^{-1/2}\tilde{\mu}_{r,s}\hat{J}_s\right]\tilde{\mu}^{1/4} + V(\rho) \qquad (22)$$

with $r, s = x, y, z, \rho$. $\hat{J}_i$ with $i = x, y, z$ are the usual angular momentum operator components $\hat{J}_x, \hat{J}_y, \hat{J}_z$, and $\hat{J}_\rho = -i\hbar(\partial/\partial\rho)$. (Note that HBJ[31] does not explicitly refer to the SRB model. However, the kinetic energy operator given in their eqn (28) is that appropriate for the SRB if the small-amplitude vibrational coordinates and angular momenta are fixed to zero and if the full ρ-dependence of $\tilde{\mu}$ is accounted for.)

The form of $\hat{H}_{\text{SRB}}$ given in eqn (22) is somewhat awkward because $\tilde{\mu}_{r,s}$ and $\tilde{\mu}$ depend on ρ and therefore do not commute with $\hat{J}_\rho$. Eqn (35) of HBJ[31] reformulates this expression by carefully accounting for the commutation relationships to obtain,

$$\hat{H}_{\text{SRB}} = \frac{1}{2}\sum_{r,s}\tilde{\mu}_{r,s}\hat{J}_r\hat{J}_s + \frac{1}{2}\sum_s[\hat{J}_\rho\tilde{\mu}_{\rho,s}]\hat{J}_s$$
$$+ \frac{1}{2}\tilde{\mu}^{1/4}\{\hat{J}_\rho\tilde{\mu}_{\rho,\rho}\tilde{\mu}^{-1/2}[\hat{J}_\rho\tilde{\mu}^{1/4}]\} + V(\rho), \qquad (23)$$

with $r, s = x, y, z, \rho$. In this expression the $\hat{J}_\rho$ operators in square or curly brackets only act within the brackets, *e.g.* $[\hat{J}_\rho\tilde{\mu}^{1/4}] = -i\hbar(\partial\tilde{\mu}^{1/4}/\partial\rho)$. The last two terms before $V(\rho)$ are purely quantum mechanical terms arising from the dependence of the elements of $\tilde{\mu}$ on ρ.

The SRB Schrödinger equation is,

$$\hat{H}_{\text{SRB}}\Psi_{\text{SRB}}(\rho, \theta, \varphi, \chi) = E\Psi_{\text{SRB}}(\rho, \theta, \varphi, \chi). \qquad (24)$$

This equation is solved in the same manner as the Rigid Bender,[33] as also outlined in section IV A of ref. 36. First the Hamiltonian operator is partitioned into two parts, a large-amplitude vibration + z-axis rotation part, and the remainder which includes all the terms involving rotation about the x or y-axes,

$$\hat{H}_{\text{SRB}} = \hat{H}_{\text{LAvib}+z\text{-rotation}} + \hat{H}_{x-y\text{-rotation}},$$

$$\hat{H}_{\text{LAvib}+z\text{-rotation}} = \frac{1}{2}\tilde{\mu}_{\rho,\rho}\hat{J}_\rho^2 + \frac{1}{2}[\hat{J}_\rho\tilde{\mu}_{\rho,\rho}]\hat{J}_\rho + \frac{1}{2}\tilde{\mu}_{z,z}\hat{J}_z^2$$
$$+ \frac{1}{2}\tilde{\mu}^{1/4}\{\hat{J}_\rho\tilde{\mu}_{\rho,\rho}\tilde{\mu}^{-1/2}[\hat{J}_\rho\tilde{\mu}^{1/4}]\} + V(\rho),$$

$$\hat{H}_{x-y\text{-rotation}} = \frac{1}{2}\sum_{i,j\neq z,z}\tilde{\mu}_{i,j}\hat{J}_i\hat{J}_j + \sum_i\tilde{\mu}_{i,\rho}\hat{J}_i\hat{J}_\rho$$
$$+ \frac{1}{2}\sum_i[\hat{J}_\rho\tilde{\mu}_{\rho,i}]\hat{J}_i, \quad i,j = x, y, z.$$
$$(25)$$

The solution of the SRB Schrödinger eqn (24) is done in two steps:

Step 1: A Large-Amplitude + z-rotation basis set is obtained by solving the Schrödinger equation,

$$\hat{H}_{\text{LAvib}+z\text{-rotation}}\Psi_{k,v}(\rho, \chi) = E_{k,v}\Psi_{k,v}(\rho, \chi) \qquad (26)$$

for the product wave function,

$$\Psi_{k,v}(\rho, \chi) = \frac{1}{\sqrt{2\pi}}e^{ik\chi}\psi_{k,v}(\rho), \qquad (27)$$

where k is the quantum number associated with the rotation about the z-axis while v corresponds to the LA-bending quantum number. (Note: This corresponds to the definition of v for a bent molecule, or the radial quantum number n when described in polar coordinates for a linear molecule.) This leads to a second order differential equation for $\psi_{k,v}(\rho)$. The LA + z-rotation part contains $\partial/\partial\rho$ and $\partial^2/\partial\rho^2$ terms (through $\hat{J}_\rho$ and $\hat{J}_\rho^2$). However, in the HBJ approach the solution of the ρ-dependent part of the Schrödinger equation relies on the Numerov–Cooley technique (ref. 41 and 42 and references therein) which requires that the differential equation only contain a second order derivative. The first derivative term in eqn (26) can be removed by the standard substitution,

$$\psi_{k,v}(\rho) = \frac{1}{\sqrt{\tilde{\mu}_{\rho,\rho}(\rho)}}\varphi_{k,v}(\rho), \qquad (28)$$

which leads to the equation for $\varphi_{k,v}(\rho)$,

$$\frac{\partial^2}{\partial\rho^2}\varphi_{k,v}(\rho) = \left\{f_1(\rho) + k^2f_2(\rho) - \frac{2}{\hbar^2\tilde{\mu}_{\rho,\rho}(\rho)}[E_{k,v} - V(\rho)]\right\}\varphi_{k,v}(\rho), \qquad (29)$$

where

$$f_1(\rho) = \frac{\tilde{\mu}(\rho)^{1/4}}{\tilde{\mu}_{\rho,\rho}(\rho)^{1/2}}\frac{\partial^2}{\partial\rho^2}\left\{\frac{\tilde{\mu}_{\rho,\rho}(\rho)^{1/2}}{\tilde{\mu}(\rho)^{1/4}}\right\},$$
$$f_2(\rho) = \frac{\tilde{\mu}_{z,z}(\rho)}{\tilde{\mu}_{\rho,\rho}(\rho)}. \qquad (30)$$

For each value of $|k|$ eqn (29) can readily be solved by the Numerov–Cooley technique to give the set of energies, $E_{k,v}$, and functions, $\varphi_{k,v}$, for as many vibrational levels as needed.

This journal is © the Owner Societies 2010

Phys. Chem. Chem. Phys., 2010, **12**, 8158–8189 | 8165

Eqn (28) followed by eqn (27) then yields the basis functions $\Psi_{k,v}(\rho,\chi)$. If the molecule passes through the linear configuration, as is the case for NCNCS, the $\tilde{\mu}$ matrix becomes singular. This can be handled by series solution in the region near the singularities and using these solutions as starting values for the Numerov–Cooley technique for regular regions.

Step 2: The product basis functions $\Psi_{k,v}(\rho, \chi)$ of eqn (27) are multiplied by "end-over-end" rotational factors, that is by the θ, φ parts, $S_{Jkm}(\theta, \varphi)$, of the normalized symmetric rotor wave functions, to give the full SRB basis functions of eqn (14) of Bunker and Stone,[33]

$$\Psi_{J,k,m,v}(\theta, \varphi, \chi, \rho) = S_{j,k,m,}(\theta, \varphi)\Psi_{k,v}(\rho, \chi) = |Jkm\rangle\psi_{k,v}(\rho), \quad (31)$$

where $|Jkm\rangle$ are normalized symmetric top wave functions and where the $\psi_{k,v}(\rho)$ are independent of the sign of k since eqn (29) depends on k^2.

The second step in the solution of the SRB problem is, for each J, to calculate the matrix representation of the SRB Hamiltonian of eqn (25), $\langle\Psi_{J,k',m,v'}|\hat{H}_{\mathrm{SRB}}|\Psi_{J,k,m,v}\rangle$, and to use standard matrix techniques to calculate the SRB eigenvalues and eigenvectors. $\hat{H}_{\mathrm{SRB}}$ is not only diagonal in m but independent of m which can therefore be neglected. One slight complication in calculating the matrix elements is that the terms in the second summation of $\hat{H}_{x-y\text{-rotation}}$ in eqn (25) require the derivatives of the $\psi_{k,v}(\rho)$ basis functions with respect to ρ. These can easily and accurately be obtained using the technique of Blatt.[43]

The evaluation of the matrix representation of the SRB Hamiltonian of eqn (25), using the basis functions obtained from the solution of eqn (29) [which itself requires the evaluation of the f_1 and f_2 functions of eqn (30)] clearly requires the evaluation of the elements of the extended inverse moment of inertia matrix $\tilde{\mu}$, of the first and second derivatives with respect to ρ of some of these terms and of the determinant of $\tilde{\mu}$, $\tilde{\mu}$. However, eqn (9) and (11) show that elements of the $\tilde{I}$ matrix in row or column ρ involve $(d\boldsymbol{a}_\alpha/d\rho)$. Thus the SRB Hamiltonian can be written in terms of the $\boldsymbol{a}_\alpha$ and their first through *third* derivatives with respect to ρ. To facilitate the calculation of this Hamiltonian ref. 8 introduced the "axes-of-convenience": x', y', z'. This axis-set can be attached to any convenient point of the molecule (or near the molecule) and oriented as desired. For example in the case of the large-amplitude CNC bending motion of NCNCS the axes-of-convenience were chosen to be centered on the central nitrogen nucleus and oriented along one of the NC bonds as shown in Fig. 5(b). Relative to the axes-of-convenience we denote the instantaneous position of each nucleus by a ρ-dependent vector, $\boldsymbol{b}_\alpha(\rho)$ for $\alpha = 1, 2, 3\ldots, N$, where N is the number of atoms in the molecule. We also introduce $\boldsymbol{R}(\rho)$ as the location of the molecular center-of-mass in the x', y', z' axis-system. It is straightforward to specify the x', y', z' components of the $\boldsymbol{b}_\alpha(\rho)$ vectors in terms of the internuclear distances $r_i(\rho)$ and the bond angles $\alpha_i(\rho)$. (These physical parameters may be constant or they may be functions of ρ.) As examples, for the axes-of-convenience chosen for NCNCS, Fig. 5(b) shows that $\boldsymbol{b}_3(\rho) = \boldsymbol{0}$ and $\boldsymbol{b}_4(\rho) = r_{\mathrm{N_2C_2}}(\rho)\hat{z}'$, where the internuclear distance may depend on ρ.
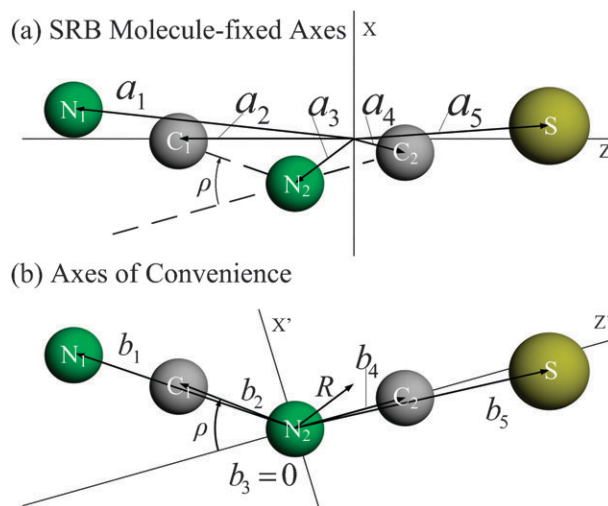
Fig. 5 (a) SRB molecule-fixed-axes and (b) axes of convenience for NCNCS. The vectors $\boldsymbol{b}_\alpha$ give the locations of the nuclei relative to the axes of convenience. The vector $\boldsymbol{R}$ points to the location of the center of mass, while all $\boldsymbol{a}_\alpha$ are relative to the SRB molecule-fixed axes.

As seen in Fig. 5(a) the SRB molecule-fixed axes can be rotated relative to the axes-of-convenience. This rotation can depend on ρ. We introduce the matrix $\mathscr{E}(\rho)$ for this rotation, so that the relationship between the SRB molecule fixed axes position vectors, $\boldsymbol{a}_\alpha$, and the axes-of convenience position vectors, $\boldsymbol{b}_\alpha$, is given by,

$$\boldsymbol{a}_\alpha(\rho) = \mathscr{E}(\rho)[\boldsymbol{b}_\alpha(\rho) - \boldsymbol{R}(\rho)]. \quad (32)$$

The $\mathscr{E}(\rho)$ rotation can be used to force some of the elements in the $\tilde{\mu}$ matrix to zero, $\tilde{\mu}_{r,s}(\rho) = 0$. Depending on the problem at hand, the following three choices of $\mathscr{E}(\rho)$ rotation have been used in GSRB calculations: (a) $\mathscr{E}(\rho) =$ identity, which means the SRB molecule-fixed axes are locked to the axes of convenience, (b) $\mathscr{E}(\rho)$ chosen so that the SRB molecule-fixed axes are principal axes, and, in the case of planar molecules, (c) $\mathscr{E}(\rho)$ chosen so that $\tilde{\mu}_{y,\rho}(\rho) = \tilde{\mu}_{\rho,y}(\rho) = 0$ for all ρ. Since $\tilde{\mu}_{x,\rho}(\rho)$ and $\tilde{\mu}_{z,\rho}(\rho)$ are identically zero for planar molecules, the HBJ axes of choice (c) result in the elimination of the rotation-large-amplitude vibrational coupling caused by the operator products $\hat{J}_x\hat{J}_\rho$, $\hat{J}_y\hat{J}_\rho$, and $\hat{J}_z\hat{J}_\rho$. This is the axis choice in the current work. Note that HBJ-axes can be generalized to non-planar molecules and that other choices of $\mathscr{E}(\rho)$ are possible as well.

If a molecule becomes linear at some point in its large-amplitude motion it is crucial that $\mathscr{E}(\rho)$ be chosen so that at that point the z-axis lies along the molecule. Otherwise the singularity in μ will interfere with the calculation of the $\hat{H}_{\mathrm{SRB}}$ matrix elements, rather than being subsumed in the solution of eqn (29).

All the elements of the SRB Hamiltonian matrix are specified by the atomic masses and the nuclear coordinates $\boldsymbol{a}_\alpha$ and their dependence on the large amplitude coordinate ρ. We can express these elements in terms of matrix products by taking $\boldsymbol{a}_\alpha$, $\boldsymbol{b}_\alpha$, and $\boldsymbol{R}$ as column vectors and defining the arrays

$\boldsymbol{A} = [\boldsymbol{a}_1, \ldots, \boldsymbol{a}_N]$, $\boldsymbol{B} = [\boldsymbol{b}_1, \ldots, \boldsymbol{b}_N]$, $\boldsymbol{R} = [\boldsymbol{R}, \ldots, \boldsymbol{R}]$, and

$$\boldsymbol{M} = \begin{bmatrix} m_1 & 0 & \cdots & 0 \\ 0 & m_2 & \cdots & 0 \\ \vdots & \vdots & \ddots & \vdots \\ 0 & 0 & \cdots & m_N \end{bmatrix}, \tag{33}$$

where $\boldsymbol{M}$ is the matrix of the masses of the individual nuclei in the molecule, so that,

$$\boldsymbol{A} = \mathscr{E}(\rho)\,(\boldsymbol{B} - \boldsymbol{R}). \tag{34}$$

With this notation we can write the elements of the standard symmetric 3×3 moment of inertia tensor of eqn (4) as

$$\begin{aligned}
\tilde{I}_{x,x} &= +[\boldsymbol{AMA}^t]_{y,y} + [\boldsymbol{AMA}^t]_{z,z}, \\
\tilde{I}_{y,y} &= +[\boldsymbol{AMA}^t]_{x,x} + [\boldsymbol{AMA}^t]_{z,z}, \\
\tilde{I}_{z,z} &= +[\boldsymbol{AMA}^t]_{x,x} + [\boldsymbol{AMA}^t]_{y,y}, \\
\tilde{I}_{x,y} &= -[\boldsymbol{AMA}^t]_{x,y}, \\
\tilde{I}_{x,z} &= -[\boldsymbol{AMA}^t]_{x,z}, \\
\tilde{I}_{y,z} &= -[\boldsymbol{AMA}^t]_{y,z},
\end{aligned} \tag{35}$$

(Where all matrix products $\boldsymbol{AMA}^t$ with an index y are zero in the case of a two-dimensional molecule in the x, z plane). Using a prime $'$ to denote differentiation with respect to ρ, the extra elements in the symmetric 4×4 extended moment of inertia matrix $\tilde{\boldsymbol{I}}$ can be written in the following (and other) ways,

$$\begin{aligned}
\tilde{I}_{x,\rho} &= +[\boldsymbol{A'MA}^t]_{z,y} - [\boldsymbol{A'MA}^t]_{y,z}, \\
\tilde{I}_{y,\rho} &= +[\boldsymbol{A'MA}^t]_{x,z} - [\boldsymbol{A'MA}^t]_{z,x}, \\
\tilde{I}_{z,\rho} &= +[\boldsymbol{A'MA}^t]_{y,x} - [\boldsymbol{A'MA}^t]_{x,y}, \\
\tilde{I}_{\rho,\rho} &= +[\boldsymbol{A'MA'}^t]_{x,x} + [\boldsymbol{A'MA'}^t]_{y,y} + [\boldsymbol{A'MA'}^t]_{z,z}.
\end{aligned} \tag{36}$$

For a planar molecule such as NCNCS the simple form of the moment of inertia tensor means that choosing the rotation $\mathscr{E}(\rho)$ so that $\tilde{I}_{y,\rho}(\rho) = \tilde{I}_{\rho,y}(\rho) = 0$ is enough to guarantee that $\tilde{\mu}_{y,\rho}(\rho) = \tilde{\mu}_{\rho,y}(\rho) = 0$, i.e. that the SRB axes are HBJ axes. In the planar case only one angle is needed to specify the relative orientation of the SRB-molecule-fixed axes and the axes of convenience shown in Fig. 5(b). Denoting this angle ε, the derivative of the coordinate array $\boldsymbol{A}$ is then

$$\begin{aligned}
\boldsymbol{A}' &= \frac{\mathrm{d}}{\mathrm{d}\rho}\mathscr{E}(\rho)(\boldsymbol{B} - \boldsymbol{R}) \\
&= \varepsilon'\mathscr{E}^{(1)}(\boldsymbol{B} - \boldsymbol{R}) + \mathscr{E}(\boldsymbol{B}' - \boldsymbol{R}')
\end{aligned} \tag{37}$$

where $\mathscr{E}(\rho) \equiv \mathscr{E}$, and,

$$\mathscr{E}(\rho)^{(1)} \equiv \mathscr{E}^{(1)} = \frac{\mathrm{d}}{\mathrm{d}\varepsilon}\mathscr{E}. \tag{38}$$

Thus for a planar molecule the HBJ axes are obtained if

$$\begin{aligned}
0 = I_{y,\rho} &= [\boldsymbol{A'MA}^t]_{x,z} - [\boldsymbol{A'MA}^t]_{z,x} \\
&= +\varepsilon'[\mathscr{E}^{(1)}(\boldsymbol{B} - \boldsymbol{R})\boldsymbol{M}(\boldsymbol{B} - \boldsymbol{R})^t\mathscr{E}^t]_{x,z} \\
&\quad - \varepsilon'[\mathscr{E}^{(1)}(\boldsymbol{B} - \boldsymbol{R})\boldsymbol{M}(\boldsymbol{B} - \boldsymbol{R})^t\mathscr{E}^t]_{z,x} \\
&\quad + [\mathscr{E}(\boldsymbol{B}' - \boldsymbol{R}')\boldsymbol{M}(\boldsymbol{B} - \boldsymbol{R})^t\mathscr{E}^t]_{x,z} \\
&\quad - [\mathscr{E}(\boldsymbol{B}' - \boldsymbol{R}')\boldsymbol{M}(\boldsymbol{B} - \boldsymbol{R})^t\mathscr{E}^t]_{z,x},
\end{aligned} \tag{39}$$

leading to the condition on ε' for the HBJ axes for planar molecules,

$$\varepsilon' = -\frac{[\mathscr{E}(\boldsymbol{B}' - \boldsymbol{R}')\boldsymbol{M}(\boldsymbol{B} - \boldsymbol{R})^t\mathscr{E}^t]_{x,z} - [\mathscr{E}(\boldsymbol{B}' - \boldsymbol{R}')\boldsymbol{M}(\boldsymbol{B} - \boldsymbol{R})^t\mathscr{E}^t]_{z,x}}{[\mathscr{E}^{(1)}(\boldsymbol{B} - \boldsymbol{R})\boldsymbol{M}(\boldsymbol{B} - \boldsymbol{R})^t\mathscr{E}^t]_{x,z} - [\mathscr{E}^{(1)}(\boldsymbol{B} - \boldsymbol{R})\boldsymbol{M}(\boldsymbol{B} - \boldsymbol{R})^t\mathscr{E}^t]_{z,x}}. \tag{40}$$

For a linear-planar molecule such as NCNCS $\varepsilon(\rho)$ is then obtained by choosing $\varepsilon(\rho = 0) = 0$ so that the SRB z-axis aligns with the molecular axis at linearity, and then numerically integrating eqn (40) from $\rho = 0$ to ρ.

For any value of ρ, the elements of the matrix $\tilde{\boldsymbol{\mu}}$ and its determinant $\tilde{\mu}$ can be obtained from $\tilde{\boldsymbol{I}}$ by direct inversion [see eqn (19)]. The required derivatives can be obtained from the relationships,

$$\begin{aligned}
\tilde{\boldsymbol{\mu}}' &= -\tilde{\boldsymbol{\mu}}\tilde{\boldsymbol{I}}'\tilde{\boldsymbol{\mu}}, \\
\tilde{\boldsymbol{\mu}}'' &= -\tilde{\boldsymbol{\mu}}\tilde{\boldsymbol{I}}''\tilde{\boldsymbol{\mu}} - 2\tilde{\boldsymbol{\mu}}\tilde{\boldsymbol{I}}'\tilde{\boldsymbol{\mu}}\tilde{\boldsymbol{I}}'\tilde{\boldsymbol{\mu}}, \\
\tilde{\mu}' &= -\tilde{\mu}\mathrm{Trace}\,(\tilde{\boldsymbol{\mu}}\tilde{\boldsymbol{I}}'), \\
\tilde{\mu}'' &= +\tilde{\mu}[\mathrm{Trace}\,(\tilde{\boldsymbol{\mu}}\tilde{\boldsymbol{I}}')]^2 - \tilde{\mu}\mathrm{Trace}\,(\tilde{\boldsymbol{\mu}}\tilde{\boldsymbol{I}}'') - \tilde{\mu}\mathrm{Trace}\,(\tilde{\boldsymbol{\mu}}'\tilde{\boldsymbol{I}}').
\end{aligned} \tag{41}$$

Thus all elements of the SRB Hamiltonian can be determined in terms of the $\boldsymbol{A}$ matrix once the elements of $\tilde{\boldsymbol{I}}$ as given in eqn (35) and (36) are calculated, along with their first through second order derivatives with respect to ρ.

Because the ρ elements given in eqn (36) already involve the first derivative of the nuclear coordinates with respect to ρ, we need the third derivatives of the nuclear coordinates with respect to ρ. Using eqn (34), which gives the $\boldsymbol{A}$ matrix in terms of the axes-of-convenience matrix $\boldsymbol{B}$, the elements of $\tilde{\boldsymbol{I}}$ and their derivatives can be expressed entirely in terms of analytic expressions involving $\boldsymbol{B}$ and its derivatives. *These expressions are general in the sense that they do not depend on the molecule or on the form of the large amplitude motion.* Although straightforward, the calculation of these analytic expressions is tedious and the results are rather complicated. The important point is that all the elements needed for the construction of the SRB Hamiltonian can be written in terms of the array $\boldsymbol{B}$ and its derivatives [along the lines of eqn (39)]. The contribution of ref. 8 was to do exactly this, thereby allowing for easy generalization of the SRB technique to any single large amplitude motion of any molecule. That is, the main part of the Generalized SRB, or GSRB, program is entirely written in terms of general analytic expressions involving the arrays $\boldsymbol{M}$ and $\boldsymbol{B}$, $\boldsymbol{B}'$, $\boldsymbol{B}''$, and $\boldsymbol{B}'''$. The arrays $\boldsymbol{B}$, $\boldsymbol{B}'$, $\boldsymbol{B}''$, and $\boldsymbol{B}'''$

This journal is © the Owner Societies 2010

Phys. Chem. Chem. Phys., 2010, **12**, 8158–8189 | 8167

themselves are simply the ρ dependent coordinates (and their derivatives with respect to ρ) of the nuclei with respect to the axes of convenience. They are therefore easy to evaluate in terms of the molecular internuclear distances and bond angles (both as functions of ρ) and are the only part of the GSRB which is specific to a particular molecule. These arrays are calculated in a molecule-specific subroutine with the GSRB main program assembling the required elements of the SRB Hamiltonian from the analytic expressions involving these simple results.

One point to remember is that a fitting of the geometric parameters of the GSRB model refers to a fitting of the equilibrium position of the reference configuration. The parameters describing the potential energy function $V(\rho)$ can also be fitted, as can bond relaxation parameters and several *ad hoc* parameters that may be needed in particular cases.

2.3 Discussion of centrifugal distortion effects and the potential function used in the GSRB Hamiltonian

The main output of the GSRB program is a set of energy eigenvalues for the range of quantum numbers requested, along with the fitted parameters when a least-squares adjustment is requested. The model accounts for the bulk of the effects of the large-amplitude vibration. However, even states in which only the large-amplitude vibration is excited are affected by the small-amplitude modes. These effects are not directly included in the GSRB and, although generally small, those that depend strongly on J can grow to dominate the deviations between observed and calculated transition frequencies. This can make it difficult to perform a useful fitting of the GSRB to experimental data. This is because the GSRB model parameters become distorted when trying to account for effects not included in the model. These difficulties can be addressed by simply adding small correction terms to the GSRB Hamiltonian, thereby "cleaning" up the fittings. By this we mean that the bulk of the effect of the not-included factors can be subsumed by the "clean-up" parameters, allowing the GSRB to account more directly for the physics which it does describe. Indeed, twenty years ago it had already been recognized that the small amplitude vibrations can contribute as much as 10% of the splitting of the $K_a = 1$ (or $\ell = 1$) levels.[8] This contribution can be accounted for in an "effective" manner by introducing a parameter $\hat{q}$ and by adding and subtracting, as appropriate, the quantity $\frac{1}{2}\hat{q}J(J + 1)(v_b + 1)$ to the two $K_a = 1$ energy levels, respectively. The quantity $\hat{q}$, representing that part of the $K_a = 1$ splitting originating in the small amplitude vibrations, analogous to the physical ℓ-type doubling constant of a linear molecule, is then determined in the least-squares fitting. Calculations which incorporate this term in the Hamiltonian can be labeled as GSRB + q. In the least-squares fittings for NCNCS, however, the uncertainty in $\hat{q}$ was larger than the fitted value, *i.e.* the parameter was, within its error, zero, meaning that for NCNCS (as was the case in ref. 8) the large-amplitude motion part of the GSRB model accounted, within the limits of the least-squares fitting, for the difference in B_{eff} values between the $K_a = 1$ asymmetry pairs. We therefore fixed $\hat{q}$ to zero in the final fitting.

Large-amplitude motion leads to effects which have the same J-dependence as centrifugal distortion. However, the GSRB does not account for centrifugal distortion itself. To account for that part of the apparent centrifugal distortion not directly due to the large-amplitude motion we can add additional terms to $\hat{H}_{SRB}$ of eqn (23). In this work we add one such term to do this,

$$\hat{H}_{CD} = -D(\rho)\hat{J}^4 \tag{42}$$

where

$$D(\rho) = D_0 + D_2\rho^2 + D_4\rho^4. \tag{43}$$

This term is simply added to $\hat{H}_{SRB}$ and included in the determination of the matrix representation and subsequent matrix diagonalization as performed in Step 2 in Sub-section 2.2, above. The three constants D_0, D_2, and D_4 are then determined in the least-squares fitting to the experimental data. Calculations which incorporate such terms can be labeled as GSRB + CD. As we shall see below, the contributions due to $\hat{H}_{CD}$ vary weakly and smoothly with K_a, and v_b unlike the large-amplitude contributions accounted for by the GSRB itself. That is, the strong variation due to monodromy is described by the GSRB, while the CD terms simply clean up the fitting.

The bulk of the experimental data reported here is for high J levels which are beyond the reasonable range of calculation due to the GSRB's neglect of centrifugal distortion (other than the optional inclusion of the leading diagonal centrifugal distortion terms in a GSRB + CD calculation). Previously this type of situation was handled by using linear-molecule Σ-state parameters fitted to high J data to calculate "synthetic" transitions at low J for use in fitting in the GSRB program. In the current work we started in that way but eventually introduced a new option into the GSRB program. With this option the program first calculates ro-vibrational energies up to $J = 25$. In each vibrational level, v_b, and for each value of K_a and symmetry (e or f), these GSRB calculated energies are used to fit values of the constants of the simple linear molecule energy level formula,

$$E = E_0 + B_{eff}(v_b, K_a, ef)J(J + 1) - D_{eff}(v_b, K_a, ef)J^2(J + 1)^2$$
$$+ H_{eff}(v_b, K_a, ef)J^3(J + 1)^3. \tag{44}$$

(Note that for $K_a = 0$ there is only one sequence, while for all other values of K_a there are two sequences of levels, the "asymmetry pairs", labeled by their symmetry e or f[44] or by the conventional asymmetric rotor rotational J_{K_a,K_c}). Similarly, linear molecule Σ-state constants were extracted from the experimental data [although using a model including the next higher centrifugal distortion term, $L_{eff}J^4(J + 1)^4$]. Although a power series in $J(J + 1)$ cannot perfectly mimic asymmetry effects, the fact that both sets of effective constants are obtained in the same way allows limitations of the strategy to cancel out. The GSRB model parameters were then adjusted to fit the B_{eff} and D_{eff} constants calculated with the GSRB to those extracted from the experimental data.

The relative weight used for the D_{eff} and B_{eff} constants in the least-squares fittings was set by first performing a range of least-squares fittings in which the relative weight was varied.

As the relative weight of the D_{eff} constants was increased by many orders of magnitude the RMS error of the B_{eff} constants stayed constant while that of the D_{eff} constants steadily but slowly improved. A relative weight on the D_{eff} constants below 10^4 led to a large RMS error on the fitted values of the D_{eff} constants, while a relative weight of 10^{10} or more results in an increase in the RMS errors of the B_{eff} constants. In the range of reasonable relative weights of 10^4 to 10^9 the square of the ratio of the RMS errors of the B_{eff} constants to those of the D_{eff} constants remained a constant 1.6×10^8. This value was therefore taken as the model limited value to use as the relative weights of the D_{eff} values to the B_{eff} values in the least-squares fitting. Since this value corresponds roughly to the inverse of the ratio of the squares of the experimental statistical errors on the two sets of constants the B_{eff} and D_{eff} values therefore contribute almost equally to the fit.

The least-squares fitting of the GSRB model was accomplished with the adjustment of only a small number of parameters. The CS internuclear distance, r_{CS}, is expressed as a quadratic function of ρ

$$r_{CS}(\rho) = r_{CS}(\rho_e) + r_{CS}^2(\rho^2 - \rho_e{}^2). \qquad (45)$$

The CS equilibrium distance, $r_{CS}(\rho_e)$, and its semi-rigidity with respect to ρ, the constant r_{CS}^2, were adjusted in the least squares fitting. The other nuclear distances were held fixed at the equilibrium values given in Table 3. This choice of variables will be discussed in section 5. The NCN and NCS angles were expanded as linear functions of ρ, each taking the value 180° at linearity ($\rho = 0$), and the ab $initio$ values given in Table 3 at the equilibrium configuration, neither of which was adjusted in the least-squares fitting. The potential energy function used for the large-amplitude bending vibration was the modified quadratic well with Lorentzian hump introduced by Barrow, Dixon, and Duxbury.[45]

$$V(\rho) = \frac{H(1 + c\rho^2)f_{\alpha\alpha}(\rho^2 - \rho_e^2)^2}{f_{\alpha\alpha}\rho_e^4 + [8H(1 + c\rho^2) - f_{\alpha\alpha}\rho_e^2]\rho^2}, \qquad (46)$$

Table 3 Results of the Generalized Semi-Rigid Bender (GSRB + CD) analysis of NCNCS rotational transitions

Parameters	Ab initio[a]	GSRB + CD	GSRB, ref. 8
		Geometry	
$r_{N_1C_1}$/Å	1.161	= ab initio	1.164
$r_{C_1N_2}$/Å	1.314	= ab initio	1.343
$r_{N_2C_2}$/Å	1.210	= ab initio	1.218
r_{C_2S}/Å	1.551	1.55812 (18)	1.52945 (11)
$r_{C_2}^2$/Å rad^{-2}		0.08353 (31)	0.09689 (22)
$\angle$(NCN)$_{equ}$/°	176.5	= ab initio	172.0
$\angle$(NCS)$_{equ}$/°	174.6	= ab initio	173.8
		Potential energy function	
$\angle$(CNC)$_{equ}$/°	143	143.327 (17)	140.983 (11)
H/hc cm^{-1}	285	272.79 (33)	270.93 (25)
$f_{\alpha\alpha}$/aJ rad^{-2}	0.109	+0.08133 (17)	+0.07713 (10)
c		−0.04491 (51)	−0.04785 (65)
		Centrifugal distortion	
D_0/Hz		+43.1 (26)	
D_2/Hz rad^{-2}		−43.9 (89)	
D_4/Hz rad^{-4}		+91.1 (69)	

[a] Geometric parameters from last column of Table 1.

where H is the height of the potential barrier to linearity, ρ_e is the non-zero equilibrium value of ρ which is the compliment of the equilibrium CNC angle, $f_{\alpha\alpha}$ is the harmonic force constant at equilibrium, and c adjusts the anharmonicity around equilibrium. All four potential energy function parameters were adjusted in the non-linear least-squares fitting procedure, making a total of 6 GSRB adjusted parameters. In addition, for the final GSRB + CD fitting, three effective centrifugal distortion constants were fitted, D_0, D_2, and D_4. All final parameters, both adjusted and held fixed, are reported in Table 3. These will be discussed in more detail in section 5.1.

All GSRB calculations were done on a notebook computer. Eqn (29) was solved using a grid of 625 points on the interval $\rho = 0$ to 2.1 rad, while the matrix representation of the Hamiltonian described in Step 2, above, was done using a basis set of $v_b = 0$–12. This provides an adequate basis for calculations through $v_b = 7$.

A full least-squares cycle, including the numerical calculation of the derivatives with respect to the 9 parameters of the GSRB + CD model and a run with the new parameters, takes roughly 2 min on a 2.00 GHz Intel(R) Core(TM)2 Due CPU Lenovo T61 computer running Windows XP Service Pack 3 and Lahey/Fujitsu Fortran 95 Compiler.

3. Experimental details

Cyanogen iso-thiocyanate, NCNCS, was prepared by the pyrolytic isomerization reaction of sulfur dicyanide, $S(CN)_2$, following the method described by King and Kroto.[5] The precursor molecule $S(CN)_2$ was synthesized using a procedure analogous to that given by Long and Steele,[51] described in detail in a recent publication by Kisiel et $al.$[46] The purified $S(CN)_2$ in crystallized form was stored in a Schlenk tube[52] in dry ice. All NCNCS spectral measurements were carried out in a flow regime with the Schlenk tube directly attached to the inlet port of the vacuum pyrolysis system, which was connected to an inlet port of the absorption cell. In order to maintain sufficient $S(CN)_2$ vapor pressure for the isomerization reaction the Schlenk tube was kept at room temperature. The quartz pyrolysis tube was heated to $ca.$ 855 °C and the reaction zone, about 20 cm in length, was filled with crushed quartz chips which were secured on both sides with quartz wool. The hot reaction gases passed through a cold trap at −45 °C in order to remove the un-reacted $S(CN)_2$ before the gaseous reaction products entered the 6 m long aluminium absorption cell. During the measurements a total pressure of 5 mTorr was maintained for the flow. From the spectra, which have a signal to noise of about 2000 : 1 for the strong NCNCS lines, only the trace components HCN and HNCS were identified. These are secondary reaction products of NCNCS and $S(CN)_2$. No $S(CN)_2$ lines could be identified.

The spectra of NCNCS were recorded using the Fast Scan Sub-millimetre Spectroscopic Technique (FASSST), as originally described in ref. 55, with further modifications and improvements covered in ref. 56 and 57. Relative frequency calibration of spectra recorded during the fast sweep of the source frequency was achieved by means of simultaneously recorded fringes obtained by directing some of the microwave radiation to a 9.5 MHz free spectral range (15 m length) ring

This journal is © the Owner Societies 2010

Phys. Chem. Chem. Phys., 2010, **12**, 8158–8189 | 8169

cavity. Absolute frequency calibration was made on the basis of line positions of the reference gas sulfur dioxide (SO_2), which was placed in a 0.5 m cell following the main absorption cell. The FASSST spectra were recorded in five different frequency segments, using three different millimetre-wave Backward Wave Oscillator (BWO) sources, as indicated in panel **a** of Fig. 6. At room temperature and at 165 °C, 200 individual scans in positive and negative frequency direction were recorded. Each scan was calibrated separately and, in the process, a small proportion of the scans was rejected by the calibration software. The individual scans were then co-added and the spectral segments were properly stitched together in amplitude and frequency to yield separate up- and down-scanned spectra covering the range from 110 to 375 GHz. Spectra obtained in this way are subject to small-scale fluctuations in frequency calibration caused by reproducible fluctuating scan rates of the BWO tubes. However, since the fluctuations in up and down scans are in opposed frequency directions,[56] considerable improvement in the accuracy of measured line positions was obtained by averaging peak positions measured in up- and down scans. In ref. 46 it was established that an even more convenient way to arrive at the final spectrum was to simply add the up- and down-scanned spectra.

At the time of the NCNCS measurements we recorded all 200 up-scans followed by 200 down-scans. Due to variations in sample pressure and thermal drifts in the system, there was a slight variance in spectral line intensity patterns between up- and down-scans. In order to perform the co-addition of the up- and down-scan spectra we normalized the line intensities in one direction to match the other data set before co-adding the two sets of spectra. The resulting line positions were comparable in accuracy to the matching entries in the peak-finder tables resulting from averaged line peak values.

Shortly after these measurements we switched to recording the down-scan immediately after the up-scan, thus eliminating the need for the above mentioned intensity normalization procedure. The accuracy of frequency measurements obtainable with the FASSST spectrometer following this procedure was discussed in ref. 46. That work furnished convincing arguments that for un-blended lines the line position accuracy is close to ±50 kHz, which appears to be the case also for the present NCNCS measurements.

Additionally, after these measurements the spectrometer calibration software was modified to account for the effects of the changing atmospheric index of refraction in the vicinity of the strongly absorbing water lines as described in ref. 57. At the time of the NCNCS measurements, no record of the laboratory air humidity and temperature was made. However, one of the features of the new calibration software is the ability to fit for those parameters. Several individual scans were calibrated in this mode to obtain a faithful measure of the humidity at the time of the measurements with the assumption that room temperature was 25 °C. The rest of the scans were re-calibrated using the adjusted correction parameters. The consistency of the data, especially over 300 GHz, was noticeably improved.

While frequencies can be measured very precisely, the accurate determination of the absorption coefficients still
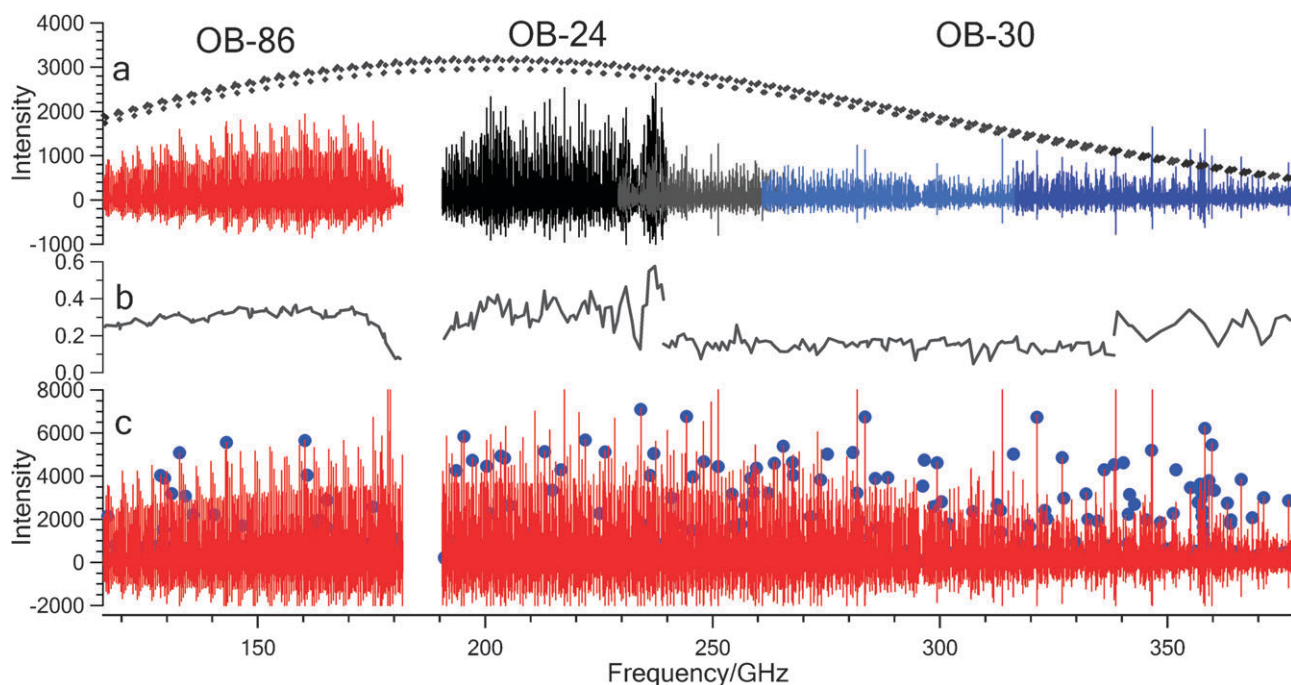
Fig. 6 The re-scaling of the intensities for the NCNCS spectrum: Panel **a** shows in the top set of black markers the predicted peak intensities for the a-type $K_a = 0$, 1 and 2 rotational transitions for the ground vibrational state, $v_b = 0$, using the Watson Hamiltonian analysis for an asymmetric rotor. The lower trace in panel **a** constitutes the raw (not yet intensity normalized) spectrum between 115 GHz and 375 GHz. The five ranges covered by the three BWOs OB-86, OB-24 and OB-30 are indicated in five different colors. Panel **b** depicts the normalization function obtained by ratioing the predicted and experimental peak intensities following the procedure outlined in ref. 46. Panel **c** shows the final, normalized, FASSST spectrum of NCNCS. This spectrum contains 115 000 line positions. The blue dots indicate SO_2 calibration lines.[47–50]

remains a notoriously difficult challenge. As Kisiel *et al.*[46] have pointed out, the intensity problem is normally disregarded in narrow-band spectra, but becomes of increasing relevance in the analysis of broad-band FASSST laboratory spectra. The assignment of such a high-information FASSST spectrum, which for NCNCS contains more than 100 000 lines distributed over a spectral region of several hundred Gigahertz, can only be dealt with using interactive graphical assignment techniques. In order to enhance the recognition of characteristic patterns, or to use the intensity information directly, it thus becomes mandatory to have reliable intensity information.

For this reason the experimental intensities of the room-temperature FASSST spectrum of NCNCS were re-calibrated on the basis of 400 un-blended, ground state, a-type $K_a = 0, 1$ and 2 rotational transitions in the spectral region from 110 GHz to 360 GHz. These transitions were the only ones that could be assigned and reasonably fitted to a Watson type Hamiltonian (A-reduction) in the SPFIT program of Pickett;[3] adding $K_a = 3$ lines increased the standard deviation dramatically. For the excited vibrational states, the fits are even worse. The constants thus determined are listed in Table 4. Only a slightly better fit might be obtained using the S-reduction. The constants obtained are in any case of little physical significance, but adequate for the intensity calculation.

The RMS deviation of the fit, even for this limited data set, was 1.08 MHz which is well outside the experimental accuracy of ± 50 kHz. King *et al.*[7] recognized that the higher K_a lines do not cluster close to the $K_a = 0$ transition, as is expected for near-prolate semirigid molecules, a fact which is clearly displayed in Fig. 2. Therefore the anomalously large centrifugal distortion constants of Table 4, necessary to reproduce just the $K_a = 2$ lines have no physical significance. However, this *effective* parameter set allowed us to calculate appropriate intensities for the a-type $K_a = 0, 1$ and 2 rotational transitions which could then be used in the intensity re-scaling procedure.

Following the procedure outlined in ref. 46, the experimental and calculated intensities for these NCNCS lines were used to derive the intensity correction array using linear interpolation between the 400 fairly sparse predicted transitions. The re-scaled FASSST spectrum assumed an intensity envelope with a Boltzmann hump as expected. The individual steps are displayed in Fig. 6. The top panel **a** of Fig. 6 shows the raw spectrum between 115 GHz and 375 GHz. To obtain predicted peak intensities for the ground state low-K_a lines we simulated the Doppler-limited spectrum using Gaussian line profiles. This procedure reproduces the linear dependence of the Doppler line width on frequency. A constant value for the a-type dipole moment component was assumed at this early stage of the data processing, taken from an early result of the *ab initio* calculations, $\mu_a = 3.1626$ D, which lies in the middle of the range spanned by the final *ab initio* results in Table 2. Since the sample was very pure, and the vapor pressure was measured, this procedure provided absolute intensities, under the assumption of a constant dipole moment value for all series. The peak intensities of the simulated spectrum are plotted as markers in the top trace in panel **a** of Fig. 6. Panel **b** shows the normalization function obtained by ratioing the predicted and experimental peak intensities. Panel **c** shows the final, now intensity-normalized, spectrum with lines belonging to the SO_2 calibration gas marked with blue dots.

4. Data reduction and assignment procedures

The assignment of the FASSST spectrum was carried out using the CAAARS program[4,58] running on the platform IgorPro. This program package provides a Loomis–Wood-type display[53,54] of the original spectrum as shown in Fig. 7. Under actual assignment conditions the screen display is overlaid with markers for line centers. Predicted line positions for the series to be identified are marked prominently in red and green colors as is shown in Fig. 7 after successfully assigning series for $K_a = 2$ for the vibrational bending state $v_b = 4$. Convenient interactive functions allow rapid consecutive assignment of lines in a series. This act of "assignment" enters the line center in a table of assigned lines together with the quantum numbers of the predicted line, a specified default estimated error and the line intensity, all sorted according to branch label definitions. At any time, with a single click CAAARS stores this list into an input file for the Jet Propulsion Laboratory (JPL) program package SPFIT/SPCAT,[3] and the fitting program runs immediately in a few seconds. Another click loads the new predictions, and the assignment process can proceed. In the best case for easily identifiable transitions, up to 600 lines could be assigned in a day. So far, 9204 rotational lines have been assigned.

The rotational frequencies clearly fall into series in J'' (see Fig. 7) that can be assigned to a given vibrational state v_b and K_a rotational level, in the notation of an asymmetric rotor, with asymmetry splitting for low K_a. As already noted, an asymmetric top Hamiltonian and a linear model were equally useless. This forced us to devise a labeling procedure in the CAAARS program that could be used with the SPFIT and SPCAT routines to determine effective parameters for such a molecule with large amplitude vibrational motion.

We resorted to simply identifying each series by the vibrational quantum number it would have as a bent molecule, v_b, and its angular momentum about the figure axis a in Fig. 1,

Table 4 Derived spectroscopic constants for NCNCS from 400 ground state rotational transitions for $K_a = 0, 1,$ and 2 using Watson A-reduction

Spectroscopic constants	Ground state $v_b = 0$
A/MHz	97007.710(267)
B/MHz	1628.0244124(63)
C/MHz	1599.3908401(54)
Δ_J/kHz	−0.418564507(165)
Δ_{JK}/MHz	0.98752349(121)
Δ_K/MHz	2986.603(43)
δ_J/kHz	−0.062265055(209)
δ_K/kHz	40.05111(206)
Φ_J/mHz	0.9754448(100)
Φ_{JK}/Hz	6.149066(67)
Φ_K/kHz	−0.06070827(305)
Φ_{KJ}/kHz	7.256510(293)
ϕ_J/mHz	0.2512794(127)
L_J/nHz	−3.63347(64)
L_{JJK}/mHz	0.1523219(42)
L_{JK}/Hz	−0.4254926(165)
L_{KKJ}/kHz	−6.839427(58)
σ_{fit}/MHz	1.081
N_{lines}	400

This journal is © the Owner Societies 2010

Phys. Chem. Chem. Phys., 2010, **12**, 8158–8189 | 8171

Fig. 7 In this Loomis–Wood[53,54] diagram the CAAARS[4] assignment window displays 20 successive excerpts of the millimetre wave spectrum of NCNCS for the rotational transitions from $J'' = 35$ to 54. The positions of successive lines of a candidate series are aligned above one another with an offset in frequency by an amount roughly equal to the spacing of $2B_v$. Other series with similar values of B_v can clearly be recognized. The two series assigned for the $K_a = 2$ rotational transitions, after considering six other candidate series in this diagram, are marked in green and red for the state $v_b = 4$, and flagged below the frequency axis.

given by quantum number K_a, which is identical to the ℓ quantum number for a linear molecule. Since the e and f symmetry of the components[44] in the cases where the K_a degeneracy is lifted was not obvious, as we shall see, they were labeled as "U" or "L" for upper or lower component, according to the frequency of the observed transitions. The raw data for the series in J'' are thus labeled by v_b, K_a and U or L. For comparison with the GSRB calculations, we will later include e and f, and also the asymmetric rotor notation where relevant. v_b, K_a and "U" or "L" were encoded in a "hash" of two digits, allowing all series for two values of v_b to be included in one data set. [Hash for $(v_b, K_a, U/L)$: $n = (v_b + 1) \times 50 + K_a + (U/L) \times 25$, where $U/L = 0$ for lower, 1 for upper.] The assignments were assembled in the assignment process in this manner into 4 data files.

Each series of rotational transitions was fit independently with a power series in $J(J + 1)$, giving spectroscopic constants as for a diatomic molecule: B_{eff}, $-D_{eff}$, H_{eff}, and L_{eff}. These four constants were necessary for each series. They are listed for NCNCS in Tables 5–7. The rotational transition frequencies are listed with the obs-calc values resulting from the polynomial fits in the supplementary data in one Table for the states $v_b = 0$ to 6. For some series, higher order terms were called for, but these cases represent either cases of identifiable accidental resonances, unidentifiable resonances, or low K_a levels with asymmetry effects (or linear molecule vibrational effects) for which it is known that a power series in $J(J + 1)$ cannot reproduce the series. In these cases, after following a

series for purposes of assignment as completely as possible with a higher order polynomial, or a local polynomial, the polynomial was truncated to four terms, and the high-J lines or those showing an obvious resonance were given low weights (artificially high estimated experimental errors) but are included in the list of assigned lines.

The v_b and K_a assignments were initially made following the assignments of King et al.,[7] for v_b up to 3 and K_a up to 8. For higher v_b and K_a, we relied on the predicted B_{eff} values obtained using the GSRB model. Intensity was also considered. Later, just as we began to find more than one legitimate candidate for some K_a levels in the $v_b = 4$ and 5 states (see Fig. 7), and predictions from preliminary fittings became available, we realized that the reproduction of the observed D_{eff} values by the GSRB predictions was more reliable and informative than we had dared to hope, and that these values provided a second and independent piece of information for making assignments. This was especially true for low K_a levels. The low K_a assignments for $v_b = 4$, 5 and 6 were *only* possible using GSRB predictions of both the B_{eff} and D_{eff} values.

Fig. 8 shows reduced Fortrat diagrams [traditionally, plotted as frequency *vs.* J'', but more revealing for a-type rotational transitions as frequency $/2(J'' + 1)$ *vs.* J''] of the measured and assigned rotational transitions. The plots show the full range of the measured data, including the earlier data of King et al.[7] which fall below the K_a labels for $v_b = 0$ to 3. Gaps in the curves below $J'' = 35$ and around $J'' = 50$ are due to the limits of the BWO frequency ranges. Smaller gaps

8172 | *Phys. Chem. Chem. Phys.*, 2010, **12**, 8158–8189

This journal is © the Owner Societies 2010

Table 5 Experimentally determined effective rotational and centrifugal distortion constants for NCNCS in the vibrational bending states $v_b = 0$, 1 and 2 for different values of K_a. Indicated uncertainties are the standard errors from power series fits.

v_b	K_a	L/U	$B_{eff}(v_b, K_a)$/MHz	$D_{eff}(v_b, K_a)$/Hz	$H_{eff}(v_b, K_a)$/mHz	$L_{eff}(v_b, K_a)$/nHz
0	0		1613.72024(59)	671.187(142)	8.5769(133)	−89.18(42)
0	1	L	1607.50471(61)	408.815(144)	2.5474(134)	−257.1(42)
0	1	U	1621.89691(61)	532.201(147)	2.1918(139)	−5.37(45)
0	2	L	1617.32946(60)	435.909(146)	1.9831(139)	−11.85(45)
0	2	U	1617.31796(67)	181.278(179)	−5.8500(188)	73.43(67)
0	3	L	1621.04643(69)	350.931(161)	−0.2504(149)	15.78(47)
0	3	U	1621.04249(69)	349.102(161)	0.5669(149)	−5.74(47)
0	4	L	1625.42595(74)	352.677(180)	0.4419(175)	3.09(57)
0	4	U	1625.42895(64)	353.634(158)	0.5346(156)	1.19(52)
0	5	L	1630.22071(62)	352.901(153)	0.8176(148)	−7.36(48)
0	5	U	1630.21656(62)	351.346(154)	0.6156(150)	1.07(49)
0	6		1635.25005(62)	349.620(151)	0.7065(146)	−0.46(48)
0	7		1640.42933(63)	348.582(156)	0.7356(153)	−0.94(51)
0	8		1645.69773(67)	349.363(174)	0.8016(167)	−2.36(54)
0	9		1651.01563(65)	350.895(165)	0.8354(164)	−3.56(55)
0	10		1656.35415(71)	352.442(178)	0.7655(175)	−1.29(58)
0	11		1661.70774(72)	355.887(185)	0.7783(183)	−1.66(61)
0	12		1667.06143(77)	360.035(195)	0.7726(194)	−1.37(65)
0	13		1672.41158(73)	365.340(187)	0.7934(188)	−1.90(64)
0	14		1677.75164(75)	371.241(193)	0.7941(196)	−1.89(67)
0	15		1683.08216(75)	378.368(195)	0.8248(198)	−2.60(68)
0	16		1688.39843(76)	385.922(198)	0.8132(202)	−1.95(70)
0	17		1693.70179(77)	394.490(199)	0.8125(202)	−1.77(69)
0	18		1698.99306(79)	404.242(206)	0.8241(211)	−1.91(74)
0	19		1704.27217(79)	415.301(207)	0.8478(213)	−2.30(74)
0	20		1709.53908(89)	427.666(229)	0.8737(233)	−2.97(81)
1	0		1610.21182(63)	634.487(154)	6.5465(148)	−70.72(48)
1	1	L	1605.63767(68)	401.031(176)	2.2471(181)	−15.58(63)
1	1	U	1620.03168(60)	531.257(146)	2.5191(139)	−7.01(45)
1	2	L	1617.74694(61)	415.543(148)	2.1131(141)	−11.32(45)
1	2	U	1617.74290(64)	250.143(152)	−4.1421(143)	56.85(46)
1	3	L	1623.38262(78)	349.795(177)	0.1524(163)	8.35(52)
1	3	U	1623.37718(62)	347.954(152)	0.4953(147)	0.92(48)
1	4	L	1629.21893(83)	348.463(268)	0.7900(340)	−10.51(150)
1	4	U	1629.21723(63)	347.407(155)	0.5830(151)	1.92(49)
1	5		1635.08277(69)	345.058(180)	0.6548(170)	0.43(54)
1	6	L	1640.92632(81)	346.165(259)	0.9400(330)	−13.72(148)
1	6	U	1640.92485(85)	345.541(285)	0.8470(380)	−9.27(171)
1	7		1646.71768(63)	345.747(158)	0.7455(154)	−1.30(51)
1	8		1652.46031(65)	347.764(165)	0.7528(164)	−1.45(55)
1	9		1658.15155(72)	350.654(180)	0.7467(177)	−1.23(59)
1	10		1663.79614(68)	354.687(172)	0.7604(170)	−1.58(57)
1	11		1669.39548(74)	359.391(188)	0.7623(187)	−1.55(63)
1	12		1674.95424(75)	365.011(190)	0.7790(189)	−1.92(64)
1	13		1680.47404(76)	371.148(200)	0.7816(204)	−1.91(70)
1	14		1685.95986(85)	378.046(230)	0.7796(232)	−1.57(79)
1	15		1691.41422(81)	385.967(208)	0.8162(209)	−2.67(71)
2	0		1602.53497(84)	605.362(270)	5.8500(340)	−21.73(148)
2	1	L	1604.05538(62)	351.096(145)	2.5908(135)	−12.18(42)
2	1	U	1618.48566(62)	472.541(150)	3.4777(143)	−13.26(46)
2	2	L	1619.73001(61)	359.287(148)	2.3063(140)	−12.120(450)
2	2	U	1619.72799(61)	309.000(148)	−3.2178(141)	45.270(450)
2	3	L	1627.37668(104)	337.310(320)	0.1070(400)	3.82(178)
2	3	U	1627.37529(105)	336.479(312)	0.4500(390)	16.68(168)
2	4	L	1634.45966(87)	338.184(232)	0.6579(220)	−3.84(70)
2	4	U	1634.45918(80)	338.101(250)	0.6634(307)	−4.66(128)
2	5	L	1641.15771(63)	339.196(159)	0.6987(157)	−2.43(52)
2	5	U	1641.15594(63)	338.563(159)	0.6206(157)	0.65(52)
2	6		1647.58752(63)	341.602(158)	0.7126(156)	−1.93(52)
2	7		1653.81686(65)	344.675(165)	0.7037(164)	−1.35(55)

scattered through the spectrum indicate local resonances where the most perturbed lines could not be found. These gaps became slowly more frequent, until starting at $v_b = 5$, they become very numerous, and many series cannot be recovered at higher J''. This is attributed to a sudden increase in the density of vibrational states, due to the lowest excited levels of the other bending vibrations. The S/N is not yet a problem at this level of excitation, though increasing number of candidates for assignment and resonances are.

The Fortrat diagrams reveal much more, however. For each series, the intersection of the curve described by each series with the axis at $J'' = 0$ defines B_{eff}. Furthermore, the

This journal is © the Owner Societies 2010

Phys. Chem. Chem. Phys., 2010, **12**, 8158–8189 | 8173

Table 6 Experimentally determined effective rotational and centrifugal distortion constants for NCNCS in the vibrational bending states $v_b = 2$, 3, 4 and 5 for different values of K_a. Indicated uncertainties are the standard errors from power series fits.

v_b	K_a	L/U	$B_{eff}(v_b, K_a)$/MHz	$D_{eff}(v_b, K_a)$/Hz	$H_{eff}(v_b, K_a)$/mHz	$L_{eff}(v_b, K_a)$/nHz
2	8		1659.89466(66)	348.754(167)	0.7103(166)	−1.33(56)
2	9		1665.85194(70)	353.642(178)	0.7233(180)	−1.46(61)
2	10		1671.70974(74)	359.109(192)	0.7382(193)	−1.77(66)
2	11		1677.48420(75)	365.013(192)	0.7409(193)	−1.75(65)
2	12		1683.18993(76)	371.740(197)	0.7632(201)	−2.22(69)
2	13		1688.83364(79)	378.664(207)	0.7507(212)	−1.53(73)
2	14		1694.42692(81)	386.814(205)	0.8111(206)	−3.47(70)
2	15		1699.97198(90)	394.935(235)	0.8047(242)	−3.17(85)
3	0		1597.58748(83)	279.737(254)	8.5261(309)	−72.89(128)
3	1	L	1606.49839(71)	228.413(187)	2.6299(177)	−6.62(55)
3	1	U	1621.68872(84)	315.540(263)	3.293(33)	−19.43(139)
3	2	L	1624.83974(82)	392.046(261)	−3.998(33)	12.276(141)
3	2	U	1624.83595(66)	273.366(163)	2.2068(160)	−14.71(53)
3	3	L	1633.55499(64)	329.536(156)	−0.6768(150)	−17.88(49)
3	3	U	1633.55956(65)	331.158(157)	1.0896(150)	12.89(49)
3	4	L	1641.28462(64)	334.307(161)	0.5732(159)	−16.67(53)
3	4	U	1641.28173(64)	333.365(167)	0.3994(167)	10.07(56)
3	5	L	1648.42057(65)	338.307(162)	0.6204(160)	−5.96(54)
3	5	U	1648.42095(65)	338.148(161)	0.5441(158)	0.45(52)
3	6		1655.17173(67)	342.955(173)	0.6108(175)	−1.84(60)
3	7		1661.65091(69)	348.471(182)	0.6593(183)	−2.37(62)
3	8		1667.92654(76)	354.535(194)	0.7243(195)	−4.08(66)
3	9		1674.04251(75)	360.328(190)	0.7013(190)	−2.50(64)
3	10		1680.03174(76)	366.775(202)	0.7194(208)	−2.78(72)
3	11		1685.91848(112)	373.43(34)	0.696(35)	−1.52(120)
3	12		1691.71928(83)	381.282(218)	0.7716(227)	−4.16(80)
4	0		1609.87312(130)	−64.670(390)	5.1240(470)	−137.36(196)
4	1	L	1614.44767(72)	114.748(171)	2.8687(159)	6.54(50)
4	1	U	1631.41814(71)	175.623(172)	1.5524(164)	−29.80(53)
4	2	L	1633.04912(215)	574.030(900)	−5.415(153)	551.4(89)
4	2	U	1633.04981(78)	186.969(193)	2.0008(189)	−21.96(63)
4	3	L	1641.65715(102)	338.379(302)	−4.5190(330)	30.52(115)
4	3	U	1641.68550(73)	351.005(182)	3.1620(176)	−2.18(58)
4	4	L	1649.45413(82)	346.646(196)	0.5492(188)	−61.51(62)
4	4	U	1649.44764(82)	344.301(193)	0.1140(184)	36.79(60)
4	5	L	1656.67406(83)	348.325(219)	0.5491(223)	−18.17(75)
4	5	U	1656.67139(84)	346.959(224)	0.2319(228)	9.29(77)
4	6	L	1663.52096(80)	353.165(210)	0.5615(215)	−6.95(73)
4	6	U	1663.51931(80)	352.389(210)	0.4275(215)	0.60(74)
4	7		1670.09128(91)	359.401(264)	0.6602(289)	−6.65(106)
4	8		1676.44750(79)	365.087(205)	0.6403(209)	−4.28(72)
4	9		1682.63919(86)	372.431(249)	0.7474(263)	−6.74(91)
4	10		1688.69304(77)	378.588(202)	0.6633(208)	−3.13(72)
4	11		1694.63345(95)	385.646(238)	0.6531(237)	−3.48(81)
4	12		1700.48590(85)	395.737(221)	0.9249(227)	−17.73(80)
5	0		1625.67774(163)	−263.00(60)	5.333(88)	−479.3(45)
5	1	L	1624.80697(116)	28.18(37)	5.762(46)	−4.89(196)
5	1	U	1644.03739(96)	81.743(271)	−1.0097(301)	−13.53(114)
5	2	L	1643.1014(38)	949.05(181)	4.90(35)	1327.6(244)
5	2	U	1643.03901(80)	102.243(210)	2.0390(216)	−47.99(75)
5	3	L	1651.0329(32)	387.34(151)	−1.1340(279)	110.1(179)
5	3	U	1651.06566(80)	405.321(200)	8.5765(198)	−90.36(66)
5	4	L	1658.5505(83)	376.7(48)	0.60(107)	−261.(82)
5	4	U	1658.5501(53)	377.69(303)	0.71(71)	−13.(58)
5	5	L	1665.66695(84)	378.198(229)	1.2907(237)	−84.20(82)
5	5	U	1665.64505(87)	369.043(251)	−0.3312(274)	37.92(101)
5	6	L	1672.4499(45)	375.16(145)	0.662(189)	−25.4(85)
5	6	U	1672.4346(41)	369.56(137)	−0.189(183)	20.7(83)

dominant curvature defines D_{eff}. Although our first calculation with the GSRB alerted us to the fact that the vibrational dependence of B_{eff} for $K_a = 0$ would reverse at $v_b = 4$, we were not prepared for the equally dramatic changes in the value of D_{eff} for $K_a = 0$, 1, and 2, which emerged as the data were assigned. The monodromy effects on the curvature totally overwhelm the centrifugal distortion due to small-amplitude vibrations. On the other hand for higher K_a, the linear

dependence of B_{eff} on K_a, and the nearly constant D_{eff}, even for the $v_b = 0$ state, are remarkable, as they show that the molecule is behaving in those states as a very linear molecule; for an asymmetric rotor, the K_a-dependence of B_{eff} would be much smaller, and be proportional to roughly K_a^2, corresponding to a term with D_{JK}. With hindsight, all of these properties of the Fortrat diagrams make physical sense, but no one had considered these aspects of the spectra of quasi-linear or,

Table 7 Experimentally determined effective rotational and centrifugal distortion constants for NCNCS in the vibrational bending states $v_b = 5$ and 6 for different values of K_a. Indicated uncertainties are the standard errors from power series fits.

v_b	K_a	L/U	$B_{eff}(v_b, K_a)$/MHz	$D_{eff}(v_b, K_a)$/Hz	$H_{eff}(v_b, K_a)$/mHz	$L_{eff}(v_b, K_a)$/nHz
5	7	L	1678.99482(90)	377.664(226)	0.583.9(228)	12.06(78)
5	7	U	1678.98981(87)	375.915(221)	0.349.6(221)	1.50(75)
5	8		1685.36469(96)	388.202(308)	1.202.(33)	30.38(111)
5	9		1691.53967(301)	384.15(148)	−2.76.(293)	−46.9(203)
5	10		1697.44384(83)	388.763(221)	0.744.3(228)	3.18(80)
5	11		1703.10715(129)	398.29(46)	0.999.(63)	0.02191(297)
5	12		1709.53931(89)	427.730(231)	0.879.8(236)	3.16(82)
6	0		1639.0587(43)	−653.39(229)	−1.18(50)	−1464.0(380)
6	1	L	1635.40962(194)	−73.20(72)	15.206(102)	−246.0(51)
6	1	U	1656.97613(95)	−30.720(251)	−6.2951(269)	69.83(98)
6	2	L	1653.7616(58)	1540.2(33)	44.30(80)	1975.0(670)
6	2	U	1653.62908(82)	−15.459(207)	0.8833(205)	−71.30(69)
6	3	L	1661.0253(33)	443.46(164)	−33.41(33)	1107.0(233)
6	3	U	1661.1105(33)	498.57(146)	20.301(267)	−389.4(172)
6	4	L	1668.19949(140)	421.96(51)	−1.821(73)	−352.8(35)
6	4	U	1668.23402(117)	438.91(38)	1.141(48)	208.68(211)
6	5	L	1675.052(38)	391.3(172)	−3.0(33)	63.0(2380)
6	5	U	1674.959(170)	364.0(710)	−6.6(131)	310.(900)
6	6		1681.7701(81)	407.4(52)	1.06(143)	−136.(139)
6	7		1688.2575(236)	428.4(184)	9.5(62)	−1370.(750)
6	8		1694.53254(275)	408.66(129)	0.692(241)	−51.7(156)
6	9		1700.6884(236)	427.2(184)	7.5(62)	−1280.(750)
6	10		1707.60871(88)	413.722(238)	0.8355(253)	−2.88(92)
6	11		1712.96200(82)	425.374(223)	0.8837(236)	−4.25(84)
6	12		1718.29093(86)	437.273(230)	0.8462(242)	−2.84(87)

perhaps just as relevant, barely-bent molecules. Most of the remaining Figures in this paper are reformulations of information contained in this plot.

5. Analysis of the NCNCS data

5.1 GSRB analysis

In earlier applications the GSRB model was fitted to the observed transition frequencies, generally for $J < 10$. In the absence of compensation for centrifugal distortion due to small-amplitude vibration, such an approach is appropriate for such low values of J. In the present case, other than a narrow range of microwave lines involving $J = 8$ to 11 (and only for the lowest bending vibrational levels), the experimental data obtained are from MMW and Sub-MMW data starting at $J'' = 33$ and extending very much higher. Even with the GSRB extended to $J = 25$, there is no overlap with the new observations. We therefore followed Bunker et al.[59] by fitting to the experimentally determined B_{eff} values, rather than directly to the transition frequencies. In this way, effects that are not rigorously modeled in the GSRB Hamiltonian, such as the centrifugal distortion effects, do not bias the GSRB fitting. New in the current work is the inclusion of the experimentally determined D_{eff} values in the fitting as discussed in section 2.3. That is, we performed a non-linear least-squares adjustment of the parameters of the GSRB + CD Hamiltonian to fit to the experimentally determined B_{eff} and D_{eff} values given in Table 5 through Table 7.

Fig. 9a presents the observed and GSRB + CD-calculated B_{eff} values for each bending vibrational level as a function of K_a. For completeness in the Figures, values for e-symmetry levels are plotted at $K_a \geq 0$, while those for f-symmetry are plotted at $K_a < 0$. As in the previous two papers, the asymmetry splitting is averaged, and the plot corresponds to the classical case with $+ K_a$ and $- K_a$. Here can be seen the prototypical behaviour due to monodromy of NCNCS as already shown for $v_b = 0$ to 5 in ref. 1 and discussed in ref. 2. Indeed, it is this striking variation of the effective rotational constants with v_b and K_a that allows the GSRB + CD to accurately determine the potential energy function from rotational data alone.

Fig. 9b shows in analogous form the GSRB + CD-calculated term values as a function of K_a for relevant bending vibrational levels. Also shown is a selection of unit cells representing an augmentation of each of K_a and v_b by one. As is now well known (for example see Fig. 9 of ref. 2 and the associated text) the definitive signature of quantum monodromy can be seen by constructing such unit cells for a sequence of points enclosing the monodromy point (here $v_b \cong 3$, $K_a = 0$). At the completion of one loop around the monodromy point, the unit cell does not return to its original configuration. Instead quantum monodromy has induced a robust dislocation in the energy level grid.

The observed and GSRB + CD-calculated D_{eff} values are shown in the left hand panels of Fig. 10 and 11, again with values for e-symmetry plotted at $K_a \geq 0$ and those for f-symmetry plotted at $K_a < 0$. In these Figures, the asymmetry effects have not been averaged out. The variation of the observed values is well reproduced in the GSRB + CD values. This agreement is particularly impressive for $v_b = 6$, for which no experimental data were included in the least-squares fitting. It is important to note that the strongly K_a-dependent variations and the major portion of the slowly varying contribution are fully accounted for by the basic GSRB model. The additional terms that were fitted, D_0, D_2, and D_4, give rise to nearly constant, smoothly varying contributions to the calculated D_{eff} values in the range of 40–50 Hz, indicated by the blue diamonds in each of these Figures. While these

This journal is © the Owner Societies 2010

Phys. Chem. Chem. Phys., 2010, **12**, 8158–8189 | 8175
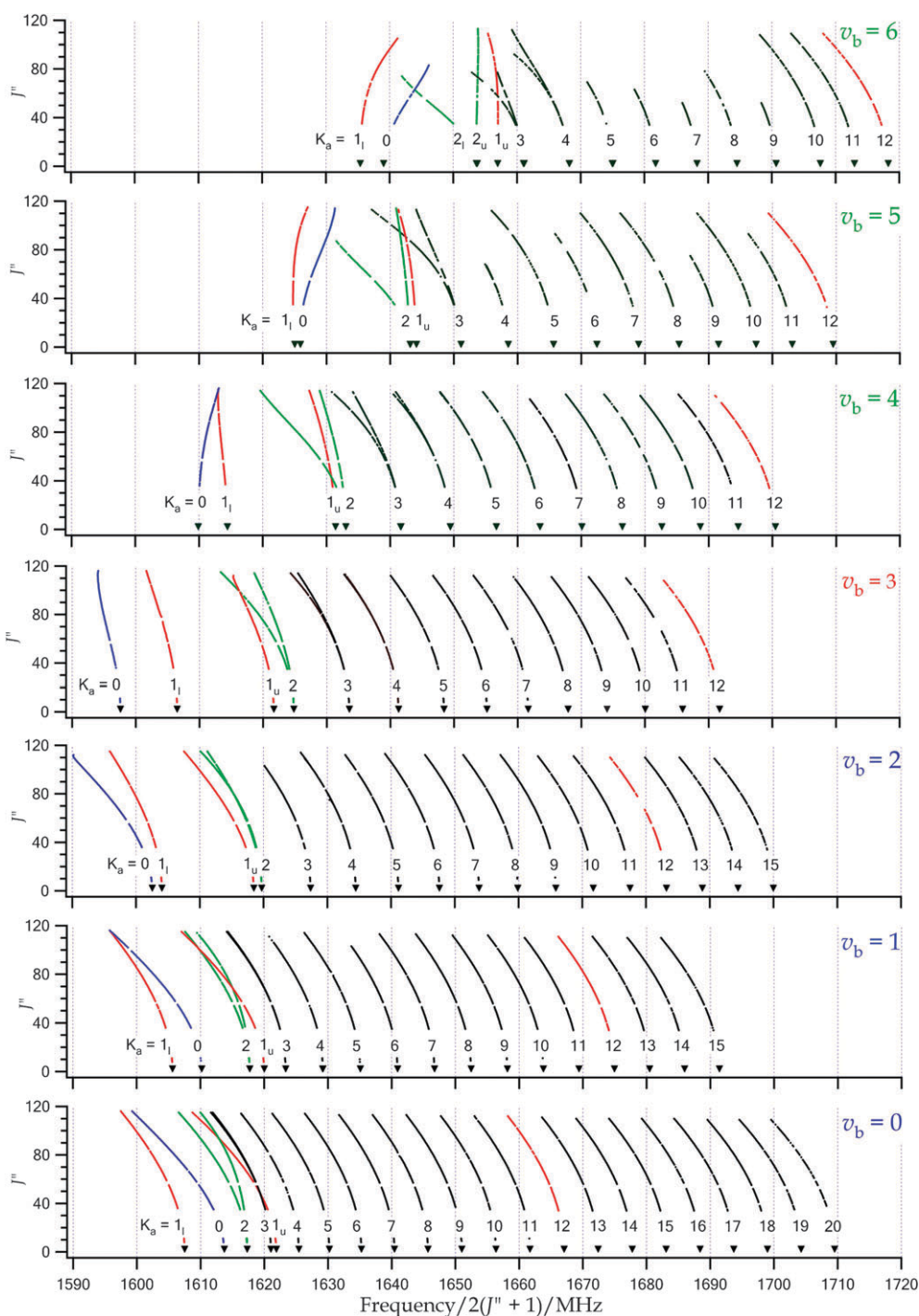
Fig. 8 Reduced Fortrat diagram of the assigned rotational frequencies of NCNCS in the ground state and the lowest 6 excited states of the quasi-linear bending mode v_b. The colors of the curves serve merely to distinguish the series of transitions with low K_a and to highlight $K_a = 12$ as representative of high K_a. The black triangles indicate the values of the experimentally determined B_{eff} values. The color coding for the v_b labels is the same as in Fig. 2 and 3.

contributions do not dominate the D_{eff} values, they are large enough to distort the fit if neglected. The lack of convergence of the series of coefficients observable in Table 3, is not a problem since the series alternates in sign and is simply the minimum number of constants sufficient to reproduce a rather large set of small, smooth, nearly flat contributions. These modest corrections can be attributed to non-resonant effects of the small-amplitude vibrations.

The agreement detailed in Tables 8–11 as well as in Fig. 9–11 between experimental and GSRB values shows that, although the GSRB model and our least squares strategy can not quite achieve experimental accuracy, the model does quantitatively reproduce all of the surprising and anomalous-seeming effects of monodromy.

The patterns seen for D_{eff} at low K_a are not actually surprising, when one realizes that they represent the effects
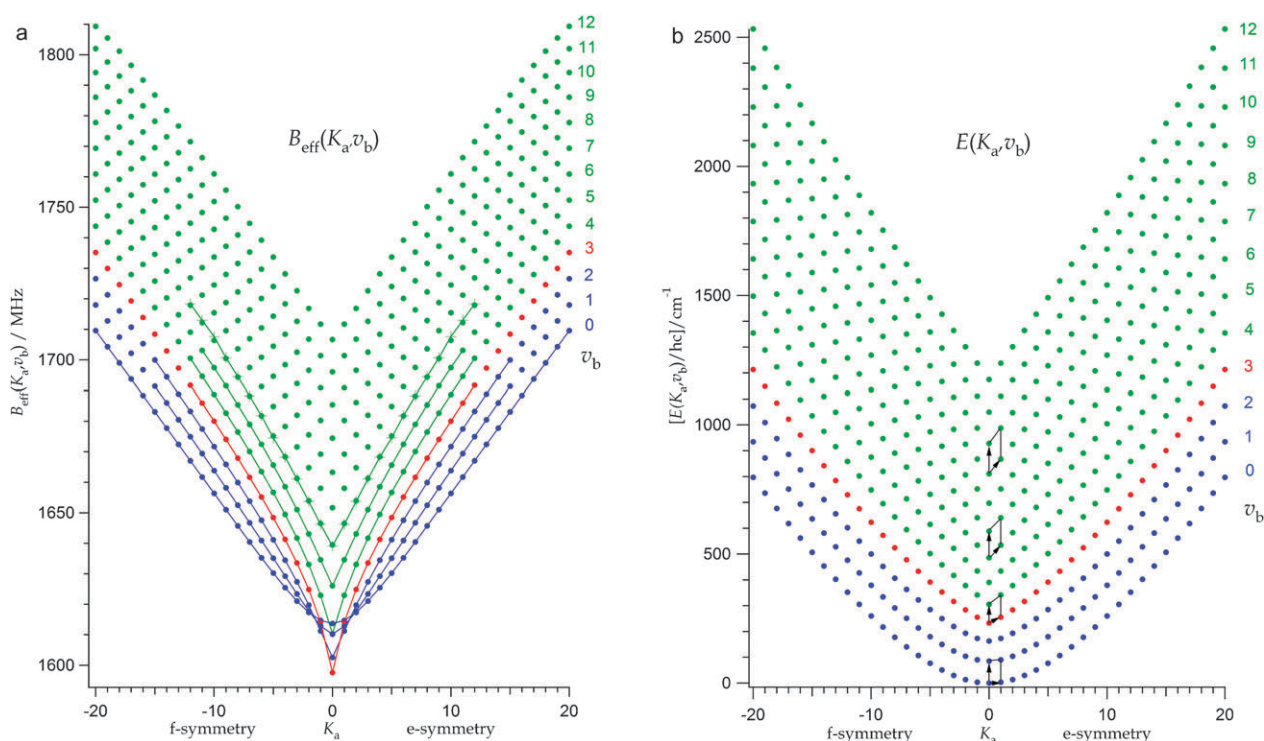
Fig. 9 Monodromy plots for NCNCS. Panel **a** shows the experimental and calculated quantum lattice of the effective rotational constants B_{eff} as a function of K_a and v_b, representing the end-over-end rotational energy contribution. The experimental B_{eff} values are connected by lines while the theoretical GSRB predictions are not. The experimental data for $v_b = 6$, which are shown as small crosses for visibility, were not included in the fitting. They are almost indistinguishable from the GSRB predictions. Panel **b** shows the corresponding two-dimensional energy-momentum map for NCNCS represented by the bending-rotation term values $E(K_a, v_b)$ plotted for $J = K_a$. The data due to asymmetry splitting for the lower K_a values were averaged, and the plots extended to $K_a < 0$ to be analogous to the classical case.

of $\Delta K = 2$ (in the symmetric top basis) interactions, over the whole range of v_b. These effects include a) asymmetry effects near the asymmetric rotor limit, in the lowest three v_b states ($v_b \leq 2$), (b) l-type doubling and l-type resonance near the linear limit in the upper three states ($v_b \geq 4$), and (c) interactions between the nearest levels of the appropriate K_a and symmetry, *regardless of vibrational identity*, near the monodromy point, indicated particularly by the indeterminate patterns of D_{eff} for $v_b = 3$. In each case, these effects show up prominently as a second order dependence of the frequencies on $J(J + 1)$, and thus in the value of D_{eff}.

The most remarkable example of the mapping of the properties of the potential function into the set of D_{eff} values is the reversal of the sign of the $K_a = 2$ splitting. The ordering of the two $K_a = 2$ levels in the ground state is just as you would expect for an asymmetric rotor: the upper level of the doublet (e symmetry in linear molecule notation, and $\mathbf{E}^+$ Wang matrix of an asymmetric rotor) is pushed up by the lower $K_a = 0$ level (also e, or $\mathbf{E}^+$). But that splitting decreases significantly for $v_b = 1$, and is extremely small for $v_b = 2$. In fact, when the entire measured range of J for $v_b = 2$ is considered, the splitting is observed to reverse at $J = 80$, as shown in Fig. 12. A look at the plot of $E(K_a, v_b)/hc$ (Fig. 9b) shown in the inset in Fig. 12 shows that for $v_b = 2$, the $K_a = 2^e$ level sees two $K_a = 0$ levels which are almost equally far away: one below, and one above. Because of the differences in B_{eff} values of the three levels, as J increases, the lower partner drifts farther away, and the upper one draws closer. The

splitting reverses, since the other $K_a = 2$ level (f-symmetry and $\mathbf{E}^-$) does not interact with $K_a = 0$. For $v_b > 2$ the inversion of the $K_a = 2$ levels is maintained, and the splitting increases rapidly in magnitude, as the $K_a = 2$ levels approach the upper $K_a = 0$ level more and more closely. The inversion of the splitting of the transitions, thus also of the doublet energy levels, reflects the loss of physical significance of the vibrational quantum number in the region of the monodromy point. The molecule does not, however, become truly linear: the anharmonicity represented by the barrier prevents the $K_a = 2$ doublet levels from rising above the $K_a = 0$ level carrying the next higher v_b label, even for high v_b (see Fig. 9b).

As can be seen in Table 10, the residuals of the B_{eff} values for $v_b = 5$, $K_a \geq 10$ do not follow the trend for lower K_a values. Also, for $v_b = 6$ the equivalent comparison for D_{eff} values revealed that as a function of K_a the observed D_{eff} values scatter irregularly around the smooth trend of the GSRB + CD-calculated values (see Table 11). It seems likely that these highly excited levels may be interacting with other nearby modes; the other four bending fundamentals are predicted[1] to lie between 430 and 483 cm^{-1}, which increases the density of interacting states rapidly. We have therefore excluded B_{eff} and D_{eff} values for $v_b = 5$, $K_a \geq 10$ and all values for $v_b = 6$ from the least-squares fitting. Thus any agreement between the observed values and the GSRB + CD-calculated values for these quantities indicates the extrapolative power of the GSRB + CD model. The fitted
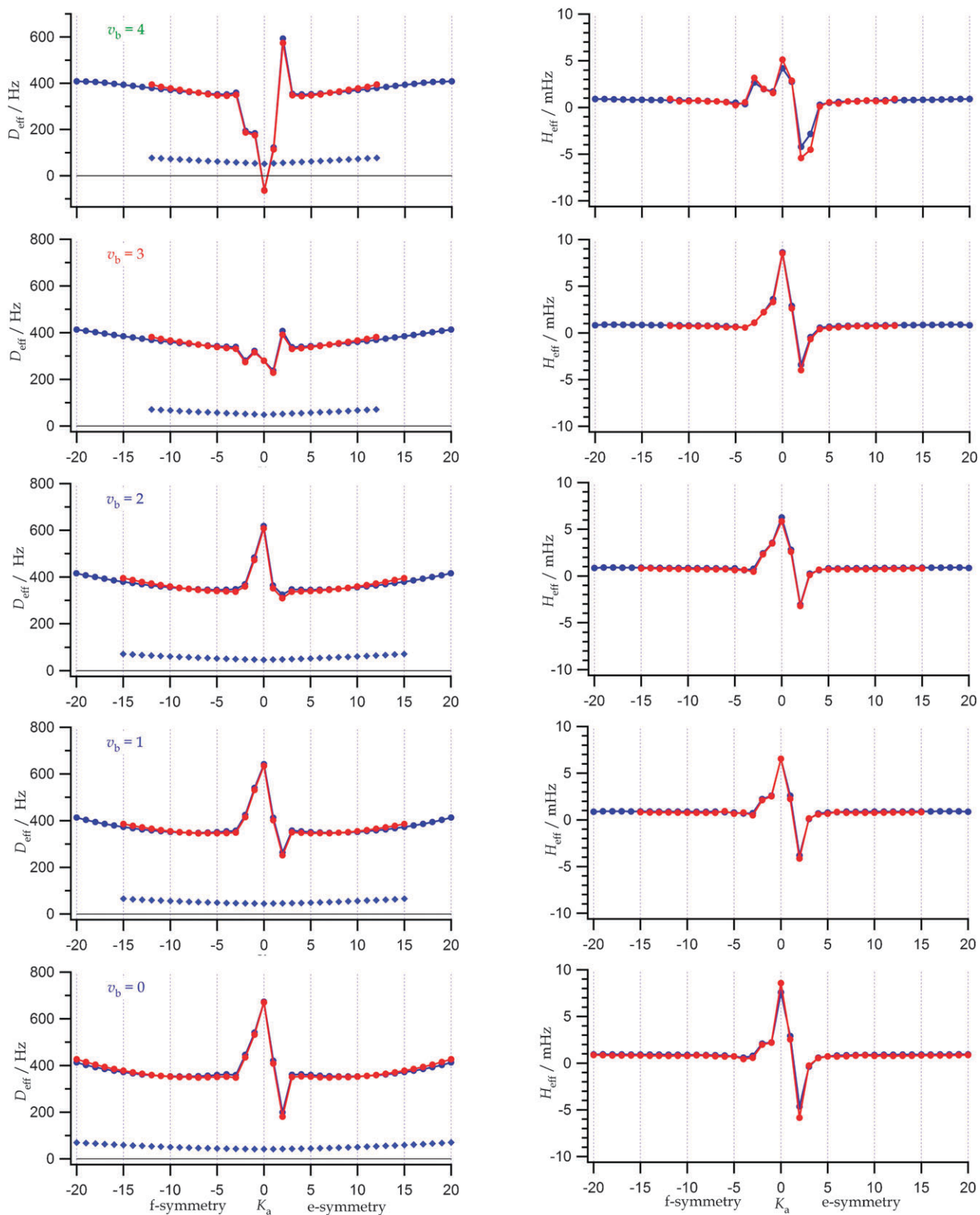
Fig. 10 Experimentally determined effective centrifugal distortion constants D_{eff} and H_{eff} for NCNCS in the states $v_b = 0$ to 4, shown in red, overlaid on those calculated by the fitted GSRB Hamiltonian, shown in blue. Values for e-symmetry levels are plotted at $K_a \geq 0$, while those for f-symmetry are plotted at $K_a < 0$. The curves defined by blue diamonds show the total contribution of the centrifugal distortion correction term [eqn (42)–(43)].

values of B_{eff}, while not providing experimental accuracy, are all within 0.26 MHz of experiment, with the exception of two

values for $v_b = 5$, and the fitted D_{eff} are all within 10 Hz of experiment.
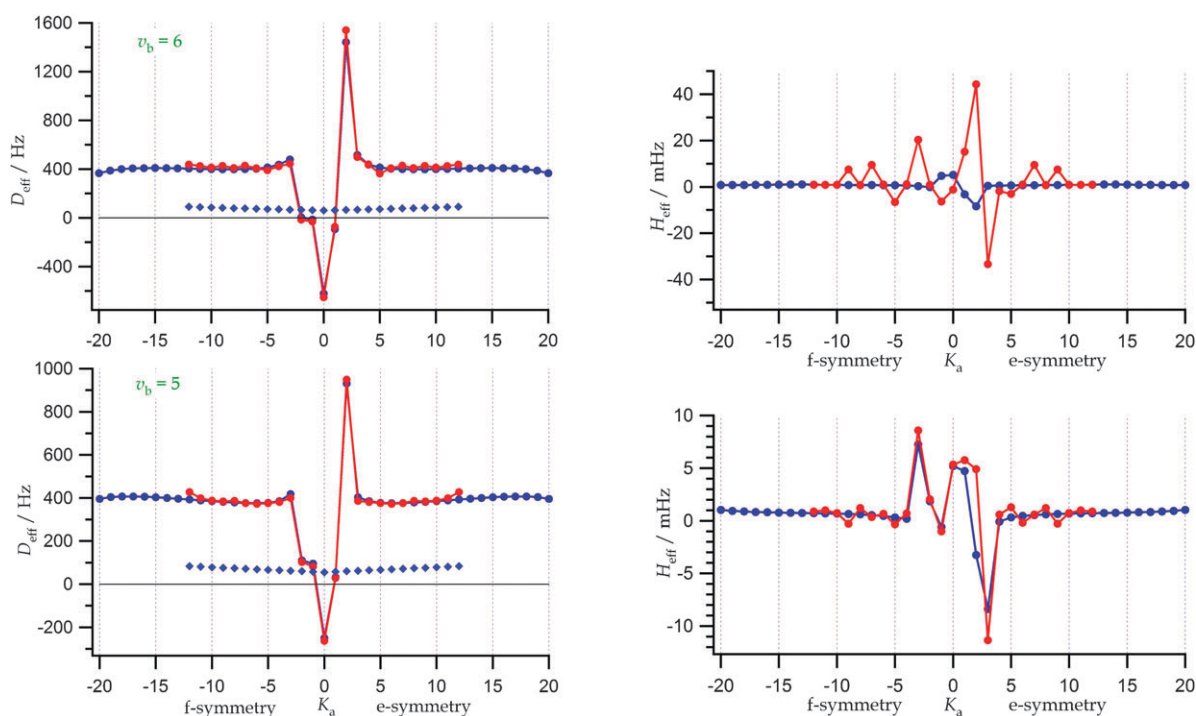
Fig. 11 Experimentally determined effective centrifugal distortion constants D_{eff} and H_{eff} for NCNCS in the states $v_b = 5$ and 6, shown in red, overlaid on those calculated by the fitted GSRB Hamiltonian, shown in blue. Values for e-symmetry levels are plotted at $K_a \geq 0$, while those for f-symmetry are plotted at $K_a < 0$. The curves defined by blue diamonds show the total contribution of the centrifugal distortion correction term [eqn (42)–(43)].

H_{eff} values were also extracted from the GSRB + CD-calculated energies and are also compared with the experimental values in Tables 8–11. The observed and GSRB + CD-calculated values are shown in the right hand panels of Fig. 10 and 11. The parameter H_{eff} was determined from polynomial fits to both the experimental and GSRB transition frequencies, but was not included in the fits. Again, we see a distinctive pattern (right-hand panels of Fig. 10 and 11) which undergoes a characteristic transformation as v_b increases, and we see that the predictions and the observed patterns coincide closely up until $v_b = 6$. This good agreement helps to confirm the assignments through $v_b = 5$, and indicates again the effect of accidental resonances becoming significant for $v_b = 5$ and especially 6. The large deviations found for $v_b = 6$ are so far from the predictions that they must be the result of inter-actions with other states.

The doublet reversal seen in the patterns for D_{eff} is not observed and not expected for H_{eff} in Fig. 10 and 11. For $K_a = 3$, the ordering follows that of $K_a = 1$, yielding a third order dependence of the splitting on $J(J + 1)$, and the doublet sequence remains as for an asymmetric rotor. For $K_a = 4$, the GSRB predictions indicate that an inversion occurs at $v_b = 2$, following that of the $K_a = 2$ levels. It appears from the plot of $E(K_a, v_b)$ /hc *versus* K_a in Fig. 9b that the $K_a = 6$ doublet will invert at $v_b = 1$. We conclude that the odd K_a doublets will not invert, but the even K_a doublets must all invert. These conclusions are the basis for the assignments of e and f symmetry in Tables 8–11. The assignment is consistent with the GSRB calculations, with what has previously been observed for quasi-linear molecules close to the linear limit, and with the special role of the $K_a = 0$ levels for even K_a, in particular the E^+ Wang block of eigenvalues.

Thus, to summarize this, another aspect of the mapping of monodromy into the spectrum is given by Fig. 13, which shows the splitting of the three resolved low K_a doublets as a function of v_b. Both the experimental splittings and those predicted from the final GSRB calculation are plotted. The $K_a = 1$ splitting, represented as the difference ΔB_{eff} between the e and f transitions, shows a pronounced kink, going from the nearly constant value typical of the inertial splitting in an asymmetric rotor to a strong linear dependence, typical of the *l*-type doubling of a linear molecule, as noted in section 5.6.1 of ref. 2. The $K_a = 2$ splitting is shown as a plot of the difference ΔD_{eff} between the transitions since they share a common B_{eff} and the splitting is dominated by a second order term. This splitting is monotonic, but passes through zero near the monodromy point, increasing in magnitude rapidly above it. For $K_a = 3$ we consider ΔH_{eff}, since the splitting between the e and f components is a third-order term in the Wang approximation of a rigid rotor. This inertial term is very small in an asymmetric rotor when it is as close to a symmetric rotor as NCNCS is already in its ground state. It is initially nearly constant with v_b, as expected for an inertial parameter depending on a given geometry, but reaches a minimum at $v_b = 2$. At higher v_b it is dominated by the $\Delta K_a = 2$ interactions of $K_a = 3$ with $K_a = 1$ levels both above and below it, and must therefore increase rapidly with v_b.

5.2 Resonance interactions

A variety of local resonance interactions were identified in the spectrum. These are listed in Table 12 and lead to anomalously large deviations of the B_{eff}, D_{eff}, and H_{eff} values for some of the

This journal is © the Owner Societies 2010

Phys. Chem. Chem. Phys., 2010, **12**, 8158–8189 | 8179

Table 8 Comparison between experimentally determined effective rotational and centrifugal distortion constants for NCNCS and their GSRB calculated values in the vibrational bending states v_b = 0 and 1 for different values of K_a. The least squares optimization was applied to these constants. The first column of data, $E_{origin} = E(K_a, v_b, J = K_a, e/f)$, is the calculated term value of the lowest level of each J-manifold, with $J = K_a$ as indicated by the quantum numbers and symmetry (e,f) in the first 5 columns. The effective spectroscopic constants B_{eff}, D_{eff}, and H_{eff} are functions of v_b, K_a and symmetry.

v_b	J	K_a	K_c	e/f	L/U	E_{origin}/ cm⁻¹	B_{eff}(obs)/ MHz	B_{eff}(cal)/ MHz	(Obs − cal)/ MHz	D_{eff}(obs)/ Hz	D_{eff}(cal)/ Hz	(Obs − cal)/ Hz	H_{eff}(obs)/ mHz	H_{eff}(cal)/ mHz	(Obs − cal)^a/ mHz
0	0	0	0	e		0.000	1613.720	1613.889	−0.168	671.19	675.26	−4.07	8.58	7.69	0.89
0	1	1	1	e	U	3.418	1607.505	1607.556	−0.051	408.82	411.57	−2.76	2.55	2.94	−0.39
0	1	1	0	f	L	3.418	1621.897	1622.141	−0.244	532.20	532.97	−0.76	2.19	2.23	−0.04
0	2	2	1	f	U	13.377	1617.318	1617.409	−0.080	435.91	436.55	−0.64	1.98	2.11	−0.13
0	2	2	0	e	L	13.377	1617.329	1617.409	−0.091	181.28	175.94	5.34	−5.85	−4.74	−1.11
0	3	3	1	e	U	29.243	1621.042	1621.056	−0.010	350.93	347.30	3.63	−0.25	−0.39	0.14
0	3	3	0	f	L	29.243	1621.046	1621.056	−0.014	349.10	347.28	1.82	0.57	0.78	−0.21
0	4	4	1	f	U	50.322	1625.429	1625.387	0.039	352.68	351.62	1.05	0.44	0.58	−0.14
0	4	4	0	e	L	50.322	1625.426	1625.387	0.042	353.63	351.62	2.01	0.53	0.58	−0.05
0	5	5	1	e		75.987	1630.221	1630.138	0.083	352.12	350.24	2.66	0.72	0.74	0.08
0	5	5	0	f		75.987	1630.221	1630.138	0.078	352.12	350.24	1.11	0.72	0.74	−0.12
0	6	6	1	f		105.705	1635.250	1635.149	0.101	349.62	348.46	1.16	0.71	0.81	−0.10
0	6	6	0	e		105.705	1635.250	1635.149	0.101	349.62	348.46	1.16	0.71	0.81	−0.10
0	7	7	1	e		139.035	1640.429	1640.321	0.109	348.58	347.56	1.02	0.74	0.85	−0.11
0	7	7	0	f		139.035	1640.429	1640.321	0.109	348.58	347.56	1.02	0.74	0.85	−0.11
0	8	8	0,1	e,f		175.607	1645.698	1645.589	0.109	349.36	347.83	1.53	0.80	0.86	−0.06
0	9	9	0,1	e,f		215.114	1651.016	1650.916	0.100	350.90	349.26	1.64	0.84	0.89	−0.05
0	10	10	0,1	e,f		257.297	1656.354	1656.274	0.081	352.44	351.77	0.68	0.77	0.89	−0.13
0	11	11	0,1	e,f		301.934	1661.708	1661.646	0.062	355.89	355.27	0.62	0.78	0.90	−0.12
0	12	12	0,1	e,f		348.838	1667.061	1667.021	0.040	360.04	359.69	0.35	0.77	0.91	−0.14
0	13	13	0,1	e,f		397.843	1672.412	1672.392	0.020	365.34	364.98	0.36	0.79	0.91	−0.12
0	14	14	0,1	e,f		448.807	1677.752	1677.751	0.000	371.24	371.13	0.11	0.79	0.92	−0.13
0	15	15	0,1	e,f		501.604	1683.082	1683.097	−0.015	378.37	378.12	0.24	0.82	0.93	−0.10
0	16	16	0,1	e,f		556.122	1688.398	1688.426	−0.028	385.92	385.99	−0.07	0.81	0.93	−0.12
0	17	17	0,1	e,f		612.264	1693.702	1693.737	−0.035	394.49	394.78	−0.29	0.81	0.94	−0.13
0	18	18	0,1	e,f		669.940	1698.993	1699.028	−0.035	404.24	404.58	−0.34	0.82	0.95	−0.12
0	19	19	0,1	e,f		729.071	1704.272	1704.299	−0.026	415.30	415.49	−0.19	0.85	0.95	−0.11
0	20	20	0,1	e,f		789.585	1709.539	1709.549	−0.010	427.67	427.69	−0.03	0.87	0.93	−0.05
1	0	0	0	e		85.037	1610.212	1610.426	−0.214	634.49	641.67	−7.19	6.55	6.64	−0.09
1	1	1	1	e	L	90.100	1605.638	1605.696	−0.058	401.03	405.33	−4.30	2.25	2.62	−0.37
1	1	1	0	f	U	90.100	1620.032	1620.232	−0.201	531.26	534.44	−3.18	2.52	2.61	−0.09
1	2	2	1	f	L	103.596	1617.747	1617.791	−0.045	415.54	417.94	−2.39	2.11	2.24	−0.12
1	2	2	0	e	U	103.596	1617.743	1617.791	−0.048	250.14	246.46	3.68	−4.14	−3.90	−0.24
1	3	3	1	e	L	123.667	1623.383	1623.377	0.006	349.80	348.89	0.91	0.15	0.08	−0.07
1	3	3	0	f	U	123.667	1623.377	1623.377	0.000	347.95	348.88	−0.92	0.50	0.71	−0.21
1	4	4	1	f	L	149.016	1629.219	1629.190	0.029	348.46	347.47	1.00	0.79	0.68	0.11
1	4	4	0	e	U	149.016	1629.217	1629.190	0.028	347.41	347.47	−0.06	0.58	0.68	−0.10
1	5	5	1	e	L	178.764	1635.083	1635.049	0.034	345.06	345.52	−0.47	0.65	0.79	−0.13
1	5	5	0	f	U	178.764	1635.083	1635.049	0.034	345.06	345.52	−0.47	0.65	0.79	−0.14
1	6	6	0	e	L	212.289	1640.926	1640.892	0.035	346.17	344.92	1.24	0.85	0.81	0.13
1	6	6	1	f	U	212.289	1640.925	1640.892	0.033	345.54	344.92	0.62	0.94	0.81	0.03
1	7	7	1	e	L	249.129	1646.718	1646.694	0.024	345.75	345.67	0.08	0.75	0.89	−0.14
1	7	7	0	f	U	249.129	1646.718	1646.694	0.024	345.75	345.67	0.08	0.75	0.89	−0.14
1	8	8	0,1	e,f		288.925	1652.460	1652.449	0.011	347.76	347.76	0.00	0.75	0.87	−0.12
1	9	9	0,1	e,f		331.392	1658.152	1658.154	−0.003	350.65	350.83	−0.17	0.75	0.88	−0.13
1	10	10	0,1	e,f		376.296	1663.796	1663.811	−0.015	354.69	354.79	−0.11	0.76	0.88	−0.12
1	11	11	0,1	e,f		423.441	1669.395	1669.422	−0.026	359.39	359.56	−0.17	0.76	0.89	−0.13
1	12	12	0,1	e,f		472.661	1674.954	1674.988	−0.033	365.01	365.07	−0.06	0.78	0.89	−0.11
1	13	13	0,1	e,f		523.812	1680.474	1680.511	−0.037	371.15	371.29	−0.14	0.78	0.91	−0.13
1	14	14	0,1	e,f		576.771	1685.960	1685.994	−0.034	378.05	378.18	−0.14	0.78	0.90	−0.12
1	15	15	0,1	e,f		631.426	1691.414	1691.439	−0.025	385.97	385.77	0.19	0.82	0.91	−0.09
1	16	16	0,1	e,f		687.683		1696.848			394.08			0.91	
1	17	17	0,1	e,f		745.453		1702.221			403.15			0.92	
1	18	18	0,1	e,f		804.661		1707.561			413.05			0.93	
1	19	19	0,1	e,f		865.236		1712.869			423.83			0.93	
1	20	20	0,1	e,f		927.116		1718.146			435.61			0.90	

^{a} H_{eff} values were not included in the GSRB fitting.

series, since not quite all transitions affected could be given zero weight in the power series fittings. The differences in K_a values for each of these pairs of interacting levels indicate that they are all second or higher order Coriolis-type interactions.

One of these resonances is illustrated in Fig. 14. Using the symmetry notation of a linear molecule, we see that the v_b, K_a = 2, 4^e/3, 1^e levels cross at J = 76, while the v_b, K_a = 2, 4^f/3, 1^f levels have an avoided crossing at J about 110. The degeneracy of the pair of v_b, K_a = 2, 4$^{e/f}$ levels is lifted over the

v_b	J	K_a	K_c	e/f	L/U	E_{origin}/ cm⁻¹	B_{eff}(obs)/ MHz	B_{eff}(cal)/ MHz	(Obs − cal)/ MHz	D_{eff}(obs)/ Hz	D_{eff}(cal)/ Hz	(Obs − cal)/ Hz	H_{eff}(obs)/ mHz	H_{eff}(cal)/ mHz	(Obs − cal)[a]/ mHz
2	0	0	0	e		162.940	1602.535	1602.557	−0.022	605.36	613.13	−7.77	5.85	6.35	−0.50
2	1	1	1	e	L	173.029	1604.055	1603.955	0.100	351.10	354.37	−3.27	2.59	2.83	−0.24
2	1	1	0	f	U	173.029	1618.486	1618.446	0.040	472.54	475.93	−3.39	3.48	3.58	−0.10
2	2	2	1	f	L	192.708	1619.730	1619.650	0.080	359.29	361.25	−1.97	2.31	2.44	−0.13
2	2	2	0	e	U	192.708	1619.728	1619.650	0.078	309.00	308.81	0.19	−3.22	−3.15	−0.06
2	3	3	1	e	L	218.522	1627.377	1627.315	0.062	337.31	338.32	−1.01	0.11	0.23	−0.12
2	3	3	0	f	U	218.522	1627.375	1627.315	0.061	336.48	338.32	−1.85	0.45	0.77	−0.32
2	4	4	0	e	L	248.975	1634.460	1634.419	0.041	338.18	338.35	−0.17	0.66	0.62	0.04
2	4	4	1	f	U	248.975	1634.459	1634.419	0.041	338.10	338.35	−0.25	0.66	0.62	0.04
2	5	5	1	e	L	283.237	1641.158	1641.141	0.017	339.20	339.43	−0.24	0.70	0.82	−0.12
2	5	5	0	f	U	283.237	1641.156	1641.141	0.015	338.56	339.43	−0.87	0.62	0.82	−0.20
2	6	6	0	e	L	320.774	1647.588	1647.592	−0.004	341.60	341.96	−0.36	0.71	0.81	−0.10
2	6	6	1	f	U	320.774	1647.588	1647.592	−0.004	341.60	341.96	−0.36	0.71	0.81	−0.10
2	7	7	1	e	L	361.203	1653.817	1653.841	−0.024	344.68	345.33	−0.66	0.70	0.82	−0.12
2	7	7	0	f	U	361.203	1653.817	1653.841	−0.024	344.68	345.33	−0.66	0.70	0.82	−0.12
2	8	8	0,1	e,f		404.232	1659.895	1659.933	−0.038	348.75	349.47	−0.72	0.71	0.84	−0.12
2	9	9	0,1	e,f		449.628	1665.852	1665.899	−0.047	353.64	354.27	−0.63	0.72	0.84	−0.12
2	10	10	0,1	e,f		497.203	1671.710	1671.759	−0.050	359.11	359.65	−0.54	0.74	0.85	−0.11
2	11	11	0,1	e,f		546.794	1677.484	1677.531	−0.046	365.01	365.58	−0.56	0.74	0.86	−0.12
2	12	12	0,1	e,f		598.265	1683.190	1683.224	−0.034	371.74	372.01	−0.27	0.76	0.87	−0.10
2	13	13	0,1	e,f		651.499	1688.834	1688.850	−0.016	378.66	378.96	−0.30	0.75	0.87	−0.12
2	14	14	0,1	e,f		706.389	1694.427	1694.413	0.013	386.81	386.41	0.40	0.81	0.88	−0.07
2	15	15	0,1	e,f		762.846	1699.972	1699.922	0.050	394.94	394.38	0.55	0.80	0.89	−0.08
2	16	16	0,1	e,f		820.786		1705.379			402.88			0.89	
2	17	17	0,1	e,f		880.137		1710.789			411.95			0.90	
2	18	18	0,1	e,f		940.831		1716.156			421.61			0.91	
2	19	19	0,1	e,f		1002.809		1721.481			431.88			0.92	
2	20	20	0,1	e,f		1066.017		1726.767			442.74			0.89	
3	0	0	0	e		232.259	1597.587	1597.341	0.247	279.74	276.74	3.00	8.53	8.72	−0.19
3	1	1	1	e	L	254.736	1606.498	1606.335	0.163	228.41	228.70	−0.29	2.63	2.92	−0.29
3	1	1	0	f	U	254.736	1621.689	1621.509	0.180	315.54	315.07	0.47	3.29	3.66	−0.36
3	2	2	0	e	L	283.013	1624.840	1624.724	0.116	392.05	394.57	−2.52	−4.00	−3.47	−0.53
3	2	2	1	f	U	283.013	1624.836	1624.723	0.113	273.37	273.08	0.29	2.21	2.25	−0.04
3	3	3	1	e	L	315.442	1633.555	1633.495	0.060	329.54	331.03	−1.49	−0.68	−0.48	−0.20
3	3	3	0	f	U	315.442	1633.560	1633.495	0.064	331.16	331.06	0.10	1.09	1.11	−0.02
3	4	4	0	e	L	351.302	1641.285	1641.260	0.024	334.31	334.30	0.01	0.57	0.55	0.02
3	4	4	1	f	U	351.302	1641.282	1641.260	0.022	333.37	334.30	−0.94	0.40	0.57	−0.17
3	5	5	1	e	L	390.148	1648.421	1648.429	−0.008	338.31	338.78	−0.48	0.62	0.66	−0.04
3	5	5	0	f	U	390.148	1648.421	1648.429	−0.008	338.15	338.78	−0.64	0.54	0.66	−0.12
3	6	6	0	e	L	431.663	1655.172	1655.202	−0.030	342.96	343.80	−0.84	0.61	0.72	−0.11
3	6	6	1	f	U	431.663	1655.172	1655.202	−0.030	342.96	343.80	−0.84	0.61	0.72	−0.11
3	7	7	1	e	L	475.602	1661.651	1661.694	−0.043	348.47	349.19	−0.72	0.66	0.75	−0.09
3	7	7	0	f	U	475.602	1661.651	1661.694	−0.043	348.47	349.19	−0.72	0.66	0.75	−0.09
3	8	8	0,1	e,f		521.765	1667.927	1667.973	−0.046	354.54	354.92	−0.39	0.72	0.78	−0.05
3	9	9	0,1	e,f		569.989	1674.043	1674.084	−0.042	360.33	360.98	−0.65	0.70	0.79	−0.09
3	10	10	0,1	e,f		620.133	1680.032	1680.060	−0.029	366.78	367.36	−0.59	0.72	0.81	−0.09
3	11	11	0,1	e,f		672.076	1685.918	1685.923	−0.004	373.43	374.06	−0.63	0.70	0.82	−0.13
3	12	12	0,1	e,f		725.711	1691.719	1691.688	0.031	381.28	381.09	0.19	0.77	0.83	−0.06
3	13	13	0,1	e,f		780.945		1697.370			388.46			0.84	
3	14	14	0,1	e,f		837.696		1702.977			396.15			0.85	
3	15	15	0,1	e,f		895.887		1708.517			404.18			0.86	
3	16	16	0,1	e,f		955.451		1713.997			412.54			0.87	
3	17	17	0,1	e,f		1016.328		1719.421			421.22			0.88	
3	18	18	0,1	e,f		1078.462		1724.794			430.19			0.90	
3	19	19	0,1	e,f		1141.801		1730.119			439.35			0.91	
3	20	20	0,1	e,f		1206.299		1735.398			448.66			0.91	

[a] H_{eff} values were not included in the GSRB fitting.

range of J from 68 to 83 by the Coriolis interaction involving the e-levels. Since the B_{eff} and D_{eff} values of all four of these interacting sequences of levels are well determined from the unperturbed lines, we can precisely determine the difference between the corresponding $[E(k \equiv K_a = J, v_b)/hc]/cm^{-1}$ term values, quantities which are among the eigenvalues calculated by the GSRB. We can use this as a test of the GSRB + CD's accuracy in determining the vibrational energy levels, despite the lack of vibrational data in the least-squares fitting. We do this by interpolating the sequence of the interacting levels

This journal is © the Owner Societies 2010

Phys. Chem. Chem. Phys., 2010, **12**, 8158–8189 | 8181

Table 10 Comparison between experimentally determined effective rotational and centrifugal distortion constants for NCNCS and their GSRB calculated values in the vibrational bending state $v_b = 4$ and 5 for different values of K_a. The least squares optimization was applied to these constants. The first column of data, $E_{origin} = E(K_a, v_b, J = K_a, e/f)$, is the calculated term value of the lowest level of each J-manifold, with $J = K_a$ as indicated by the quantum numbers and symmetry (e,f) in the first 5 columns. The effective spectroscopic constants B_{eff}, D_{eff}, and H_{eff} are functions of v_b, K_a and symmetry.

v_b	J	K_a	K_c	e/f	L/U	$E_{origin}/$ cm^{-1}	$B_{eff}(obs)/$ MHz	$B_{eff}(cal)/$ MHz	(Obs − cal)$^a/$ MHz	$D_{eff}(obs)/$ Hz	$D_{eff}(cal)/$ Hz	(Obs − cal)$^a/$ Hz	$H_{eff}(obs)/$ mHz	$H_{eff}(cal)/$ mHz	(Obs − cal)$^b/$ mHz
4	0	0	0	e		304.636	1609.873	1609.938	−0.065	−64.67	−74.16	9.49	5.12	4.28	0.85
4	1	1	1	e	L	340.463	1614.448	1614.456	−0.008	114.75	111.67	3.08	2.87	2.80	0.07
4	1	1	0	f	U	340.463	1631.418	1631.382	0.036	175.62	172.34	3.28	1.55	1.72	−0.17
4	2	2	0	e	L	377.137	1633.049	1633.038	0.011	574.03	579.68	−5.65	−5.42	−4.27	−1.14
4	2	2	1	f	U	377.137	1633.050	1633.037	0.012	186.97	185.13	1.84	2.00	1.98	0.02
4	3	3	1	e	L	415.878	1641.657	1641.685	−0.028	338.38	348.36	−9.99	−4.52	−2.91	−1.61
4	3	3	0	f	U	415.878	1641.686	1641.685	0.001	351.01	348.47	2.53	3.16	2.73	0.43
4	4	4	0	e	L	456.858	1649.454	1649.475	−0.021	346.65	345.81	0.84	0.55	0.28	0.27
4	4	4	1	f	U	456.858	1649.448	1649.475	−0.028	344.30	345.84	−1.54	0.11	0.36	−0.25
4	5	5	1	e	L	500.032	1656.674	1656.712	−0.038	348.33	348.98	−0.66	0.55	0.50	0.05
4	5	5	0	f	U	500.032	1656.671	1656.712	−0.040	346.96	348.98	−2.02	0.23	0.50	−0.27
4	6	6	0	e	L	545.300	1663.521	1663.561	−0.040	353.17	353.90	−0.73	0.56	0.60	−0.04
4	6	6	1	f	U	545.300	1663.519	1663.561	−0.042	352.39	353.90	−1.51	0.43	0.60	−0.17
4	7	7	1	e	L	592.551	1670.091	1670.123	−0.032	359.40	359.57	−0.17	0.66	0.66	0.00
4	7	7	0	f	U	592.551	1670.091	1670.123	−0.032	359.40	359.57	−0.17	0.66	0.66	0.00
4	8	8	0,1	e,f		641.677	1676.448	1676.464	−0.017	365.09	365.68	−0.59	0.64	0.70	−0.06
4	9	9	0,1	e,f		692.577	1682.639	1682.629	0.011	372.43	372.10	0.33	0.75	0.73	0.02
4	10	10	0,1	e,f		745.158	1688.693	1688.647	0.046	378.59	378.77	−0.19	0.66	0.76	−0.09
4	11	11	0,1	e,f		799.335	1694.633	1694.543	0.090	385.65	385.69	−0.04	0.65	0.77	−0.12
4	12	12	0,1	e,f		855.032	1700.486	1700.334	0.152	395.74	392.82	2.91	0.92	0.79	0.14
4	13	13	0,1	e,f		912.177		1706.033			400.16			0.80	
4	14	14	0,1	e,f		970.707		1711.652			407.68			0.82	
4	15	15	0,1	e,f		1030.563		1717.197			415.35			0.83	
4	16	16	0,1	e,f		1091.689		1722.676			423.12			0.84	
4	17	17	0,1	e,f		1154.037		1728.095			430.90			0.86	
4	18	18	0,1	e,f		1217.561		1733.457			438.58			0.89	
4	19	19	0,1	e,f		1282.218		1738.767			445.90			0.93	
4	20	20	0,1	e,f		1347.968		1744.025			452.53			0.88	
5	0	0	0	e		389.599	1625.678	1625.933	−0.255	−263.00	−262.91	−0.09	5.33	5.30	0.04
5	1	1	1	e	L	433.354	1624.807	1624.999	−0.192	28.18	22.24	5.94	5.76	4.82	0.94
5	1	1	0	f	U	433.354	1644.037	1644.170	−0.133	81.74	81.24	0.50	−1.01	−0.62	−0.39
5	2	2	0	e	L	476.531	1643.101	1643.157	−0.055	949.05	917.56	31.49	4.90	−3.24	8.14
5	2	2	1	f	U	476.531	1643.039	1643.155	−0.116	102.24	101.00	1.25	2.04	1.88	0.16
5	3	3	1	e	L	520.610	1651.033	1651.146	−0.113	387.34	400.96	−13.62	−11.34	−8.57	−2.77
5	3	3	0	f	U	520.610	1651.066	1651.146	−0.080	405.32	401.22	4.10	8.58	7.43	1.15
5	4	4	0	e	L	566.097	1658.551	1658.625	−0.074	376.70	378.32	−1.62	0.71	−0.09	0.69
5	4	4	1	f	U	566.097	1658.550	1658.625	−0.075	377.69	378.44	−0.75	0.60	0.19	0.52
5	5	5	1	e	L	613.165	1665.667	1665.703	−0.036	378.20	373.44	4.75	1.29	0.32	0.97
5	5	5	0	f	U	613.165	1665.645	1665.703	−0.058	369.04	373.45	−4.40	−0.33	0.32	−0.65
5	6	6	0	e	L	661.857	1672.450	1672.468	−0.018	375.16	374.47	0.69	0.66	0.46	0.20
5	6	6	1	f	U	661.857	1672.435	1672.468	−0.033	369.56	374.47	−4.91	−0.19	0.46	−0.65
5	7	7	1	e	L	712.161	1678.995	1678.984	0.011	377.66	378.05	−0.38	0.58	0.55	0.03
5	7	7	0	f	U	712.161	1678.990	1678.984	0.006	375.92	378.05	−2.13	0.35	0.55	−0.20
5	8	8	0,1	e,f		764.037	1685.365	1685.298	0.066	388.20	382.91	5.29	1.20	0.61	0.59
5	9	9	0,1	e,f		817.437	1691.540	1691.445	0.094	384.15	388.53	−4.38	−0.28	0.66	−0.93
5	10	10	0,1	e,f		872.306	1697.444	1697.451	−0.008	388.76	394.61	−5.85	0.74	0.69	0.05
5	11	11	0,1	e,f		928.591	1703.107	1703.337	−0.229	398.29	401.02	−2.73	1.00	0.72	0.28
5	12	12	0,1	e,f		986.240	1709.539	1709.117	0.423	427.73	407.66	20.07	0.88	0.74	0.14
5	13	13	0,1	e,f		1045.202		1714.803			414.43			0.76	
5	14	14	0,1	e,f		1105.429		1720.407			421.26			0.78	
5	15	15	0,1	e,f		1166.876		1725.936			428.05			0.80	
5	16	16	0,1	e,f		1229.502		1731.396			434.67			0.82	
5	17	17	0,1	e,f		1293.266		1736.792			440.91			0.85	
5	18	18	0,1	e,f		1358.132		1742.129			446.50			0.90	
5	19	19	0,1	e,f		1424.063		1747.409			450.93			0.96	
5	20	20	0,1	e,f		1491.028		1752.634			453.60			1.03	

^{a} $v_b = 5$ levels with $K_a \geq 10$ were not included in the GSRB fitting. ^{b} H_{eff} values were not included in the GSRB fitting.

down to $J = 4$ and thus determining the vibration–rotation energy difference between $v_b = 3$, $K_a = 1^e$, $J = 4$, and $v_b = 2$, $K_a = 4^e$, $J = 4$. The experimentally determined difference is 5.49 cm^{-1}. The GSRB+CD values of these energy levels as listed in Table 9 differ by 6.73 cm^{-1}, within 1.25 cm^{-1} of the experimental value. Considering the use of only the pure rotational spectrum, as well as the limitations of the model and fitting procedure, this is an acceptable deviation. We note finally that all of the sets of resonance partners assigned in Table 12 are similarly consistent with the calculated energy

8182 | *Phys. Chem. Chem. Phys.*, 2010, **12**, 8158–8189

This journal is © the Owner Societies 2010

Table 11 Comparison between experimentally determined effective rotational and centrifugal distortion constants for NCNCS and their GSRB calculated values in the vibrational bending state $v_b = 6$ for different values of K_a. The least squares optimization was applied to these constants. The first column of data, $E_{origin} = E(K_a, v_b, J = K_a, e/f)$, is the calculated term value of the lowest level of each J-manifold, with $J = K_a$ as indicated by the quantum numbers and symmetry (e,f) in the first 5 columns. The effective spectroscopic constants B_{eff}, D_{eff}, and H_{eff} are functions of v_b, K_a and symmetry.

v_b	J	K_a	K_c	e/f	L/U	E_{origin}/ cm^{-1}	B_{eff}(obs)/ MHz	B_{eff}(cal)/ MHz	(Obs − cal)^a/ MHz	D_{eff}(obs)/ Hz	D_{eff}(cal)/ Hz	(Obs − cal)^a/ Hz	H_{eff}(obs)/ mHz	H_{eff}(cal)/ mHz	(Obs − cal)^b/ mHz
6	0	0	0	e		484.704	1639.059	1639.409	−0.350	−653.39	−628.35	−25.04	−1.18	5.13	−6.31
6	1	1	1	e	L	533.359	1635.410	1635.694	−0.285	−73.20	−92.45	19.25	15.21	10.52	4.69
6	1	1	0	f	U	533.359	1656.976	1657.189	−0.213	−30.72	−27.53	−3.19	−6.30	−5.29	−1.00
6	2	2	0	e	L	581.368	1653.762	1653.901	−0.139	1540.20	1438.35	101.85	44.30	5.22	39.08
6	2	2	1	f	U	581.368	1653.629	1653.897	−0.268	−15.46	−0.03	−15.43	0.88	1.99	−1.10
6	3	3	1	e	L	629.786	1661.025	1661.230	−0.204	443.46	491.22	−47.76	−33.41	−20.46	−12.95
6	3	3	0	f	U	629.786	1661.111	1661.230	−0.119	498.57	491.75	6.82	20.30	18.07	2.23
6	4	4	0	e	L	679.119	1668.199	1668.311	−0.112	421.96	433.89	−11.93	−1.82	−0.68	−1.14
6	4	4	1	f	U	679.119	1668.234	1668.311	−0.077	438.91	434.27	4.64	1.14	0.20	0.94
6	5	5	1	e	L	729.610	1675.052	1675.139	−0.087	391.30	413.91	−22.61	−3.00	0.11	−3.11
6	5	5	0	f	U	729.610	1674.959	1675.139	−0.180	364.00	413.91	−49.91	−6.60	0.13	−6.73
6	6	6	0	e	L	781.373	1681.770	1681.739	0.031	407.40	406.92	0.48	1.06	0.31	0.75
6	6	6	1	f	U	781.373	1681.770	1681.739	0.031	407.40	406.92	0.48	1.06	0.31	0.75
6	7	7	1	e	L	834.453	1688.258	1688.141	0.117	428.40	405.76	22.64	9.50	0.43	9.07
6	7	7	0	f	U	834.453	1688.258	1688.141	0.117	428.40	405.76	22.64	9.50	0.43	9.07
6	8	8	0,1	e,f		888.857	1694.533	1694.372	0.160	408.66	407.58	1.08	0.69	0.51	0.18
6	9	9	0,1	e,f		944.572	1700.688	1700.456	0.232	427.20	411.06	16.14	7.50	0.57	6.93
6	10	10	0,1	e,f		1001.577	1707.609	1706.411	1.197	413.72	415.54	−1.82	0.84	0.62	0.22
6	11	11	0,1	e,f		1059.840	1712.962	1712.253	0.709	425.37	420.62	4.76	0.88	0.65	0.23
6	12	12	0,1	e,f		1119.331	1718.291	1717.995	0.296	437.27	426.04	11.23	0.85	0.68	0.17
6	13	13	0,1	e,f		1180.014		1723.646			431.61			0.71	
6	14	14	0,1	e,f		1241.856		1729.215			437.12			0.73	
6	15	15	0,1	e,f		1304.825		1734.709			442.38			0.76	
6	16	16	0,1	e,f		1368.888		1740.134			447.12			0.80	
6	17	17	0,1	e,f		1434.013		1745.494			450.96			0.86	
6	18	18	0,1	e,f		1500.173		1750.792			453.37			0.94	
6	19	19	0,1	e,f		1567.337		1756.030			453.54			1.07	
6	20	20	0,1	e,f		1635.480		1761.209			450.13			1.16	

^{a} None of the $v_b = 6$ data was included in the GSRB fitting. ^{b} H_{eff} values were not included in the GSRB fitting.

level pattern of Fig. 9 b. As noted in section 5.1, the assigned series of lines for $v_b = 5$ and 6 show numerous further resonances which could not be assigned within the sequence of excited states of the quasi-linear bending mode.

5.3 Summary of the fitting, potential function, energy levels and wave functions

The *ab initio* values from Table 3 were used as the initial geometry for the GSRB calculations. The fitted GSRB + CD parameters are also given in Table 3. Those parameters not fitted were fixed to the *ab initio* values in the "Equ." column of Table 1. For comparison the last column of Table 3 gives the parameters from the 1988 GSRB fitting of the microwave data for the $v_b = 0$ to 3 levels of NCNCS.[8]

There is a wide variety of choice in deciding which geometric parameters to fit and which to leave at *ab initio* values. The final choice was guided by the quality of the resulting fits, both with respect to the final standard error and also with regard to the stability of the fitting. It must be remembered that, at least to first order, the GSRB geometry represents an averaging over the zero point motion of the small amplitude vibrations. It is therefore not strictly equivalent to the *ab initio* equilibrium geometry. With data from only one isotopologue it was only reasonable to fit one internuclear distance in such a nearly linear structure. In the fittings the best results were obtained by fitting the CS internuclear distance. This is not unreasonable

given the dominant mass of the sulfur atom. The final fitted value for r_{CS} is within 0.007 Å of the *ab initio* value.

Similarly, it was only possible to fit one internuclear distance semi-rigidity parameter. Initially the semi-rigidity of each of the four internuclear distances was taken from the *ab initio* calculations and each one of these values was adjusted in a least squares fit. However, neither that, nor scaling all the semi-rigidities by one parameter worked as well as simply choosing one internuclear distance semi-rigidity and adjusting it, fixing the remaining semi-rigidities to zero. The natural choice is the CS bond semi-rigidity, and adjusting this did result in the best fit. Again, due to this choice, as well as zero point averaging, the *ab initio* and fitted semi-rigidity are not strictly comparable. In the final least-squares fit given in Table 3 the one non-zero semi-rigidity constant takes the value 0.08 Å rad^{-2}. This value is quite close to the value 0.07 Å rad^{-2} that would be the sum of the *ab initio* semi-rigidities of all four internuclear distances. As has been seen before, the one fitted semi-rigidity essentially acts as a proxy for the overall increase or decrease in length of the molecule upon bending.

Finally, the *ab initio* calculated variation of the ∠NCN and ∠NCS bond-angles as a function of the bending coordinate could be well modeled by odd functions in ρ up to the cubic term. The *ab initio* calculations were done out to $\rho = 70°$. To ensure convergence of the GSRB calculations, the basis set was extended up to $v_b = 12$. This in turn required the GSRB calculation to extend to about $\rho = 120°$. Unfortunately the

This journal is © the Owner Societies 2010

Phys. Chem. Chem. Phys., 2010, **12**, 8158–8189 | 8183
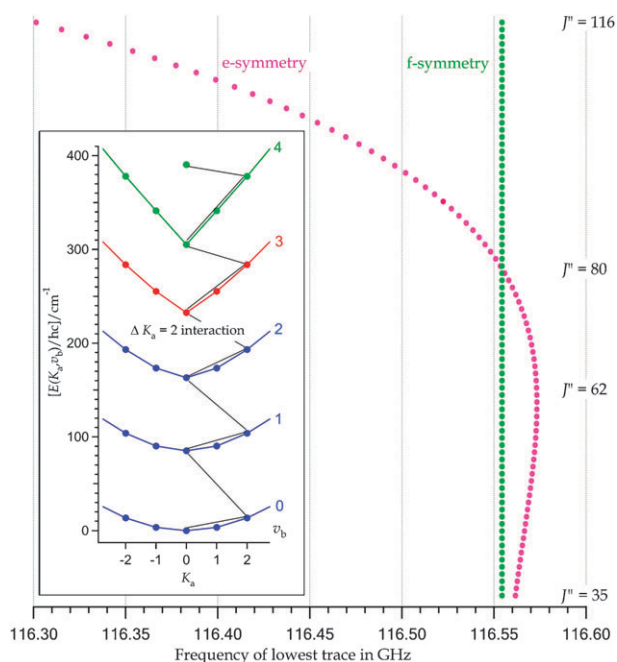
Fig. 12 Simplified CAAARS Loomis–Wood diagram of the splitting of the rotational transitions for $v_b = 2$, $K_a = 2$. The frequency points are calculated (polynomial fit to experimental data) to eliminate gaps; the deviations are less than the point width. The inversion of the splitting, so that the e component drops below the f component, true both for the transition frequency and the level energies, reflects the loss of significance of the vibrational quantum number in the region of the monodromy point. In the inset, an enlargement from Fig. 9b around the monodromy point, the $\Delta K_a = 2$ interactions are indicated by black lines connecting the $K_a = 0$ levels with the $K_a = 2$ levels.

cubic form for the variation of the $\angle$ NCN and $\angle$ NCS bond angles gave unreasonable values when extrapolated to such large angles and could not be used. Instead, as mentioned above, a linear variation was chosen, with $\angle$ NCN and $\angle$ NCS both set to 180° when $\rho = 0$ and to their *ab initio* calculated equilibrium values at $\rho = \rho_e$. The resulting linear function follows the *ab initio* variation quite well over the classically allowed regions.

The GSRB fitted potential energy function for the large amplitude bending motion is shown in Fig. 15. Also shown, by the round dots connected by an interpolated dashed line, are the *ab initio* potential energy values from Table 2. The GSRB potential energy function includes the variation with ρ of the zero-point energy of all the small-amplitude vibrations and is not expected to be identical to the *ab initio* function. In this context the good agreement between these two potential energy functions is quite satisfying.

The probability densities (PD), given by the squares of the vibrational wave functions, are shown in Fig. 15 for $K_a = 0$ with their baselines set at their term values, $[E(k, v_b)/hc]/\text{cm}^{-1}$. The wave functions, expressed in polar coordinates, are those defined in eqn (27). The resulting PDs are ρ-dependent and give the probability for a ring on a spherical surface of width $d\rho$, and thus refer to a volume element $d\rho$. These wave functions must all go to zero at $\rho = 0$, the linear configuration, which represents a singularity, as mentioned in section 2.2. The PDs so defined are labeled as $|\psi_\rho|^2$. To instead give a view
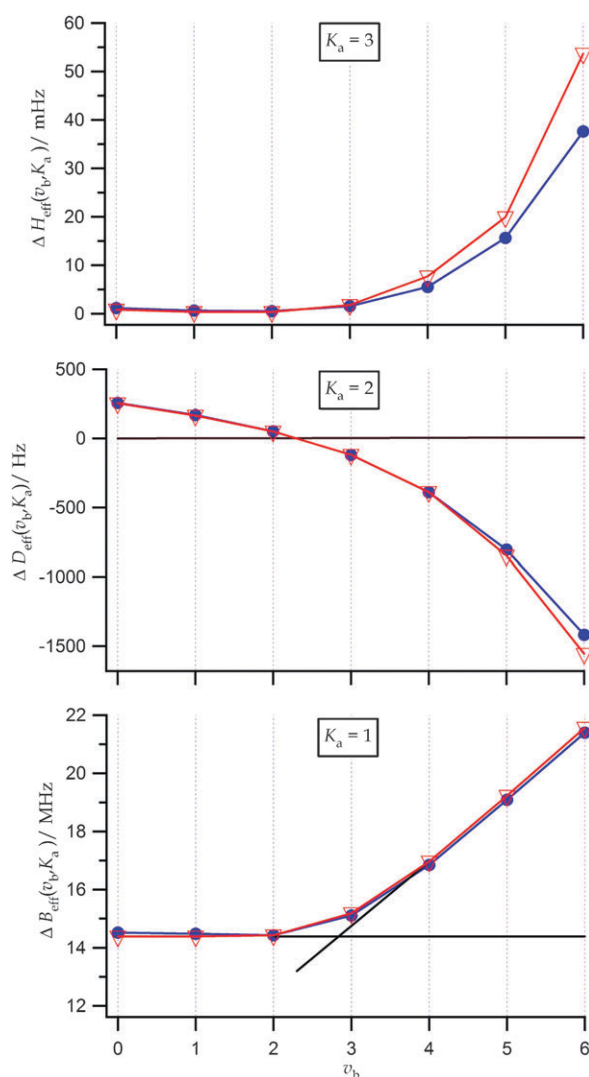
Fig. 13 Dependence on v_b of the splitting of transitions for $K_a = 1$, 2, and 3, represented by the dominant contributions ΔP_{eff}. These are ΔB_{eff} for $K_a = 1$, ΔD_{eff} for $K_a = 2$, and ΔH_{eff} for $K_a = 3$, where $\Delta P_{\text{eff}} = P_{\text{eff}}(v_b, K_a, \text{f}) - P_{\text{eff}}(v_b, K_a, \text{e})$. The GSRB values are shown as solid blue circles while the experimentally determined splittings are entered as open red triangles.

Table 12 Resonance interactions identified in the rotational spectrum of NCNCS, with level crossings at the indicated value of $J = J_c$

Lower		Upper			
v_b	K_a	v_b	K_a	ΔK_a	J_c
0	5[e]	1	1[e]	4	> 105
0	8[e,f]	1	5[e,f]	3	80
1	4[e]	2	0[e]	4	> 102
1	6[e,f]	2	3[e,f]	3	108
2	4[e]	3	1[e]	3	76
2	4[f]	3	1[f]	3	110
2	5	3	1	4	> 110

of the same wave function as it would appear in a cut through a Cartesian coordinate giving the distance of the nucleus C_1 from the axis defined by $r_{N_2C_2}$ (see Fig. 4), we can show the PD with the label $|\psi_c|^2$ appropriate to a normalization dx. This is

8184 | *Phys. Chem. Chem. Phys.*, 2010, **12**, 8158–8189

This journal is © the Owner Societies 2010
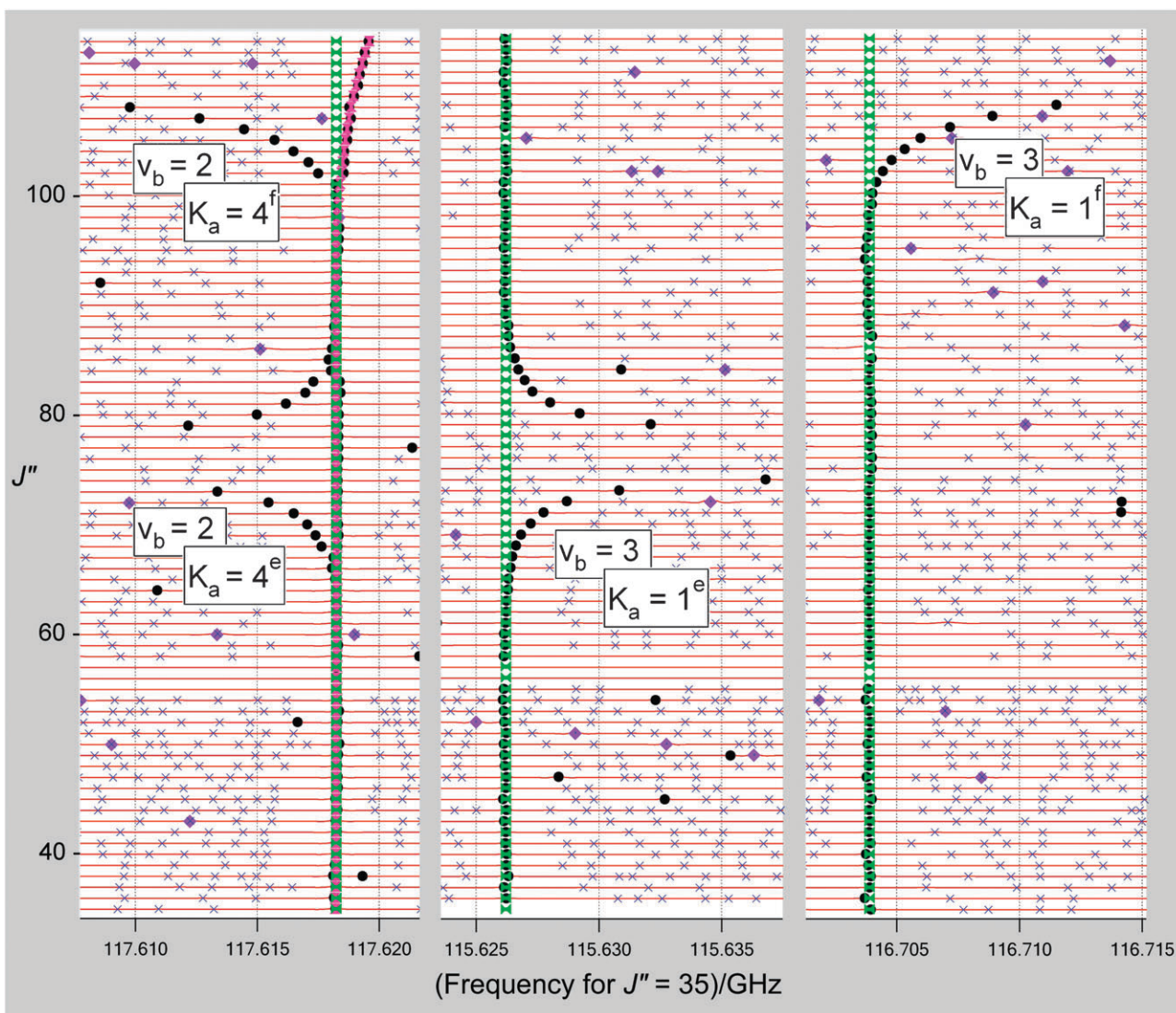
Fig. 14 Resonances between the levels v_b, $K_a = 2$, 4 and 3, 1 are shown in excerpts of three separate Loomis–Wood diagrams, each centered on the polynomial fitted to the unperturbed lines of the respective series of transitions affected. The e and f series for v_b, $K_a = 2$, 4 are degenerate up to $J'' = 102$, where the f component is affected by the resonance. The black dots are assigned transitions for $v_b = 2$ or 3, and the red and green markers are predictions from parameters determined from the unperturbed transitions in the interacting series. The blue crosses are unassigned peak position markers, and the purple markers are lines assigned to $v_b = 0$ or 1. Line intensities are suppressed in this presentation.

readily done by simply plotting $|\psi_c|^2 = |\psi_\rho|^2/\rho$,[16] shown by the dashed curves in Fig. 15. The abscissa for this wave function, shown at the top of Fig. 15, shows only half of the range of x for which this wave function is defined, since negative values are not shown; the values are given by $r_{C_1N_2} \sin \rho$. For $x < 0$ the PDs are identical to those for $x > 0$.

The resulting very different forms of the probability distributions have the property that they only really go to zero at linearity for non-zero angular momentum, *i.e.* $k \equiv K_a > 0$, in which case $\rho = 0$ is a true node of the wave function. For $K_a > 0$, therefore, the difference between the two sets of curves is of minor importance, and is not illustrated here. The abruptness of the change in the probability distributions at the monodromy point is seen in the $|\psi_c|^2$ curves in the amplitude at the linear configuration, and also in the change in the curvature of $|\psi_c|^2$ at $\rho = 0$.

5.4 Dipole moment functions and expectation values of ρ and ρ^2

As shown in Table 2 and Fig. 15b, the components of the electric dipole transition moment as obtained from *ab initio* calculations are not constant as a function of ρ, as assumed early in this study when the experimental intensities were roughly scaled. The expectation values of the two components in the large-amplitude basis functions of eqn (27),

$$\langle \Psi_{k \equiv K_a, v_b}(\rho) | \mu(\rho) | \Psi_{k \equiv K_a, v_b}(\rho) \rangle \qquad (47)$$

were calculated and are plotted for each v_b as a function of K_a in Fig. 16a (μ_a) and Fig. 16b (μ_b). These figures strongly resemble Fig. 9. Since the effective inertial constant and the dipole moment are quantities with completely independent physical properties, the striking similarity of their dependence on K_a and v_b indicates that this behaviour is related to how the

This journal is © the Owner Societies 2010

Phys. Chem. Chem. Phys., 2010, **12**, 8158–8189 | 8185
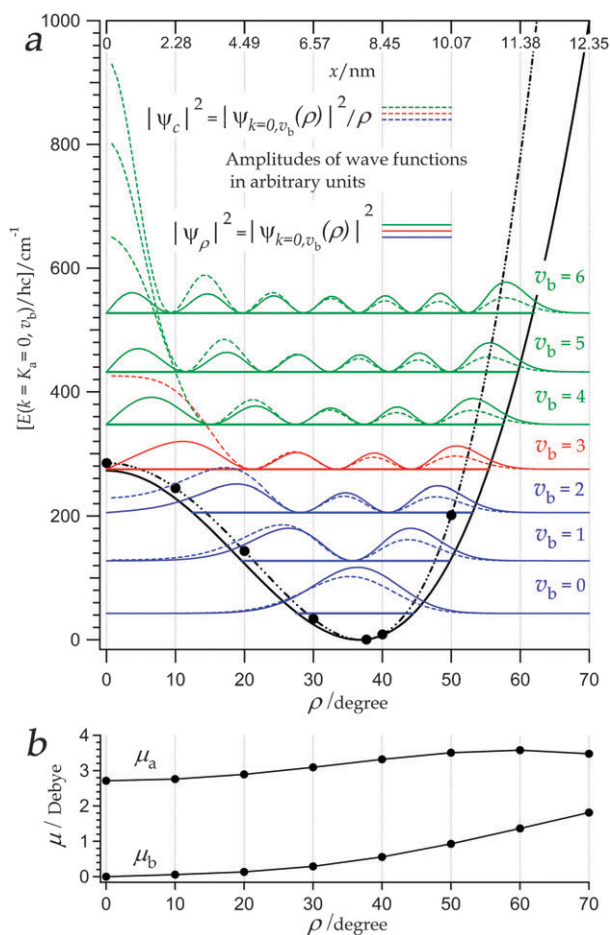
Fig. 15 In panel **a** the fitted potential energy of NCNCS as a function of ρ is displayed as a solid black line, and the *ab initio* values are given by the solid black circles connected by an interpolated curve. The probability densities for v_b, $K_a = 0$, as formulated for both polar and Cartesian coordinates, are shown with the color coding of Fig. 2. The squares of the conventional polar or radial wave-functions $|\psi\rho|^2$ are shown as solid lines and refer to the lower abscissa scale in ρ, while those of Cartesian wave-functions $|\psi_c|^2$ are shown as dashed lines and refer to the upper abscissa scale in the displacement coordinate x (see text). Panel **b** shows the dependence on ρ of the *ab initio* calculated transition dipole moments μ_a and μ_b.

large-amplitude bending vibration wave function is affected by monodromy. To investigate this we show in Fig. 17 the expectation values of the simple non-constant functions ρ and ρ^2, in the large-amplitude basis functions of eqn (27),

$$\langle \Psi_{k\equiv K_a, v_b}(\rho) | \rho | \Psi_{k\equiv K_a, v_b}(\rho) \rangle \qquad (48)$$

and

$$\langle \Psi_{k\equiv K_a, v_b}(\rho) | \rho^2 | \Psi_{k\equiv K_a, v_b}(\rho) \rangle. \qquad (49)$$

In these figures the same monodromy-induced dependence on K_a and v_b is clearly visible, showing that the effects of mono-dromy are directly mapped into the wave-function. This means that any quantity that has a dependence on the large amplitude bending angle will take a form close to the patterns seen in Fig. 17. We note that the monodromy map of $B_{\text{eff}} \approx \langle \mu_b \rangle \approx \langle \rho^2 \rangle$, and $\langle \mu_a \rangle \approx \langle \rho \rangle$, It was actually predictable that

monodromy is not only mapped into the lattice of the energy levels plotted *versus* K_a, but also into the corresponding large-amplitude bending wave-functions, and all quantities depending on them.

5.5 The quasi-linear parameter as a representation of a unit cell in quantum monodromy energy-momentum maps

The quasi-linearity parameter defined by Yamada and Winnewisser[2,60] in 1976 considered the ratio of the energy interval between the ground state and the first $K_a = 1$ level, and the interval between the ro-vibrational ground state and the first vibrationally excited $K_a = 0$ level. This was suggested as the basis of a scalar single parameter characterizing the combined effects of both the effective potential function and the mass dependence of the energy eigenvalues given small-amplitude vibrational state. But this ratio, and the scale chosen to display it, give exaggerated prominence to molecules close to the linear limit, and bunches up the "more bent" species, including NCNCS, close together near the bent limit. It is now clear that there are many molecules, previously classified as bent, which have a monodromy point in the energy range experimentally or astronomically accessible, as in the case of water.

It would be convenient to be able to classify all of these molecules more usefully. We can do this simply by generalizing the original definition of the quasi-linearity parameter to a characteristic *function* depending on the large amplitude vibrational level,

$$\gamma_0(v_b) = 1 - 4\left[\frac{E(v_b, K_a = 1) - E(v_b, K_a = 0)}{E(v_b + 1, K_a = 0) - E(v_b, K_a = 0)}\right]. \quad (50)$$

The pair of energy intervals (here term values with $J = K_a$) defining the original quasi-linearity parameter is now the first member of a set, each pair defining a unit cell in the quantum lattice energy-momentum map, or monodromy plot, of $E(K_a, v_b)$ *vs.* K_a. Such unit cells, spanned by the two vectors $(\Delta K_a, \Delta v_b) = (0,1)$ and $(\Delta K_a, \Delta v_b) = (1,0)$ are shown in Fig. 9 and discussed in ref. 2 and in more detail in ref. 14. If we move this unit cell from the origin at $K_a = v_b = 0$ to successively higher values of v_b with $K_a = 0$, and take the ratios of the two intervals indicated by the two vectors, we obtain a succession of ratios that can be scaled as in eqn (50) (*i.e.* in the same way as the original γ_0[60]), and plotted against the origin, E_{origin}, of the two vectors for a given v_b. (It can also be plotted just using v_b as the ordinate.) In this way we obtain a curve such as that in Fig. 18 for NCNCS. In a classical picture we could say that the molecule traverses from a bent molecular geometry to a linear molecular model upon excitation. The excitation term values are taken from Tables 8–11. Four sample pairs of intervals are indicated by their unit cells in Fig. 9b. The curve in Fig. 18 crosses the diagram rapidly at the monodromy point. A truly bent molecule, in contrast, will have a γ_0 value close to $+1.0$ for bending energies as high as we can measure or calculate.

The recently assigned spectroscopic data for highly excited bending states of the water molecule are given in ref. 18. The values of $\gamma_0(v_b)$ for the various bending states of water calculated from the predictions of the BT2 line list, published

8186 | *Phys. Chem. Chem. Phys.*, 2010, **12**, 8158–8189

This journal is © the Owner Societies 2010
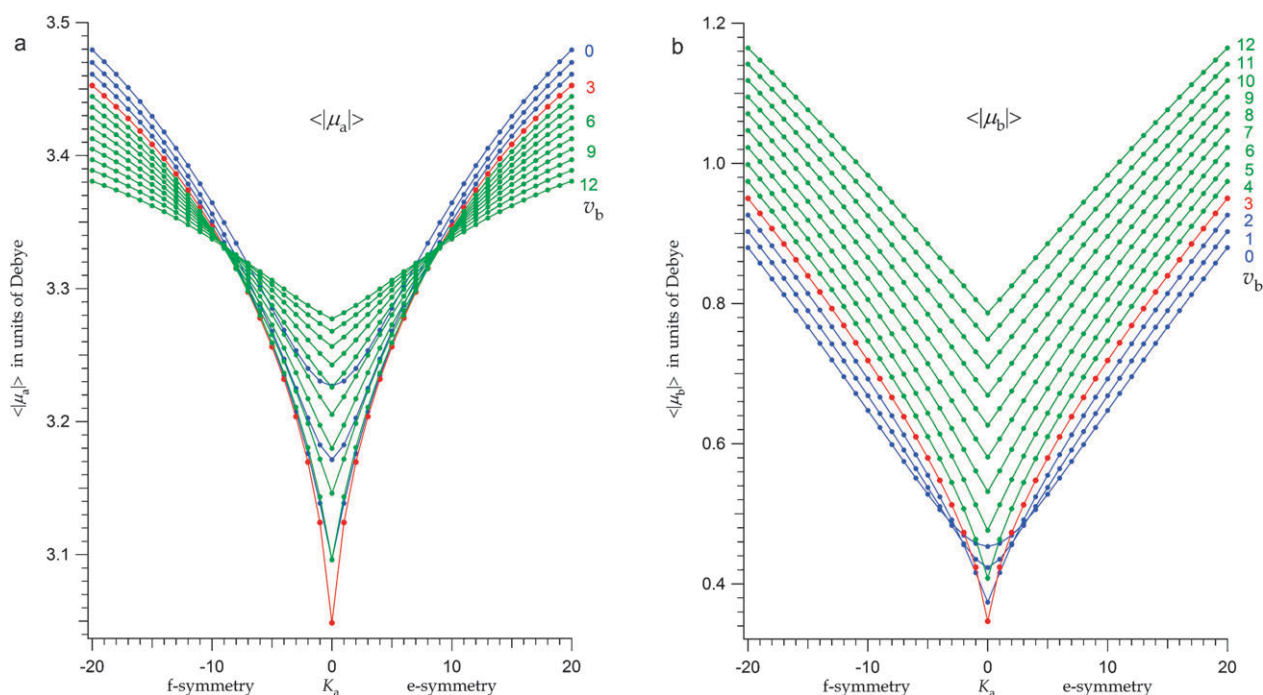
Fig. 16 Expectation values of the permanent electric dipole moment component μ_a (Panel **a**) and μ_b (Panel **b**) for NCNCS as a function of K_a and arranged as quantum monodromy plots. Both sets of values were calculated from an *ab initio* potential function for the large amplitude bending motion with a SRB Hamiltonian. Values for e-symmetry levels are plotted at $K_a \geq 0$, while those for f-symmetry are plotted at $K_a < 0$. The asymmetry splitting for low K_a values was averaged.
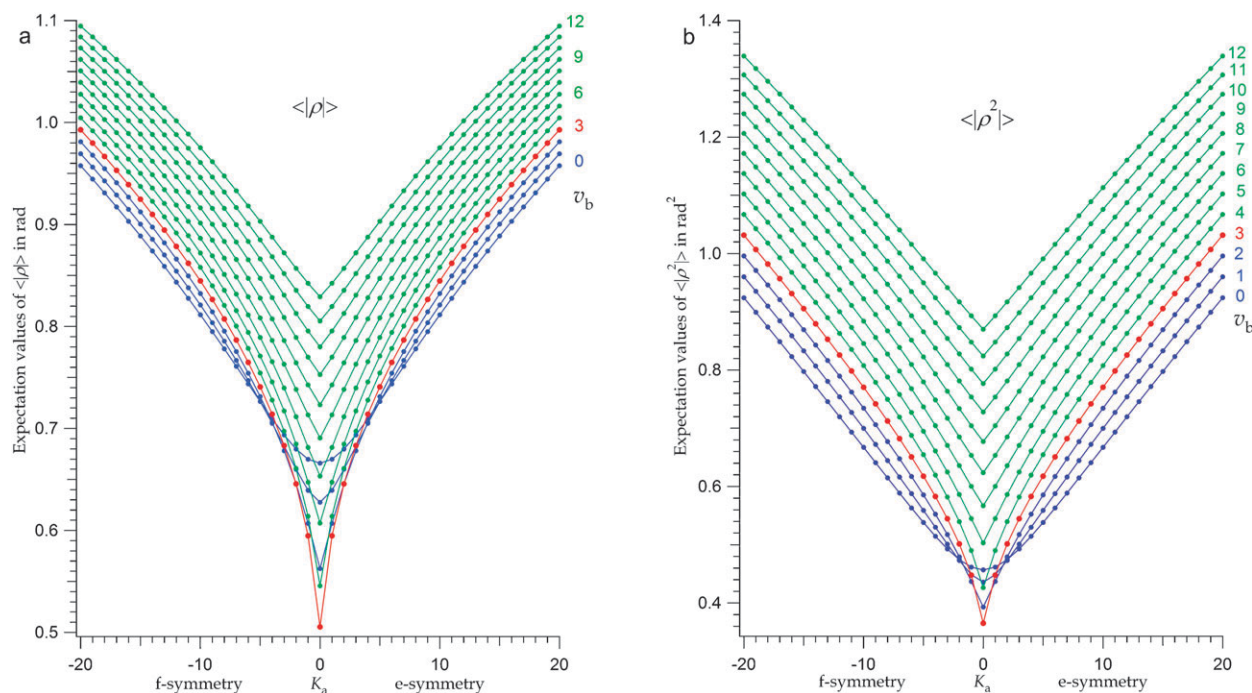
Fig. 17 Panel **a**: Expectation values of the quasi-linear bending coordinate ρ for NCNCS as a function of K_a and v_b and Panel **b**: analogously for ρ^2, arranged as a quantum monodromy plot. Both sets of values were calculated with the GSRB Hamiltonian. Values for e-symmetry levels are plotted at $K_a \geq 0$, while those for f-symmetry are plotted at $K_a < 0$. The asymmetry splitting for low K_a values was averaged.

with ref. 61, are plotted up to $v_2 = v_b = 13$ in Fig. 19. These calculated energies differ from the highest of the experimental values, those for $v_2 = v_b = 9$, by ~ 1.0 cm^{-1}, which is within the pen-width of the plot. The transition from bent to linear for NCNCS is imitated closely by the water molecule, showing the generality of the effect of quantum monodromy. Molecules like OCCCO and HCNO will have curves that look like excerpts of the upper half of Fig. 18.

This journal is © the Owner Societies 2010

Phys. Chem. Chem. Phys., 2010, **12**, 8158–8189 | 8187
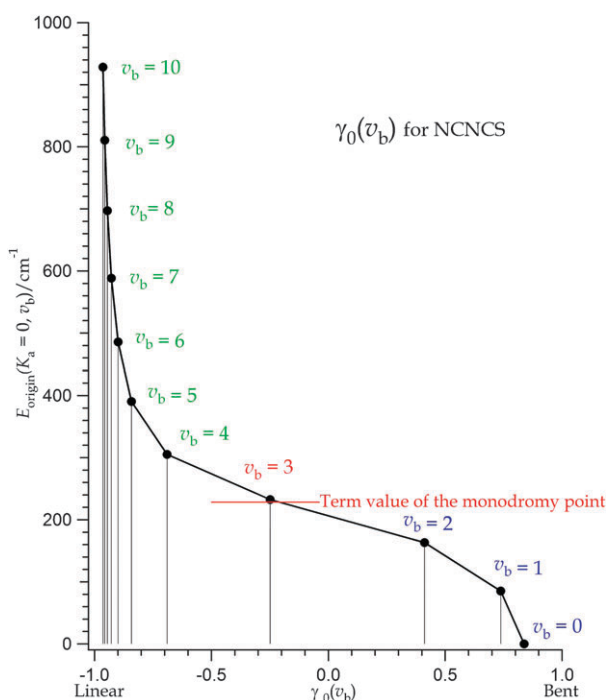
Fig. 18 The quasi-linear characteristic $\gamma_0(v_b)$ values plotted as a function of the bending-rotation term values of the manifold of the quasi-linear bending mode of NCNCS. The data are given in Tables 8 through Table 11.
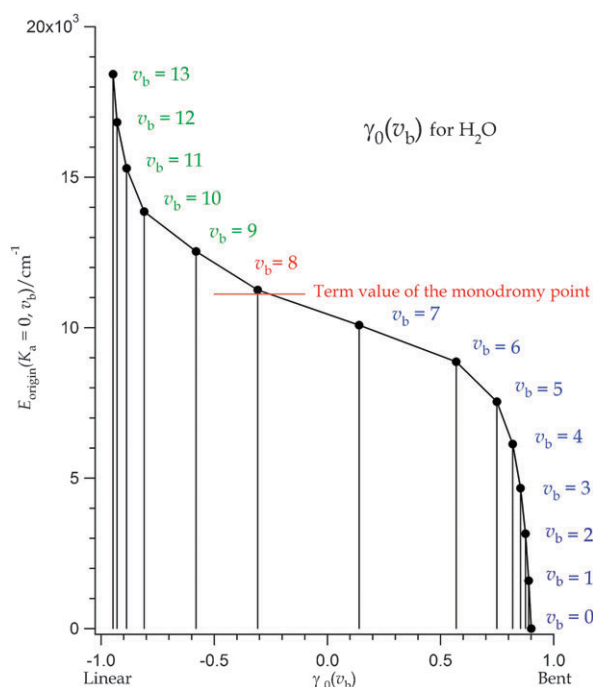
Fig. 19 The quasi-linear characteristic $\gamma_0(v_b)$ values for water have been calculated from the term values available in ref. 18 and 61 and their respective supplementary materials. The bending mode ν_2 for water is replaced by ν_b in our present discussion.

6. Conclusions

As can be seen in Table 3 the current GSRB fitting produces constants very much in agreement with the previously reported

results.[8] This is true even though the fitted value for the CS internuclear distance is 0.03 Å longer in the current work; this simply offsets the 0.03 Å shorter CN and NC internuclear distances used here. In the earlier work no *ab initio* values were available and the fixed internuclear distances, including r_{CN}, were simply estimates. The potential energy functions are also quite similar in the two fittings. We can now reasonably extend the calculations to much higher J than the limit of $J = 9$ in the earlier work. In the light of the above dipole moment discussion a re-scaling of the experimentally observed rotational line intensities becomes feasible and necessary for the line search for the naturally occurring isotopologues.

An aspect of the current analysis that has not been explicitly reported before is the fact that the D_{eff} and H_{eff} values also contain information, which can be used, about the large-amplitude bending motion and the monodromy point of the potential function. The distinctive patterns due to large-amplitude motion are visible at low K_a in Fig. 10 and 11. The good agreement between experimental and GSRB+CD values seen here speaks for the physicality of the GSRB+CD model and how well monodromy is incorporated within it.

We have presented the NCNCS spectral patterns at great length. This is not because we expect this molecule and its dynamics to make an impact in important gas phase applications. Instead, we have done this because these patterns underlie the energy level manifolds of all chain-form molecules, including water. This will be particularly important in those situations where the temperature is sufficient to excite a significant population to levels at or above the monodromy point. Although these patterns may not always be as obvious as they are for NCNCS, where the lowest bending mode is strongly decoupled from the other vibrational modes, they should still help in conceptualizing these previously unsuspected aspects of the structure and properties of the energy level manifolds of these molecules.

Furthermore we have shown that almost every property of the molecular energy levels is affected by quantum monodromy. This includes the effective rotational spectroscopic constants, B_{eff}, D_{eff}, and H_{eff} (the monodromy effects on the latter two examined for the first time) and the dipole transition moments. In section 5.3 we showed that essentially any molecular property that changes due to the large-amplitude vibrational motion will exhibit such behaviour. That is, the effects of monodromy are mapped into the wave function and thus become ubiquitous.

6.1 Supplementary material

Tables submitted as electronic supplementary material† with this paper include:

Table 1. List of all 9204 assigned rotational transitions, including assignment, position, intensity, estimated experimental error (set large for observed perturbations), and deviation from polynomial fit calculations made for each series using the constants in Tables 5–7 of this paper.

Table 2. Predictions of series origins $E_{origin} = E(K_a, v_b, J = K_a, e/f)$, B_{eff}, D_{eff}, and H_{eff} based on GSRB calculations up to $J = 20$ and $v_b = 12$, used for Fig. 9 thus extending beyond the range included in Tables 8–11 of this paper.

Table 3. Bending-rotation term values calculated for $J \leq 20$ and $v_b \leq 12$ using the GSRB constants given in Table 3. Some minor trends indicate lack of convergence for $v_b = 10$ to 12, but these values are included for completeness.

Acknowledgements

References

1 B. P. Winnewisser, M. Winnewisser, I. R. Medvedev, M. Behnke, F. C. De Lucia, S. C. Ross and J. Koput, *Phys. Rev. Lett.*, 2005, **95**, 243002.
2 M. Winnewisser, B. P. Winnewisser, I. R. Medvedev, F. C. De Lucia, S. C. Ross and L. M. Bates, *J. Mol. Struct.*, 2006, **798**, 1.
3 H. M. Pickett, *J. Mol. Spectrosc.*, 1991, **148**, 371.
4 I. R. Medvedev, M. Winnewisser, B. P. Winnewisser, F. C. De Lucia and E. Herbst, *J. Mol. Struct.*, 2005, **742**, 229.
5 M. A. King and H. W. Kroto, *J. Chem. Soc., Chem. Commun.*, 1980, 606.
6 H. W. Kroto, *Molecular rotation spectra*, Dover Publications, Inc., 1992.
7 M. A. King, H. W. Kroto and B. M. Landsberg, *J. Mol. Spectrosc.*, 1985, **113**, 1.
8 S. C. Ross, *J. Mol. Spectrosc.*, 1988, **132**, 48.
9 L. M. Bates, *Z. Angew. Math. Phys.*, 1991, **42**, 837.
10 R. Cushman and J. J. Duistermaat, *Bull. Am. Math. Soc.*, 1988, **19**, 475.
11 M. S. Child, T. Weston and J. Tennyson, *Mol. Phys.*, 1999, **96**, 371.
12 M. S. Child, *J. Phys. A: Math. Gen.*, 1998, **31**, 657.
13 M. S. Child, *J. Mol. Spectrosc.*, 2001, **210**, 157.
14 M. Child, *Adv. Chem. Phys.*, 2007, **136**, 39.
15 B. P. Winnewisser, *Molecular Spectroscopy: Modern Research*, 1985, vol. 3, ch. 6, p. 321.
16 W. Quapp and B. P. Winnewisser, *J. Math. Chem.*, 1993, **14**, 259.
17 R. Cushman and L. Bates, *Global Aspects of Classical Integrable Systems*, Birkhäuser, 1997.
18 N. F. Zobov, S. V. Shirin, O. L. Polyansky, J. Tennyson, P. F. Coheur, P. F. Bernath, M. Carleer and R. Colin, *Chem. Phys. Lett.*, 2005, **414**, 193.
19 J. Koput, *J. Mol. Spectrosc.*, 1986, **118**, 448.
20 J. Koput, *J. Mol. Spectrosc.*, 1986, **118**, 189.
21 D. Sadovskii and B. Zhilinskii, *Mol. Phys.*, 2006, **104**, 2595.
22 H. Żołądek, *The Monodromy Group*, Birkhäuser Verlag, Basel, Boston, Berlin, 2006.
23 D. Hilbert, *Göttinger Nachr.*, 1900, 253–297.
24 *Mathematical Developments arising from Hilbert Problems*, ed. F. E. Browder, Proceedings of Symposia in Pure Mathematics, American Mathematical Society, Providence Rhode Island, 1976.
25 J. Čiek, *J. Chem. Phys.*, 1966, **45**, 4256.
26 G. E. Scuseria and T. J. Lee, *J. Chem. Phys.*, 1990, **93**, 5851.
27 T. H. Dunning, Jr., *J. Chem. Phys.*, 1989, **90**, 1007.
28 T. H. Dunning, Jr., K. A. Peterson and A. K. Wilson, *J. Chem. Phys.*, 2001, **114**, 9244.
29 D. E. Woon and T. H. Dunning, Jr., *J. Chem. Phys.*, 1995, **103**, 4572.
30 H.-J. Werner, P. J. Knowles, R. Lindh, F. R. Manby, M. Schütz, P. Celani, T. Korona, G. Rauhut, R. D. Amos, *et al.*, *MOLPRO, a package of* ab initio *programs designed by H.-J. Werner and P. J. Knowles, Version 2006.1*, 2006.
31 J. T. Hougen, P. R. Bunker and J. W. C. Johns, *J. Mol. Spectrosc.*, 1970, **34**, 136.
32 P. R. Bunker and B. M. Landsberg, *J. Mol. Spectrosc.*, 1977, **67**, 374.
33 P. R. Bunker and J. M. R. Stone, *J. Mol. Spectrosc.*, 1972, **41**, 310.
34 A. R. Hoy and P. R. Bunker, *J. Mol. Spectrosc.*, 1974, **52**, 439.
35 P. Jensen, *Comput. Phys. Rep.*, 1983, **1**, 1.
36 S. C. Ross, T. J. Butenhoff, E. A. Rohlfing and C. M. Rohlfing, *J. Chem. Phys.*, 1994, **100**, 4110.
37 P. R. Bunker and P. Jensen, *Molecular Symmetry and Spectroscopy*, NRC Research Press, Ottawa, Ontario, Canada, second edn, 1998.
38 E. B. Wilson, J. C. Decius and P. C. Cross, *Molecular Vibrations: The Theory of Infrared and Raman Vibrational Spectra*, Dover Publications Inc., New York, 1980.
39 B. Podolsky, *Phys. Rev.*, 1928, **32**, 812.
40 H. Meyer, *Annu. Rev. Phys. Chem.*, 2002, **53**, 141.
41 J. W. Cooley, *Math. Comp. Annu.*, 1961, **15**, 363.
42 B. R. Johnson, *J. Chem. Phys.*, 1977, **67**, 4086.
43 J. M. Blatt, *J. Comput. Phys.*, 1967, **1**, 382.
44 J. M. Brown, J. T. Hougen, K.-P. Huber, J. W. C. Johns, I. Kopp, H. Leffebvre-Brion, A. J. Merer, D. A. Ramsay, J. Rostas and R. N. Zare, *J. Mol. Spectrosc.*, 1975, **55**, 500.
45 T. Barrow, R. N. Dixon and G. Duxbury, *Mol. Phys.*, 1974, **27**, 1217.
46 Z. Kisiel, O. Dorosh, M. Winnewisser, M. Behnke, I. R. Medvedev and Frank C. De Lucia, *J. Mol. Spectrosc.*, 2007, **246**, 39.
47 P. A. Helminger and F. C. De Lucia, *J. Mol. Spectrosc.*, 1985, **111**, 66.
48 F. J. Lovas, *J. Phys. Chem. Ref. Data*, 1985, **14**, 395.
49 E. A. Alekseev, S. F. Dyubko, V. V. Ilyushin and S. V. Podnos, *J. Mol. Spectrosc.*, 1996, **176**, 316.
50 D. Patel, D. Margolese and T. R. Dyke, *J. Chem. Phys.*, 1979, **70**, 2740.
51 D. A. Long and D. Steele, *Spectrochim. Acta*, 1963, **19**, 1731.
52 T. T. Tidwell, *Angew. Chem., Int. Ed.*, 2001, **40**, 331.
53 F. W. Loomis and R. W. Wood, *Phys. Rev.*, 1928, **32**, 223.
54 B. P. Winnewisser, J. Reinstädtler, K. M. T. Yamada and J. Behrend, *J. Mol. Spectrosc.*, 1989, **136**, 12.
55 D. T. Petkie, T. M. Goyette, R. P. A. Bettens, S. P. Belov, S. Albert, P. Helminger and F. C. De Lucia, *Rev. Sci. Instrum.*, 1997, **68**, 1675.
56 I. Medvedev, M. Winnewisser, F. C. De Lucia, E. Herbst, E. Białkowska-Jaworska, L. Pszczółkowski and Z. Kisiel, *J. Mol. Spectrosc.*, 2004, **228**, 314.
57 P. Groner, M. Winnewisser, I. R. Medvedev, F. C. De Lucia, E. Herbst and K. V. L. N. Sastry, *Astrophys. J. Suppl. Ser.*, 2007, **169**, 28.
58 Z. Kisiel, L. Pszczółkowski, I. R. Medvedev, M. Winnewisser, F. C. De Lucia and E. Herbst, *J. Mol. Spectrosc.*, 2005, **233**, 231.
59 P. R. Bunker, B. M. Landsberg and B. P. Winnewisser, *J. Mol. Spectrosc.*, 1979, **74**, 9.
60 K. Yamada and M. Winnewisser, *Z. Naturforsch., A*, 1976, **31**, 139.
61 R. J. Barber, J. Tennyson, G. J. Harris and R. N. Tolchenov, *Mon. Not. R. Astron. Soc.*, 2006, **368**, 1087, (http://www.tampa.phys.ucl.ac.uk/ftp/astrodata/water /BT2/).